공학박사 학위논문

Microfluidic Device Using Viscoelastic Flow

점탄성 유동을 이용한 미세유체장치

2018년 8월

서울대학교 대학원

재료공학부

양 세 현

Microfluidic Device Using Viscoelastic Flow

점탄성 유동을 이용한 미세유체장치

지도 교수 윤 재 륜

이 논문을 공학박사 학위논문으로 제출함
2018 년 6 월

서울대학교 대학원
재료공학부
양 세 현

양세현의 박사 학위논문을 인준함
2018 년 6 월

위 원 장 서 용 석 (인)
부위원장 윤 재 륜 (인)
위 원 김 장 주 (인)
위 원 안 철 희 (인)
위 원 송 영 석 (인)

Doctoral Dissertation in Engineering

Microfluidic Device Using Viscoelastic Flow

by

Sei Hyun Yang

Advisor: Prof. Jae Ryoun Youn

August 2018

Department of Materials Science and Engineering

Graduate School

Seoul National University

Abstract

Multiple-line particle focusing has been identified in a straight channel, while single-line particle focusing has been only reported in previous works. By controlling the force balance between elastic force and inertial force induced by geometric features of a channel, a new focusing mechanism has been suggested. Also, another hypothesis has been emerged that each normal stress component is acting on a particle traveling on the viscoelastic flow. Applications of the multiple-line particle focusing have been focused on microfluidic logic operations by developing a microfluidic logic device and a particle valve system.

In Chapter II, we observed the transition between single-line and multiple-line particle focusing in a microfluidic device. The elastic and inertial forces acting on suspended particles were manipulated by tuning the concentration of dilute polymer solution and the flow rate of a fluid. The finding showed that the confinement effects determined by the channel aspect ratio and the inlet geometry lead to the multiple-line focusing of particles in the microfluidic channel due to the fluid elasticity and hydrodynamic behavior of the fluid. A microfluidic channel with high channel aspect ratio possesses broad minimal region of the elastic force across the channel, which generates a wide particle focusing band rather than a single particle focusing at the center. The multiple-line particle focusing occurs as the inertial force outweighs the elastic force, resulting in the particle migration towards the channel sidewalls.

In Chapter III, we investigated a microfluidic logic device that is built based on the particle dynamics in viscoelastic fluid. A logic gate system employing a Boolean function was implemented by utilizing multiple line particle focusing behavior in the microfluidic channel. The device was designed and fabricated to hydrodynamically control the logic operations of XOR, OR, AND, Buffer, and NOT under the fixed flow condition (*e.g.*, flow rate, particle size, and fluid elasticity~1.483). In addition, numerical simulation was carried out to understand the fundamental physics of the particle and fluid behavior in viscoelastic flow. Clear multiple particle focusing lines with high separation resolution (R_{ij}~6.19) were observed and the particle extraction at the outlets were analyzed by image-processing.

In Chapter IV, we proposed an unique valve system for smart particle control by employing a transparent shape memory polymer (SMP) as a constituent material of the microchannel. The core of this strategy was to use SMP instead of poly(dimethylsiloxane)

(PDMS) to give the channel shape-programmable function. The magnitude of the hydraulic resistance formed in the SMP microchannel could be selectively controlled according to the deformation and recovery of the channel. Due to the pressure difference between the two outlets, the path of the focused particles was determined depending on the channel-shape. The pressure distribution and shape memory-recovery behavior of the SMP microchannel were theoretically investigated by the numerical calculations. The operation as a particle valve and its repeatability were confirmed by experimental observation.

In Chapter V, the lateral particle migration was investigated in a hydroxypropyl cellulose (HPC) viscoelastic fluid with a negative first normal-stress difference. Unlike common viscoelastic fluids with positive normal stress differences, double-line particle focusing was identified in a microfluidic channel, which was caused by the negative first normal stress difference. More importantly, unique particle migration with different sized particles in a microchannel was observed in which bigger particles were double-line focused along the channel walls while smaller particles were single-line focused at the center. A new dimensionless parameter, the ratio of the normal force to the viscous drag force, was defined to demonstrate this unique double line focusing behavior of particles in the viscoelastic fluids.

Keywords: Multiple-line particle focusing, microfluidic particle logic device, viscoelastic flow, shape memory polymer, first normal stress difference (N_1), normal stress component, particle separation, flow analysis, structural analysis, heat transfer

Student Number: 2013-23041

Contents

List of Figures

particle focusing phenomenon is observed. At the relatively low polymer concentration, all the particles are double-line focused close to the channel walls. However, as the polymer concentration is increased, the large particles are double-line focused, but the small particles are focused at the center. Hundreds of images are superimposed for an enhanced observation of the particle migration.

Figure 5.10. Particle focusing behavior in HPC solutions. (a) Particle focusing location according to the polymer concentration and the particle size and (b) Particle-separation resolutions (R_{ij}) with respect to various polymer concentrations. $R_{ij} = \Delta x_{ij}/(s_i + s_j)$, where Δx_{ij} is the distance between the *i*-th and *j*-th particles, and s_i is the standard deviation of the *i*-th particle's location.

Figure 5.11. Typical particle focusing behavior in the PEO solution. All of the particles with 5, 10, and 15 μm diameters are focused at the center.

Figure 5.12. Schematic illustration of focusing mechanism of a particle in viscoelastic fluids. (a) Particle behavior in the positive N_1 flow. The particle is focused at the center when the τ_{yy} is negligible. (b) Particle behavior in the negative N_1 flow. The particle is double-line focused close to the wall when the $F_{E,\tau_{yy}}$ outweighs the $F_{\tau_{xy}}+F_{E,\tau_{xx}}$. Here, $F_{E,\tau_{xx}}$ and $F_{E,\tau_{yy}}$ are the elastic forces from τ_{xx} and τ_{yy}, respectively, and F_v is viscous force from τ_{xy}.

Figure 5.13. Focusing mechanism of particles induced by τ_{yy}. (a) Dimensionless number, $\rho a^2 \tau_{yy}/\mu^2$ as a function of the concentration and the particle size. The dimensionless number is defined to figure out the effect of the ratio of the viscous drag force to the normal force τ_{yy} on the particle migration. (b) Focusing location ratio as a function of the number.

Figure 5.14. Single-line and double-line particle-focusing regimes classified according to the $\tau_{yy}/\mu\dot{\gamma}$.

List of Tables

Chapter I.

Introduction

1.1. Particle dynamics in a microsystem

Microfluidics has many advantages including reduced sample consumption, low cost, precise and fast analysis, high throughput and accuracy.[1,2] It is also called as lab-on-a-chip (LOC) since complete laboratory protocols can be achieved on a single chip of few square centimeters. Especially, particle manipulation in flowing liquids has been widely used in biological, pharmaceutical, medical, chemical and industrial fields. The particles suspended in a liquid flow are manipulated with several technologies such as focusing, sorting and trapping, which is essential abilities in a microfluidic system.[1,3] The manipulation method of the particles can be categorized into two approaches as active and passive. For the active approach, the particles are pushed by applied external forces such as optical, magnetic, acoustic and electric forces.[4–7] In the passive way, the particles are manipulated due to only hydrodynamic forces triggered by the flow and intrinsic properties of fluids.[8–12]

Hydrodynamic forces are defined as inertial forces including shear-gradient lift force and wall-repulsion lift force, drag force and elastic force dependent on the fluid properties. Many fundamental studies of particle migration mechanism based on the hydrodynamic forces have been carried out for both Newtonian and non-Newtonian fluids.[3,13] Unlike the Newtonian fluids, non-Newtonian fluids exhibit no linear behavior of viscosity with increasing shear rate. Viscoelasticity, one of the attractive properties of the non-Newtonian complex fluid flow, affects to the particle manipulation by causing the imbalance of the first normal stress difference ($N_1 = \tau_{xx} - \tau_{yy}$), where τ_{xx} is the normal stress toward the flow direction and τ_{yy} is the normal stress toward the perpendicular direction of the flow.[2,12] In general, non-Newtonian properties such as shear-thinning, storage and loss modulus, first and second first normal stress differences can influence the equilibrium

locations of the flow system. It is worthwhile to investigate particle migration in non-Newtonian fluids for understanding the particle dynamics and guiding the optimum process for applications such as cell counting, separation, and uniform distribution. Complex fluids such as dilute polymer and DNA solutions, animal blood, and biopolymer solution have long chain molecules in a Newtonian base medium. As dilute polymer solutions, PEO (Polyethylene oxide), PVP (Polyvinyl pyrrolidone), HPC (Hydroxypropyl cellulose), DNA (DeoxyriboNucleic acid) and HA (Hyaluronic acid) have been commonly used for microfluidic analysis. A microfluidic system was fabricated by using soft-lithography (*i.e.*, PDMS (Polymethylsiloxane) molding methods). Soft-lithographic techniques have several advantages such as low cost, simple process and outstanding accessibility and repeatability.[14] To generate micropatterns and microstructures with high replication rate, pre-polymer of PDMS, which is a transparent elastomeric polymer, was poured over a master. After degassing, the polymer was cured at high temperature near 70℃, then, peeled off. The detail soft-lithography process is schematically illustrated in **Figure 1.1**.

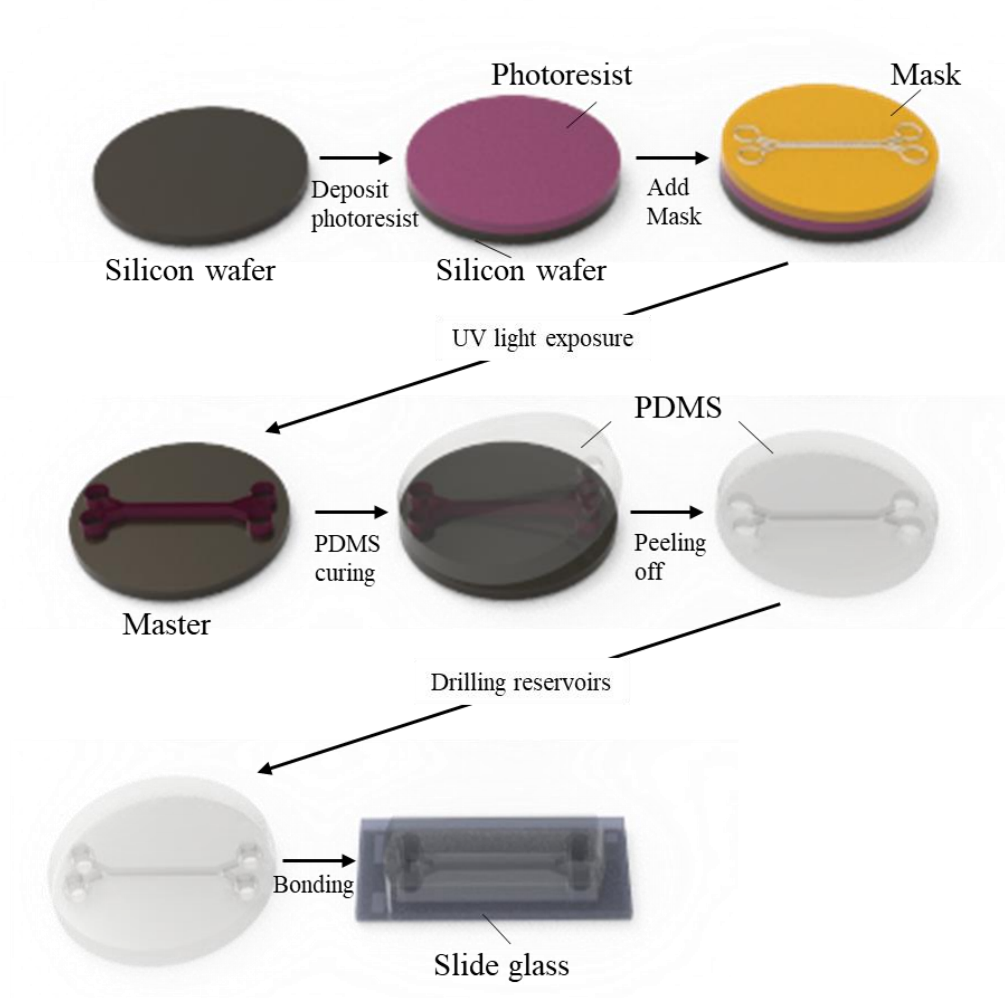

Figure 1.1. Microchannel fabrication by using Soft lithography.

1.1.1. Hydrodynamic forces induce by viscoelastic flow

Particles suspended in viscoelastic fluids experience three hydrodynamic forces (*i.e.*, inertial force (F_L), elastic force (F_E) and drag force (F_D)) when they flow through a confinement. The forces acting on the particle compete until the particle is located at the equilibrium position in the flow. The particle focusing locations are mainly tuned by the force competition between the inertial force and the elastic force under viscoelastic flow. The direction of each force acting on a particle is schematically described in **Figure 1.2**.

By velocity gradient between the fluid and particles, the viscous drag force is induced and the particle migration can be influenced. The drag force (F_D) allows the particles to be accelerated until the particles flow under steady-state flow condition in the flow direction.[3] When a spherical particle is in a uniform Stokes flow, the Stokes drag is defined as

$$F_D = 3\pi\eta a(U - U_p) \tag{1-1}$$

, where η is the fluid viscosity, a is the particle diameter, and U and U_p is the velocities of fluid and particle.

Two kinds of inertial force are acting on the particles suspended in a fluid. The inertial force (F_L) is comprised of the shear gradient lift force ($F_{L.S}$) and the wall repulsion lift force ($F_{L.W}$). The shear gradient lift force pushes the particle toward the channel sidewalls, acting down the gradient in shear rate of the flow.[1,3] The shear gradient lift force can be scaled as

$$F_{L.S} = f_L \rho U^2 a^3 / W \tag{1-2}$$

, where ρ is the fluid density, W is the channel width, and f_L is the lift coefficient. For most microfluidic applications, the lift coefficient remains to be constant. The f_L is approximated as 0.5 at Re $(= \rho U D_h/\eta) < 100$, where D_h $(= 2WH/(W + H))$ is the hydraulic diameter and H is the channel height. The wall repulsion lift force pushes the opposite direction of the shear gradient lift force which is toward the channel centerline. Near the wall, the repulsion lift force can be scaled as

$$F_{L.W} = f_L \rho U^2 a^6 / W^4. \quad (1\text{-}3)$$

Therefore, the net inertial lift force can be expressed as

$$F_L = f_L \rho U^2 a^4 / D_h^2. \quad (1\text{-}4)$$

The elastic force is induced by the intrinsic properties of a viscoelastic fluid. In a viscoelastic fluid, τ_{xx}, τ_{yy}, and τ_{zz} normal stresses are generated along the flow direction, velocity gradient direction and vorticity direction, respectively. The difference of the normal stresses are defined as the first normal stress difference ($N_1 = \tau_{xx} - \tau_{yy}$) and the second normal stress difference ($N_2 = \tau_{yy} - \tau_{zz}$). The first normal stress difference is much larger than the second normal stress difference. Therefore, the first normal stress difference a major driving force for the particle migration and the elastic force is expressed as below, proportional to the gradient of first normal stress difference (N_1).

$$F_E \approx a^3 \nabla N_1 \quad (1\text{-}5)$$

The first normal stress difference can be numerically calculated to compare the magnitude of the elastic force. By assuming incompressible steady-state viscoelastic flow conditions, the governing equations of fluid dynamics[2] are defined as follows:

Mass balance (continuity): $$\nabla \cdot \boldsymbol{u} = 0 \quad (1\text{-}6)$$

Momentum balance: $$\rho \left(\frac{\partial \boldsymbol{u}}{\partial t} + \boldsymbol{u} \cdot \nabla \boldsymbol{u} \right) = \nabla \cdot \boldsymbol{\sigma} \quad (1\text{-}7)$$

Total stress tensor: $$\boldsymbol{\sigma} = -p\boldsymbol{I} + 2\eta_s \boldsymbol{D} + \boldsymbol{T} \quad (1\text{-}8)$$

Here, $\boldsymbol{u}$ is the velocity vector, p is the dynamic pressure, η_s is the viscosity of Newtonian solvent, $\boldsymbol{I}$ is the unit tensor, $\boldsymbol{D}$ is the rate of deformation tensor, defined as $(\nabla \boldsymbol{u} + (\nabla \boldsymbol{u})^T)/2$. $\boldsymbol{T}$ denotes the extra viscoelastic stress contribution and extra stress tensor is defined by selecting a proper constitutive equation among several equations. In

the researches, we used the upper convective Maxwell model (or Oldroyd-B model) for the viscoelastic stress contribution. The model is defined as

$$\boldsymbol{T} + \lambda\left(\frac{\partial \boldsymbol{T}}{\partial t} + (\boldsymbol{u}\cdot\nabla)\boldsymbol{T} - [(\nabla\boldsymbol{u})\cdot\boldsymbol{T} + \boldsymbol{T}\cdot(\nabla\boldsymbol{u})^T\right) = \eta_p(\nabla\boldsymbol{u} + (\nabla\boldsymbol{u})^T) \qquad (1\text{-}9)$$

, where λ is the characteristic relaxation time and η_p is the viscosity of the polymer. The Oldroyd-B model is one of the simplest viscoelastic models that can be expressed in an analytical way such that $N_1 \approx \tau_{xx}$ and $N_2 \approx 0$ in simple shear flows. The minimal N_1 values are distributed around the flow center (*i.e.*, **Figure 1.2**, blue region), therefore, the region is the most stable location for the suspended particles.

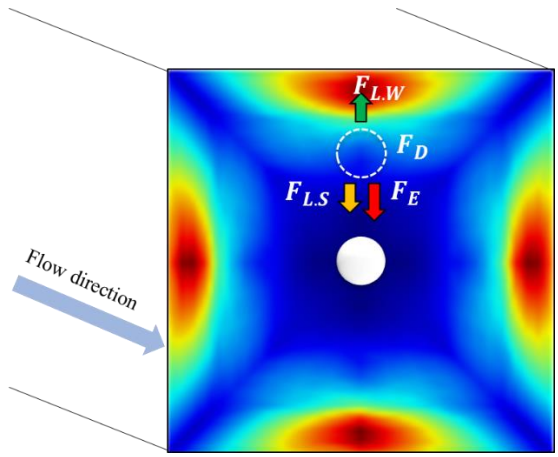

Figure 1.2. A schematic illustration of hydrodynamic forces acting on a particle under the first normal stress difference distribution.

1.1.2. Normal stress measurement

Normal stresses in shear flow are the evidence of elasticity in liquids with storage modulus (G') and loss modulus (G'') since polymeric liquids behave much like rubber at short times and high strain rate due to their entangled coil. And the normal stress measurements can be very useful to speculate micro-structural changes induced by the shear such as large scale disentanglement of chains, phase change or molecular orientation. By using a conventional bulk rheometer, the normal stresses can be measured.[15] Each normal stress cannot be measured without customized pressure sensors embedded in the accessories for the shear flow measurement. Therefore, the difference of the normal stresses are defined with related to the torque and normal forces.

The first normal stress difference (N_1) of a viscoelastic fluid can be measured by using a cone-and-plate geometry with relation of the normal force F_N. The F_N acting on the upper cone surface is measured and the N_1 can be defined as below, where R is the radius of the plate.

$$N_1 = \frac{2F_N}{\pi R^2} \tag{1-10}$$

When the parallel plates is used for the measurement, the difference between the N_1 and N_2 can be obtained with definition as

$$N_1 - N_2 = \frac{2F_N}{\pi R^2}\left[1 + \frac{d\ln F_N}{2d\ln\Omega}\right] \tag{1-11}$$

, where Ω is the angular velocity.

1.1.3. Elasto-inertial particle focusing

For the particle focusing in a viscoelastic fluid, the fluid elasticity is a significant factor leading the focusing behavior. The fluid elasticity (El=Wi/Re) is a dimensionless number, defined as the ratio of Weissenberg number (Wi) to Reynolds number (Re). Wi ($= \lambda\dot{\gamma} = 2\lambda Q/HW^2$) is a dimensionless number representing the elastic effect of flow, where $\dot{\gamma}$ is the shear rate, and Q is the flow rate. And, Re ($= \rho U D_h/\eta$) is a dimensionless number indicating the relative importance of the inertial effect and viscous effect. By comparing these two dimensionless numbers, a major force for the particle focusing phenomena can be speculated. For examples, the single line particle focusing at the channel center in a square microchannel is observed when El is larger than the unity (El>1) as shown in **Figure 1.3(a)**. Since the elastic force is overwhelming compared to the inertial force, the particles migrate toward the channel center, where the first normal stress difference is the minimum. When the inertial force is comparably larger than the elastic force (El<1), the focusing locations can be several (**Figure 1.3(b)**) or unstable focusing behavior can be observed.

In a rectangular channel, the inertial force is meaningful and the particles can be considerably affected by shear-induced migration at even low Re.[13] Also, even a small magnitude of the second normal stress difference (N_2) induces a secondary flow in a simple shear flow in a rectangular channel, while the N_2 is about 10 % of N_1 in general.[1,2,13] The secondary flow effect can be detected by using the particles with low blockage ratio ($\beta = a/H$) about 0.02, where a is the particle diameter and H is the channel height. So far, the elasto-inertial particle focusing in a shear-thinning fluid has been reported based on the N_1 distribution with single line particle focusing.

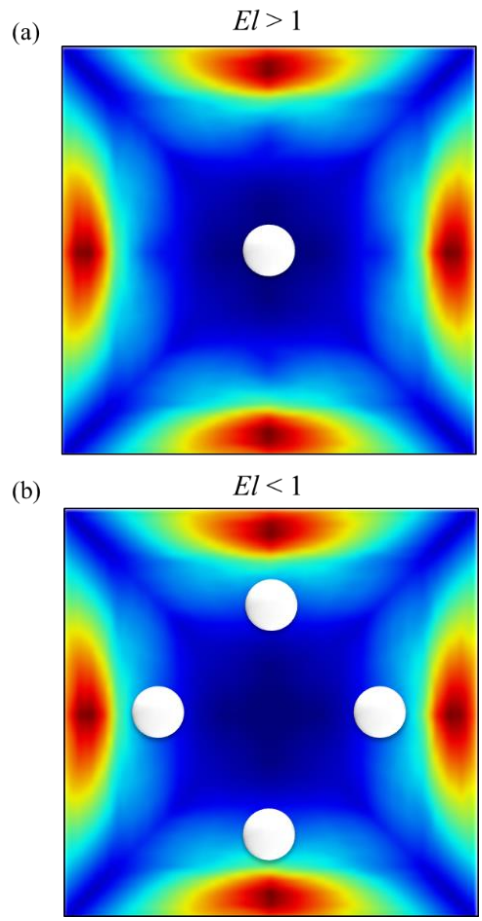

Figure 1.3. Probable focusing locations of particles in flow conditions. (a) When $El > 1$ and (b) When $El < 1$.

1.2. Integration of electronics into microfluidics

The microfluidic devices have developed in the fields of analytical chemistry and biomedical sciences. The miniaturized fluidic technologies with high accuracy are not feasible since the devices are based on the non-linear behaviors, generating high driving pressures. Many attempts have been made to improve the accuracy by integrating various engineering technologies into microfluidic devices.[16–20] As a typical integration, the electronic engineering has been merged with the flow operation. A fluidic circuit has been a popular research topic in 1960s to compete with electronics. The electronic devices were smaller and faster than the fluidic circuit, therefore, the earlier work of fluidic circuit lost the competition. However, the use of fluidic system to perform the logical calculation is still important in micro-, nano-scale platforms. By using the nonlinearity of the fluids, amount of applications have been reported with related to the electronics concepts such as transistor, memory device, logic gate and cascaded systems.[17,20–22]

In order to merge the electronics into the microfluidics, we should understand the logical concept which is the basic operation for all electronic devices. Boolean algebra consists of the truth values, *i.e.*, truth and false, and it is usually denoted 1 and 0, respectively. The Boolean functions are practically implemented by using logic gate. The logic gate is an element for building a digital circuit and most logic gates have two inputs and one output. Since the electronic gates require a power supply, every terminal is in one of the two binary number driven by the voltages and logical values of 0 and 1 represent 0 V and 5 V, respectively. There are three basic logic gates, *i.e.*, AND, OR, NOT, and the false of the AND and OR is NAND and NOR. XOR (exclusive-OR) acts as the logical "either/or," the output is 1 only if the inputs are different. XNOR is the false of the XOR. Each gate can be described as the truth table, symbols and the circuits. The simple logic circuit of each gate is represented in **Figure 1.4**.

(a)

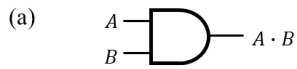

Input(A)	Input(B)	AND
0	0	0
1	0	0
0	1	0
1	1	1

(b)

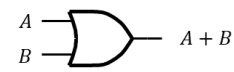

Input(A)	Input(B)	OR
0	0	0
1	0	1
0	1	1
1	1	1

(c)

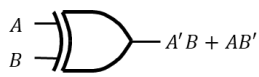

Input(A)	Input(B)	XOR
0	0	0
1	0	1
0	1	1
1	1	0

(d)

Input (A)	NOT
0	1
1	0

(e)

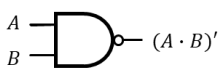

Input(A)	Input(B)	NAND
0	0	1
1	0	1
0	1	1
1	1	0

(f)

Input(A)	Input(B)	NOR
0	0	1
1	0	0
0	1	0
1	1	0

(g)

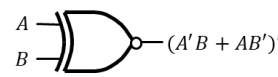

Input(A)	Input(B)	XNOR
0	0	1
1	0	0
0	1	0
1	1	1

Figure 1.4. Truth table and circuit of logic gates. (a) AND, (b) OR, (c) XOR, (d) NOT, (e) NAND, (f) NOR, and (g) XNOR.

1.3. Objectives of present work

Most studies of viscoelastic particle focusing phenomenon has been reported as single-line particle focusing due to the force balance between the elastic force related to the first normal stress difference distribution and inertial force induced by the flow. In the elasticity-dominant flow condition, the particles are aligned as a single line at the center in a radius pipe or a square channel. However, the focusing locations of the particles can be tuned by the additional inertial forces, the hydraulic pressure generation or the rheological properties of the viscoelastic fluids. We manipulated the particles in both passive and active ways based on the modification of viscoelastic particle focusing mechanism. In order to explore and understand the particle dynamics in viscoelastic flow, four major topics are carried out in present study.

To demonstrate the tunable particle focusing locations, we firstly investigated the multiple-line particle focusing in a straight channel based on the viscoelastic particle focusing mechanism. The additional inertial forces were generated by controlling the microchannel geometry such as the number of channel inlets and cross-sectional aspect ratio of the channel. By the numerical simulation, the minimal first normal stress difference region of difference channel aspect ratios (1:1, 2:1, and 4:1) was compared to increase the particle probability. To identify the tunable particle focusing locations, the number of channel inlets were increased from one to three. Consequently, the particles were aligned as double-line and triple-line along the channel width in a high aspect ratio channel. With varying the flow conditions, a *Re*-*Wi* working space for the multiple-line particle focusing was arranged from the experimental results with an illustration of the focusing mechanism.

To overcome issues of low accuracy and lack of analytical applications in a microscale fluidic device, we secondly developed a binary microfluidic device including several logic gates. By integrating of the electronics and microfluidics, the truth (binary number 1) and the false (binary number 0) were assigned according to the existence of the particles in a channel. Based on the multiple-line particle focusing mechanism, the basic logic gates including AND, OR, NOT, Buffer and XOR were realized in one microfluidic device. The particle streamlines and the normal stresses induced the fluid injection were expected by using numerical calculation based on finite element method.

Thirdly, we manipulated the path of multiple focused particles to structure a new microfluidic logic device by substituting PDMS microchannel to an acrylic shape memory polymer (SMP) microchannel. With the local deformation of the SMP microchannel, the difference of the local hydraulic pressure and resistance increases and it induces the change of the particle progress path. The deformed channel cross-section was experimentally observed and the distorted shape was numerically verified by the structural analysis. By the numerical flow analysis, the hydraulic pressure and resistance was calculated and compared to the analytical calculation results. From the results, a microfluidic particle valve was identified and a microfluidic logic circuit was also suggested as an application of the valve system.

Meanwhile, the first normal stress difference (N_1) of a viscoelastic fluid is defined with the positive sign and the negative sign. Typically, most of polymeric fluids show a positive N_1 under the shear flow. Some interesting complex fluids (*e.g.,* liquid crystalline polymer solution) exhibit a negative N_1. To investigate the particle dynamics in the negative N_1 solution, the particle migration was observed and the magnitude of the normal stresses were experimentally estimated by assuming incompressible linear viscoelastic fluid. The multiple-line particle focusing behavior was demonstrated in the negative N_1 solution, while a single-line particle focusing was observed in the positive N_1 solution when the solutions flow through the 2:1 aspect ratio straight channel. The interesting migration behavior was verified with the dimensionless number and the schematic illustration from the experimental evaluations. From these results, we aim to predict the normal stresses acting on the particles in the viscoelastic flow and structure a new fluidic logical operation in a microscale. We anticipate these researches help understanding the particle dynamics under the viscoelastic flow based on the rheological properties and make a guideline for designing a microfluidic platform for customized analysis.

1.4. References

1. Yuan, D. *et al.* Recent progress of particle migration in viscoelastic fluid. *Lab Chip* **18,** 551–567 (2018).
2. D'Avino, G. & Maffettone, P. L. Particle dynamics in viscoelastic liquids. *J. Nonnewton. Fluid Mech.* **215,** 80–104 (2015).
3. Di Carlo, D. Inertial microfluidics. *Lab Chip* **9,** 3038 (2009).
4. Ohta, A. T. *et al.* Optically controlled cell discrimination and trapping using optoelectronic tweezers. *IEEE J. Sel. Top. Quantum Electron.* **13,** 235–242 (2007).
5. Vahey, M. D. & Voldman, J. An equilibrium method for continuous-flow cell sorting using dielectrophoresis. *Anal. Chem.* **80,** 3135–3143 (2008).
6. Chiou, P. Y., Ohta, A. T. & Wu, M. C. Massively parallel manipulation of single cells and microparticles using optical images. *Nature* **436,** 370–372 (2005).
7. Procedures, E. Conformational properties of hydroxypropylcellulose--ii. flow birefringence and optical anisotropy of hydroxypropylcellulose macromolecules. **26,** 787–790 (1990).
8. Villone, M. M., D'Avino, G., Hulsen, M. A., Greco, F. & Maffettone, P. L. Particle motion in square channel flow of a viscoelastic liquid: Migration vs. secondary flows. *J. Nonnewton. Fluid Mech.* **195,** 1–8 (2013).
9. Lee, D. J., Brenner, H., Youn, J. R. & Song, Y. S. Multiplex particle focusing via hydrodynamic force in viscoelastic fluids. *Sci. Rep.* **3,** 3258 (2013).
10. Chung, A. J., Gossett, D. R. & Di Carlo, D. Three dimensional, sheathless, and high-throughput microparticle inertial focusing through geometry-induced secondary flows. *Small* **9,** 685–690 (2013).
11. Bhagat, A. A. S., Kuntaegowdanahalli, S. S. & Papautsky, I. Inertial microfluidics for continuous particle filtration and extraction. *Microfluid. Nanofluidics* **7,** 217–226 (2009).
12. Li, G., McKinley, G. H. & Ardekani, A. M. Dynamics of particle migration in channel flow of viscoelastic fluids. *J. Fluid Mech.* **785,** 486–505 (2015).
13. Yang, S., Kim, J. Y., Lee, S. J., Lee, S. S. & Kim, J. M. Sheathless elasto-inertial particle focusing and continuous separation in a straight rectangular microchannel.

Lab Chip **11,** 266–273 (2011).

14. Qin, D., Xia, Y. & Whitesides, G. M. Soft lithography for micro- and nanoscale patterning. *Nat. Protoc.* **5,** 491–502 (2010).
15. Miller, M. J. & Christiansen, E. B. The stress state of elastic fluids in viscometric flow. *AIChE J.* **18,** 600–608 (1972).
16. Zhao, Y. & Chakrabarty, K. Fault diagnosis in lab-on-chip using digital microfluidic logic gates. *J. Electron. Test. Theory Appl.* **27,** 69–83 (2011).
17. Groisman, A., Enzelberger, M. & Quake, S. R. Microfluidic memory and control devices. *Science* **300,** 955–958 (2003).
18. Ramalingam, N. *et al.* Fluidic Logic Used in a Systems Approach to Enable Integrated Single-Cell Functional Analysis. *Front. Bioeng. Biotechnol.* **4,** (2016).
19. Liu, W., Ren, Y., Tao, Y., Li, Y. & Wu, Q. On traveling-wave field-effect flow control for simultaneous induced-charge electroosmotic pumping and mixing in microfluidics : physical perspectives and theoretical analysis. (2018).
20. Liu, W. *et al.* On utilizing alternating current-flow field effect transistor for flexibly manipulating particles in microfluidics and nanofluidics. *Biomicrofluidics* **10,** (2016).
21. Zhan, W. & Crooks, R. M. Microelectrochemical logic circuits. *J. Am. Chem. Soc.* **125,** 9934–9935 (2003).
22. Prakash, M. & Gershenfeld, N. Microfluidic Bubble Logic. *Science* **274501,** 832–836 (2007).

Chapter II.

Multiple-line particle focusing

2.1. Introduction

Passive manipulation of particles in a microfluidic platform has been widely explored in recent years by using viscoelastic fluids since controlling particles or cells suspended in a fluid becomes important in a wide range of applications such as biology[1], optics[2], and electronics[3]. Viscoelasticity, one of the most intriguing properties of complex fluids such as diluted polymer and DNA solutions, animal blood, and biopolymer solution, represents the combination of elastic and viscous features in various flow conditions.[4,5] The viscoelasticity causes the imbalance of the first normal stresses of fluid ($N_1 = \tau_{xx} - \tau_{yy}$) in a channel, which can allow particles suspended in the viscoelastic medium to migrate towards a position with minimal hydrodynamic energy.[6–19] Here, τ_{xx} and τ_{yy} are the normal stresses developed in the flow direction and the shear-gradient direction.

Since *Segré* and *Silberberg* first reported particle migration in a Newtonian fluid[20] flowing in a circular pipe, many fundamental studies related to the particle migration have been carried out for both the Newtonian and non-Newtonian fluids.[6–19,21–23] This passive particle manipulation technique harnesses mainly three factors such as hydrodynamic forces, intrinsic properties of fluids, and channel confinement. Inertial focusing in the microfluidic channel has been studied extensively for the Newtonian fluid in which particles are driven into a specific position by inertial and viscous drag forces.[22–33] Particles in a pipe flow form an annular ring at the location of around $0.6R$ away from the center (here, R is the radius of tube), which is well-known as the tubular pinch effect.[20] For a square cross-sectional microchannel, suspended particles are focused at four symmetric positions, which are face-centered on each wall due to high shear rate at the corners.[27] Because the non-Newtonian fluid possesses remarkable rheological behaviors such as viscoelastic and shear thinning effects,[6,7,34–38] particles are focused at four corners and at the center of the channel cross-section when the fluid elasticity is larger than the fluid

inertia.[18] The multiple equilibrium focusing positions is reduced to single equilibrium position (*i.e.,* the centerline of channel) when *Re* is high enough meaning that the flow rate of viscoelastic solution is high.

The geometry and structure of a channel play important roles in determining particle migration. A number of studies regarding the particle migration and separation have been investigated by changing the channel geometry, *e.g.*, with the use of expansion contraction array[29,31,32], curved shape[12,19,30,33], and 3D hydrodynamic focusing[39]. This deformed channel geometry creates additional secondary forces that can lead particles towards different equilibrium positions. In addition, the channel aspect ratio, width to height ratio, can affect the equilibrium position of particles. Particles in a Newtonian fluid migrate towards two long-face-centered positions of the high aspect ratio channel due to rotation-induced lift force.[40] However, the particle migration for the non-Newtonian fluid relies on not only the competition between the elastic and the inertial forces but also the channel aspect ratio.[19,41] To our best knowledge, the first study on this subject conducted by Liu *et al*.[42] focused on the application of different sized particle/cell separation in a straight channel with different channel aspect ratios while little attention was paid to the fundamental mechanism of the transition between single-line and double-line particle focusing dynamics over various influencing factors.

In this study, we investigated particle migration under viscoelastic flow in a microfluidic device depending on the inlet geometry and the aspect ratio of the channel. A key finding is that we observed the multiple-line particle focusing induced by the combined effect of the fluid elasticity and hydrodynamic behavior of the fluid by the confinement geometry of the channel. We examined the particle focusing behavior controlling several variables of geometry such as aspect ratio (*e.g.*, 1:1, 2:1 and 4:1) and inlet number (*e.g.*, double inlets and triple inlets). A $Re - Wi$ diagram for the multiple-line particle focusing was introduced to understand the underlying physics behind the phenomenon. Numerical analysis was carried out to model viscoelastic and hydrodynamic forces acting on the particles passing through different channel aspect ratios.

2.2. Experimental

2.2.1. Design and fabrication of a microchannel

Straight microfluidic channels with different aspect ratios and inlet channel geometries are fabricated for the particle focusing and design of the channel was described in **Figure 2.1 (a)**. A channel height is fixed to 25 μm, and channel width is set to be 25, 50, and 100 μm. The corresponding channel aspect ratios (*AR* = *W*/*H*) are 1:1, 2:1, and 4:1 (**Figure 2.1 (b)**). Asymmetrical outlet channels are designed to clarify the multiple-line particle focusing in the device. The microchannel has a length of 40 mm, which is longer than the calculated focusing length to stabilize the position of the particles based on the focusing length calculation. The focusing length of the particle at low *Wi* can be simply calculated by the channel dimension, the blockage ratio (d_p/H), and the Weissenberg number (Wi), which is expressed as $\Theta = Wi(L/H)(d_p/H)^2$,[43,44] where d_p is the particle diameter, *H* is the channel width, and *L* is the focusing length. By substituting *Wi* = 1.67, *H* = 100 μm, d_p= 6.42 μm , and $\Theta = 1$ for the perfect particle focusing, the focusing length of the channel is calculated to be 14.5 mm. A microchannel is fabricated with PDMS (Sylgard 184, Dow Corning) by using a standard soft lithography method. The micropattern of a replica mold is constructed on a silicon wafer with negative photoresist (SU-8, Microchem Corp.). A PDMS solution composed of base and curing agents (10:1) is poured onto the SU-8 master. The mold is degassed in a vacuum chamber for 1 hour and cured in an oven at 65 ℃ for 6 hours. The PDMS channels are peeled off and punched using a puncher with a 1.5 mm diameter (Uni-Core, Harris) for tube connections. The channels are bonded onto a slide glass by using a plasma cleaner and heated at 120 ℃ for 1 hour to enhance the bonding strength.

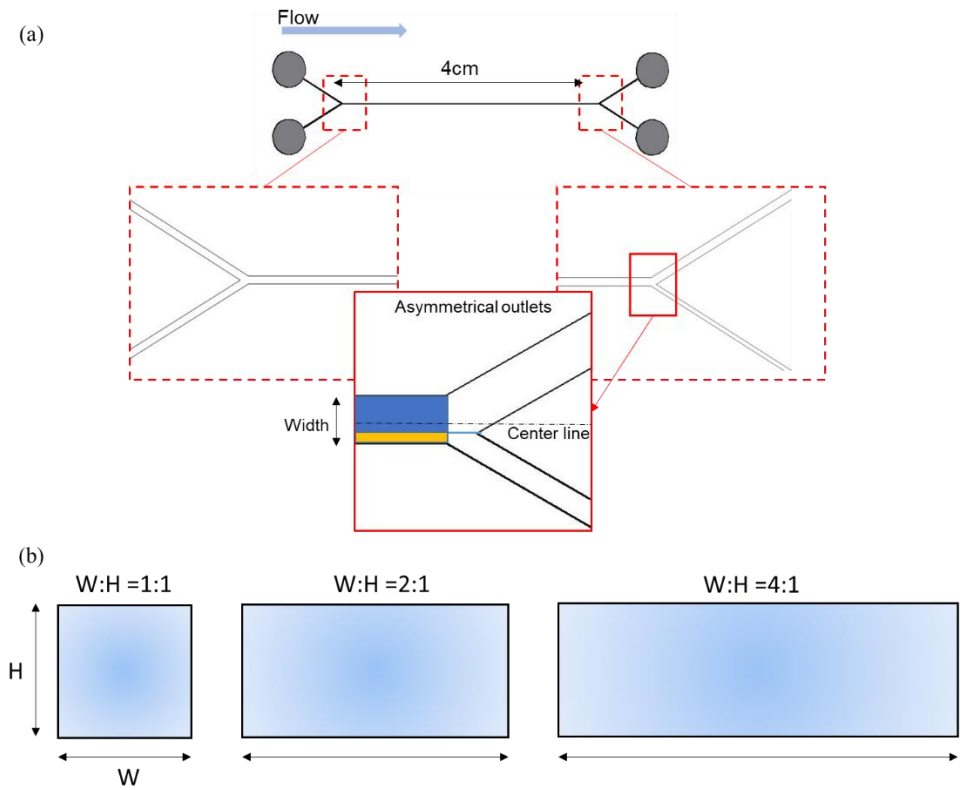

Figure 2.1. Design of a microchannel. (a) A microchannel consists of 2 inlets and 2 outlets with y-shaped geometry and 40 mm of straight part. The outlets is designed to have asymmetrical portion of flow for particle observation. (b) Channel cross-sectional aspect ratio was varied from 1:1 to 4:1.

2.2.2. Sample preparation

Viscoelastic fluids used in our experiments are PEO (polyethylene oxide, M_w=2,000,000, Sigma-Aldrich) solutions with 22 wt% aqueous glycerol. The concentrations of PEO in the solutions vary in the range of 500 to 4000 ppm. Fluorescent polystyrene particles with a diameter of 6.42 μm (Nile red, Spherotech Inc.) and non-fluorescent PS particles of 10 μm (Polysciences, Inc.) and 15 μm (Polysciences, inc.) are suspended in the viscoelastic medium with a small amount of Tween 20 (P1379-25ML, Sigma-Aldrich) to prevent aggregation of the particles shown in **Figure 2.2**. The microchannel is first flushed with a viscoelastic medium for the prevention of particle adhesion onto the channel wall. The solutions are injected into the microchannel using a syringe pump (KDS 200, KD Scientific) with flow rates ranging from 0.05 ml/hr to 0.6 ml/hr. An inverted optical microscope (IX 53, Olympus) and CCD camera (AcquCAM 23G, VISIONHI) are used to analyze the particle migration. The lateral positions of particles are measured by using an ImageJ software.

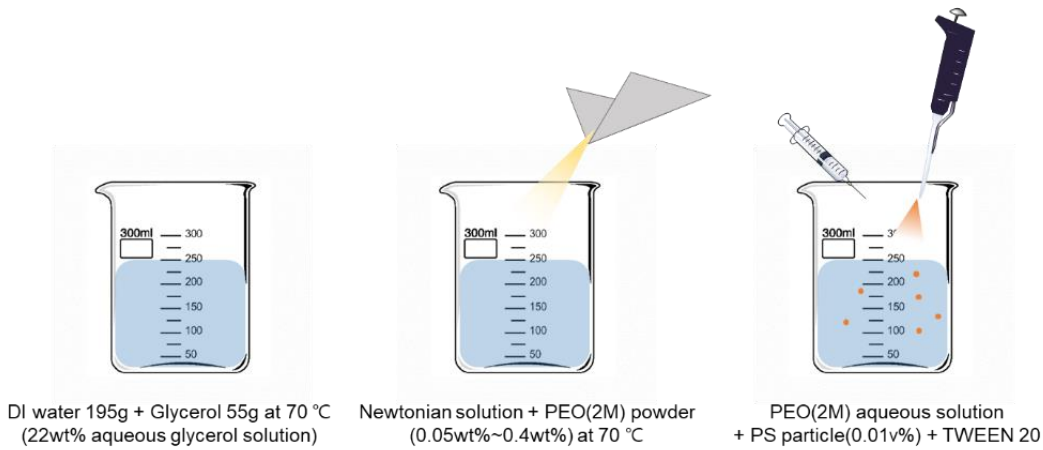

Figure 2.2. Sample solution preparation. By mixing DI water and glycerol, 22 wt % aqueous glycerol solution is initially prepared as Newtonian solution. Polyethylene oxide powder is resolved into the Newtonian solution with different weight fraction from 0.05 to 0.4 at high temperature. Finally, microparticles and surfactant are suspended into viscoelastic solutions.

2.2.3. Flow characterization

Dilute polyethylene oxide (PEO) solution is used as a viscoelastic medium due to its viscous and elastic properties. The rheological properties of viscoelastic solutions such as the steady shear viscosity (η) and the relaxation time (λ) are measured by a rotational rheometer (MCR-301, Anton Paar) and a capillary breakup extensional rheometer (CaBER-1, ThermoHakke), respectively. PEO solutions with different PEO concentrations ranging from 500 to 4000 ppm were prepared. It is observed that the viscosity and the relaxation time increase with increasing the PEO concentrations in the medium (**Figure 2.3** and **Table 2.1**). It is shown that the shear-thinning effects are clearly negligible as the PEO concentrations are in the range of 500 to 2000 ppm. For 2500 and 3000 ppm solutions, the shear thinning effect becomes obvious. Indeed, the significant shear-thinning behavior is clearly observed for PEO concentrations exceeding 3500 ppm (**Figure 2.3**). We aim to exclude any shear-thinning effects on particle migration so that 2000 ppm PEO solution was mainly used in our experimental and theoretical studies. The relaxation times of the PEO solutions were characterized by fitting with the Bird-Carreau viscosity model. The Bird-Carreau model is defined as $(\eta - \eta_\infty)/(\eta_0 - \eta_\infty) = (1 + (\lambda\dot{\gamma})^a)^{(n-1)/a}$, where η_∞ is the infinite shear viscosity, η_0 is the zero-shear viscosity, a is the dimensionless parameter for the transition from zero-shear rate region to power-law region, and n is the power-law index. The fluid relaxation time of the PEO solutions was measured by using a CaBER instrument, and were compared with the Bird-Carreau model. The relaxation time measured by the CaBER was listed in Table 1. Furthermore, the relaxation time estimated by the Bird-Carreau model was provided with a 95% confidence interval for each parameter,[45,46] and were compared with the fitting model of the concentration-dependent relaxation time for dilute polymer solutions (**Figure 2.4**).[47]

In a dilute entangled polymer solution where the polymer concentration $c > c^* = 3M/4\pi N_A R_g^3$, the longest relaxation time λ depends on the polymer concentration c due to the polymer interactions between different chains as $\lambda = \lambda_0[1 + cA - \sqrt{2}(cA)^{1.5} + 2(cA)^2]$.[47,48] Here, M is the molar mass, N_A is the Avogadro number, and $R_g = 0.0215M^{0.583\pm0.031}$ is the radius of gyration in a dilute solution,[49,50] λ_0 is the longest relaxation time at an infinite dilution, and $A \approx 0.5[\eta]$ is a scaling parameter. For our PEO solutions, R_g is calculated to be 100 nm and c^* is 790, and that the concentration-

dependent relaxation time model in a dilute polymer solution can be applied when the polymer concentration $c > c^*$. It is found that the relaxation time fitting model shows good agreement with the experimental values. The relaxation time tends to have wide error bars as the polymer concentrations are below 2000 ppm due to the weak shear-thinning effect (please see **Figure 2.4**).

The particle migration in the viscoelastic fluid is determined by the combination of the elasticity and inertia of the fluid.[18] The Reynolds number, *Re*, is a dimensionless number that accounts for the relative importance of inertial and viscous effects, which can be defined as

$$Re = \frac{\rho u D_h}{\eta} = \frac{2\rho Q}{\eta(W+H)} \tag{2-1}$$

, where *H* is the channel height, *W* is the channel width, ρ is the fluid density, *u* is the fluid velocity, and $D_h = 2WH/(W+H)$ is the hydraulic diameter of rectangular channel. The elastic effect of flow is represented by the Weissenberg number, *Wi*, which encompasses the relaxation time (λ) and the characteristic shear rate ($\dot{\gamma}_c$). *Wi* is defined as

$$Wi = \lambda\dot{\gamma}_c = \frac{2\lambda Q}{HW^2} \tag{2-2}$$

, where $\dot{\gamma}_c = 2U/W = 2Q/HW^2$. The fluid elasticity is characterized by the competition between *Re* and *Wi*. The elasticity number (*El*) is defined as

$$El = \frac{Wi}{Re} = \frac{\lambda\eta(W+H)}{\rho W^2 H}. \tag{2-3}$$

When the viscoelastic fluid has no apparent shear-thinning effect, *El* becomes independent of the flow rate and only depends on the viscosity of fluid and the relaxation time in a specific channel. The elastic force becomes more dominant than the inertial force as *El* becomes larger than unity. Since our experiments were carried out in the range of $0.35 < Re < 30.07$ and $1.668 < Wi < 57.715$, the resulting elasticity of the viscoelastic fluid is described with $0.66 < El < 13.36$. Typically, single-line particle focusing in a viscoelastic fluid occurs when $El > 1$.[6-19]

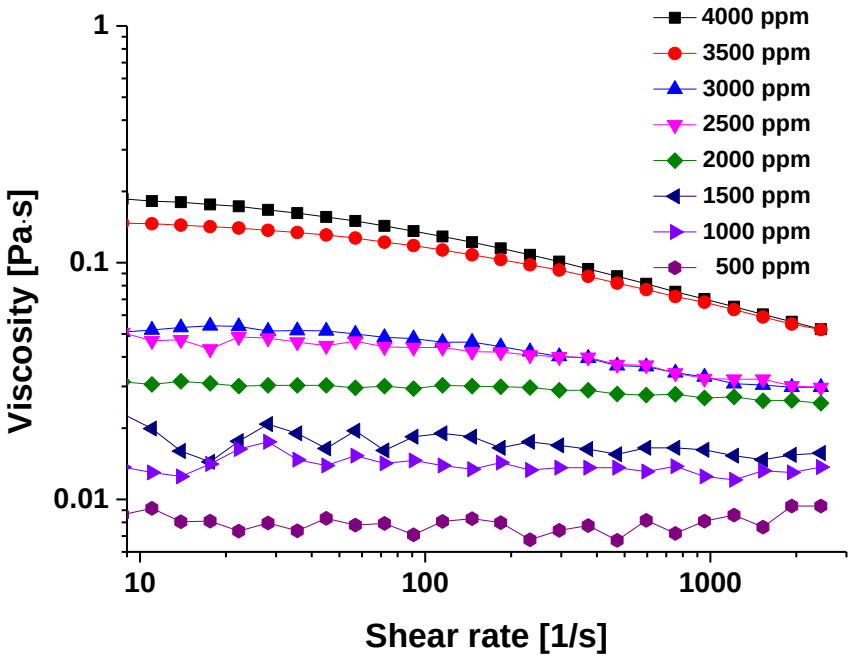

Figure 2.3. Viscosities of diluted PEO viscoelastic solutions with respect to different PEO concentrations.

Table 2.1. Rheological properties of diluted PEO viscoelastic solutions. The fitting parameters of *a*, *n,* and λ_{mean} for the Bird-Carreau viscosity model represent the mean values of the transition from zero-shear rate region to power-law region, the power-law index, and the mean value of relaxation time, respectively. The relaxation time is measured experimentally by using a capillary breakup extensional rheometer (CaBER).

Polymer concentration [ppm]	**Bird-Carreau model**			**CaBER**
	a	***n***	***λmean* [s]**	**λ_{mean} [s]**
500	0.00137	0.98817	0.01404	0.015
1000	0.02817	0.95559	0.01959	0.0184
1500	0.06303	0.93016	0.01918	0.0198
2000	0.94246	0.89214	0.02206	0.0217
2500	1.21754	0.68414	0.02302	0.0232
3000	2.19084	0.61134	0.02352	0.0243
3500	2.47148	0.58312	0.03296	0.0338
4000	2.63601	0.56314	0.04009	0.0432

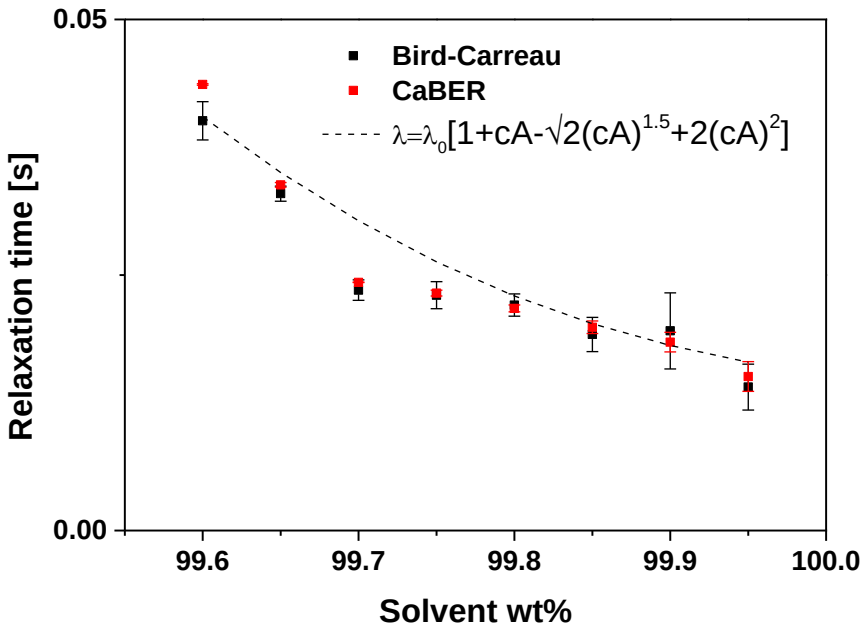

Figure 2.4. Relaxation time λ as a function of solvent weight percent. Red symbols represent the experimental data obtained by a CaBER instrument. The experimental data was compared with the Bird-Carreau model (black symbols) derived from a viscosity fitting. Error bars for the black symbols are derived from a 95% confidence interval. Dashed line is a curve fitting from the concentration-dependent relaxation time model for dilute polymer solutions.

2.3. Numerical analysis

We carried out numerical simulation to analyze the effect of channel aspect ratios on the first normal stress difference. Since the first normal stress difference $(N_1 = \tau_{xx} - \tau_{yy})$ of the solution is much higher than the second normal stress difference $(N_2 = \tau_{yy} - \tau_{zz})$, the first normal stress difference is a major driving force for the particle migration together with the inertial force.[4,5] For the simulation, the steady-state momentum equation is expressed as

$$\rho\left(\frac{\partial \boldsymbol{u}}{\partial t} + (\boldsymbol{u}\cdot\nabla)\boldsymbol{u}\right) = \nabla\cdot(-p\boldsymbol{I} + \eta_s(\nabla\mathbf{u} + (\nabla\boldsymbol{u})^T) + \boldsymbol{T}) \quad (2\text{-}4)$$

and the extra stress contribution (upper convective Maxwell model) is defined as follow

$$\mathbf{T} + \lambda\left(\frac{\partial \boldsymbol{T}}{\partial t} + (\boldsymbol{u}\cdot\nabla)\boldsymbol{T} - [(\nabla\boldsymbol{u})\cdot\boldsymbol{T} + \boldsymbol{T}\cdot(\Delta\boldsymbol{u})^T]\right) = \eta_p(\nabla\mathbf{u} + (\nabla\boldsymbol{u})^T) \quad (2\text{-}5)$$

, where u is the velocity vector, λ is the characteristic relaxation time, η_p and η_s are the viscosities of polymer and solvent, and the total viscosity (η) is $\eta_p + \eta_s$. These two equations are solved along with the continuity equation to confirm the effect of N_1 distribution according to channel aspect ratio. The normal stress τ_{yy} was subtracted from τ_{xx} to obtain N_1, and then N_1 was normalized with its maximum value to compare the values of N_1 with different channel aspect ratios.

Shear gradient lift forces acting on the particles for different channel aspect ratios were also predicted numerically to understand the force balance between the inertial force and the shear gradient lift force. The shear gradient lift force is defined as

$$F_L = f_L\rho u^2 a^3/W \quad (2\text{-}6)$$

, where f_L is the dimensionless coefficient, ρ is the fluid density, u is the fluid velocity, a is the particle diameter, and W is the channel width.[51] From the numerical calculation, the lateral fluid velocity u is obtained. Then, the shear gradient lift force is calculated together

with the particle diameter $= 15\ \mu$m, the channel width $W = 25,\ 50$ and 100 μm, the fluid density ρ = 1 g/cm^3, and the dimensionless coefficient f_L = 0.5. For most microfluidic applications, the lift coefficient remains to be constant, which is approximated as $f_L \sim 0.5$ at $Re < 100$.[52]

2.4. Results and Discussion

2.4.1. Multiple particle focusing behavior

It has been reported that particles were aligned along the centerline of a straight channel under pressure-driven flow by adding the so-called elasticity enhancers such as polymers and DNAs.[10,11,21,53–55] Particles in a 1:1 aspect ratio rectangular channel are focused at the center and four corners when *El* is on the order of 10^2 for inertia-less flow. When *El* becomes on the order of 10^1, the number of the multiple equilibrium positions is reduced to one equilibrium position at the centerline of the channel.

Here, we designed a rectangular channel with double inlets and 4:1 aspect ratio for the formation of multiple-line particle focusing (**Figure 2.5**). The inertial and elastic forces are altered depending on the channel aspect ratio, which may create different equilibrium particle positions as a result of the force balance between them. 2000 ppm PEO aqueous solution was injected into the double inlet channel with the flow rate of 0.3 ml/hr. Once the particles are introduced, they start to migrate towards the centerline due to the fluid elasticity. However, the two lines do not merge at the center due to the fact that the shear gradient force pushes the particles away from the centerline of the channel. For a 1:1 aspect ratio rectangular channel, the double-line focusing is not found because the elastic force outweighs the shear gradient force. It should be noted that the particles are easily aligned in double-line as they are introduced through two inlets since the shear gradient force at the center becomes high when the flows from the two inlet meet at the straight channel. Consequently, the particles introduced into the two inlets are aligned along the two different equilibrium focusing positions.

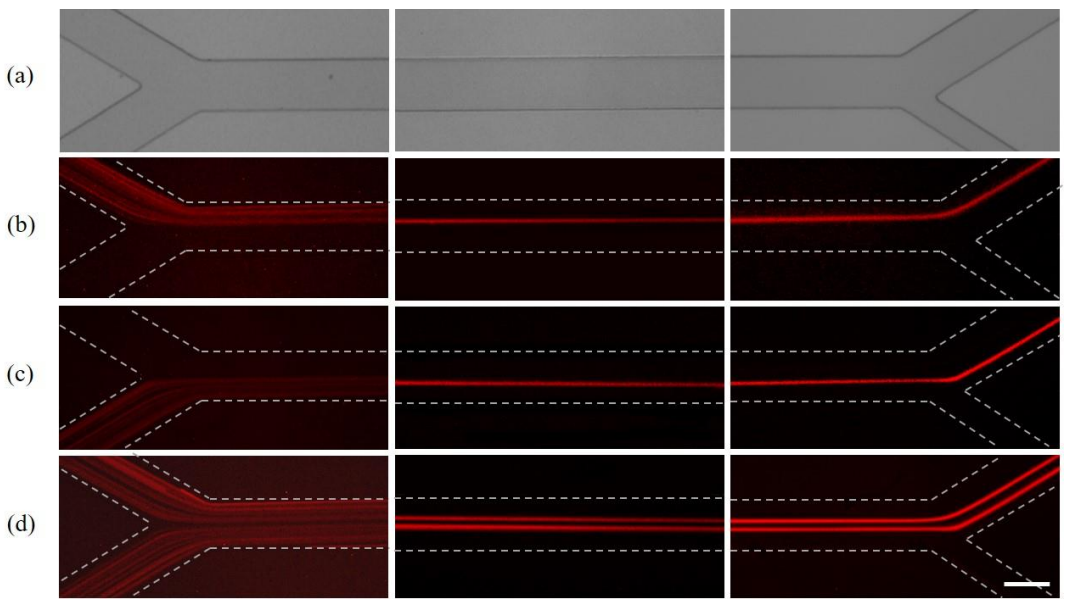

Figure 2.5. Particle focusing behavior in the 4:1 double inlet channel: (a) Bright field image of the channel. 2000 ppm PEO solution with fluorescent PS particles was injected into the channel with the flow rate of 0.3 ml/hr. (b) and (c) Particles are introduced into the upper and lower channel inlets, respectively. (d) Particles are introduced into both channel inlets. The particles are focused at the specific locations in the channel. The asymmetrical outlet is designed to clarify the multiple-line particle focusing at the channel outlet. Scale bar = 100 μm.

2.4.2. Channel aspect ratio effect

The elastic force acting on the particles can be estimated using the first normal stress difference (N_1) of viscoelastic fluids such as PEO and PVP solutions. The elastic force is evaluated with use of $F_E \sim a^3 \nabla N_1$, where a and N_1 are the particle diameter and the first normal stress difference, respectively. The scaling law of the elastic force is derived from the gradient of the first normal stress difference $N_1 = \tau_{xx} - \tau_{yy}$. Particles suspended in viscoelastic solutions can be affected by the gradient of τ_{xx} and the gradient of τ_{yy} along the y-direction. Furthermore, the second normal stress differences $N_2 = \tau_{yy} - \tau_{zz}$ is not a trivial factor for lateral particle migration in Poiseuille flow.[13,17] Due to the complexity, many researchers neglect the N_2 contribution and assume the transverse elastic force exerted on the particle is proportional to the gradient of N_1.[13,18] Here, we also used a scaling law as $F_E \sim a^3 \nabla N_1$. We confirm that the normalized N_1 shows the lowest values at the center of the cross-section ($y/L = 0$) for 1:1, and 2:1 channel aspect ratios (**Figure 2.6**). On the other hand, the normalized N_1 for the 4:1 channel aspect ratio has a wide range of the minimal value along the centerline in the y-direction range of $-0.5 < y/L < 0.5$. Therefore, the particles in the 1:1 aspect ratio channel are focused preferably at the center compared to the other channels. For the rectangular channel, it was already reported by other researchers that the particles are focused at the center due to high elastic force of the fluid ($El \sim O(2)$).[6,18,44]

We observed the transition from the single-line particle focusing to the multiple-line particle focusing for the first time in this study, and demonstrated the effect of the gradient lift force and the effect of particle sizes. It is shown that the gradient of the first normal stress difference remains unchanged in the range of $-0.5 < y/L < 0.5$ at the centerline of the cross-section as the channel aspect ratio becomes high, which can generate the broad in-plane particle focusing (**Figure 2.6 (b)**). Whereas the shear gradient lift force is a parabolic function along the centerline of the cross-section even though the channel aspect ratio becomes high, the particles can migrate towards the side walls of the channel (**Figure 2.7**). In addition, the particle migration towards the side walls is more obvious when the particle size becomes larger since the shear gradient lift force depends on the volume of the particle (**Figure 2.8 (a)** and **2.8 (b)**). We measured the rheological properties of 2000 ppm PEO

solution to calculate *Wi* and *Re* with different channel aspect ratios. The viscosity and the relaxation time of the fluid are measured to be 27.4 mPa·s and 21.7 ms, respectively. The normalized fluorescence intensity peaks represent the particle focusing locations along the lateral position. For the 2:1 aspect ratio channel, a single-line particle focusing at the center is detected when *El* is 6.77 (**Figure 2.9**). A large elasticity number indicates that the elastic force is stronger than the inertial force in the rectangular channel. The double-line focusing of the particles becomes visually discernible as the *Wi* reaches 77.078. For the 4:1 aspect ratio channel, it is remarkable that the double-line focusing becomes more clear at low *El* (*Wi/Re* = 2.82) (**Figure 2.10**). From these results, we understand that the double-line particle focusing is associated with the competition between the elastic and inertial forces depending on the channel aspect ratio. In this sense, the effect of channel aspect ratio should be considered to understand the mechanism of the multiple-line particle focusing in the microchannel.

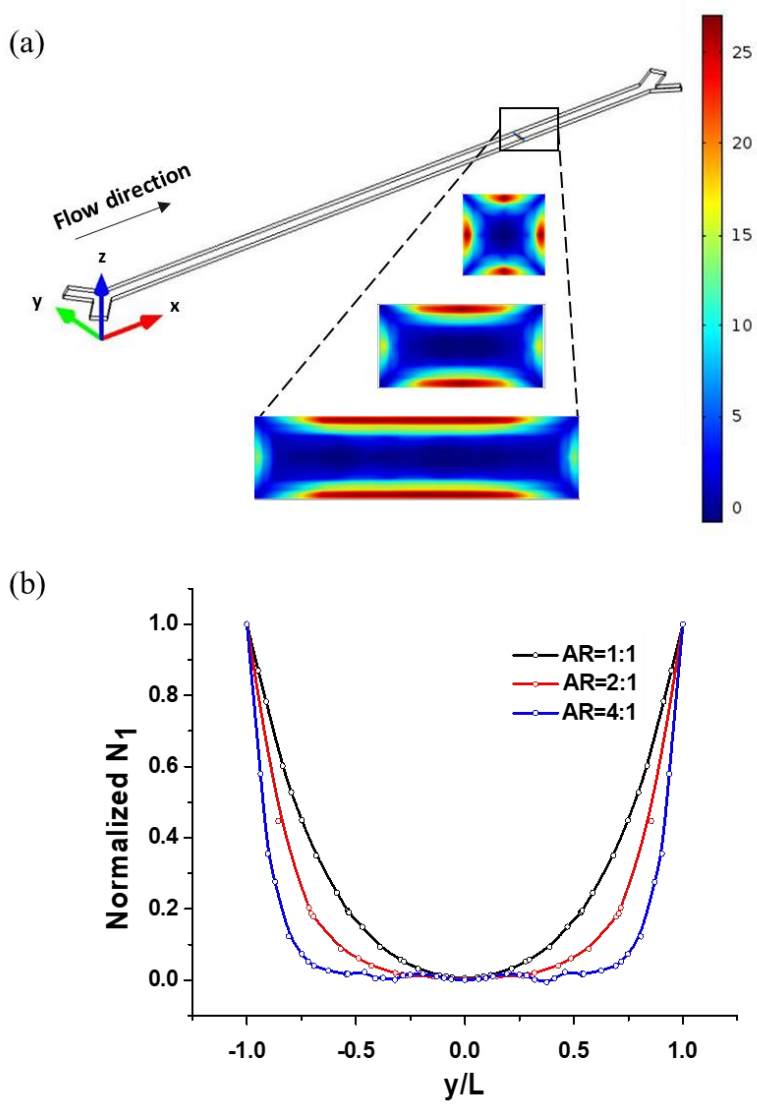

Figure 2.6. Analysis of multiple-line particle focusing: (a) First normal stress difference (N_1) in the cross-sectional area was obtained by numerical simulation. (b) Higher channel aspect ratio leads to broader plateau region of N_1.

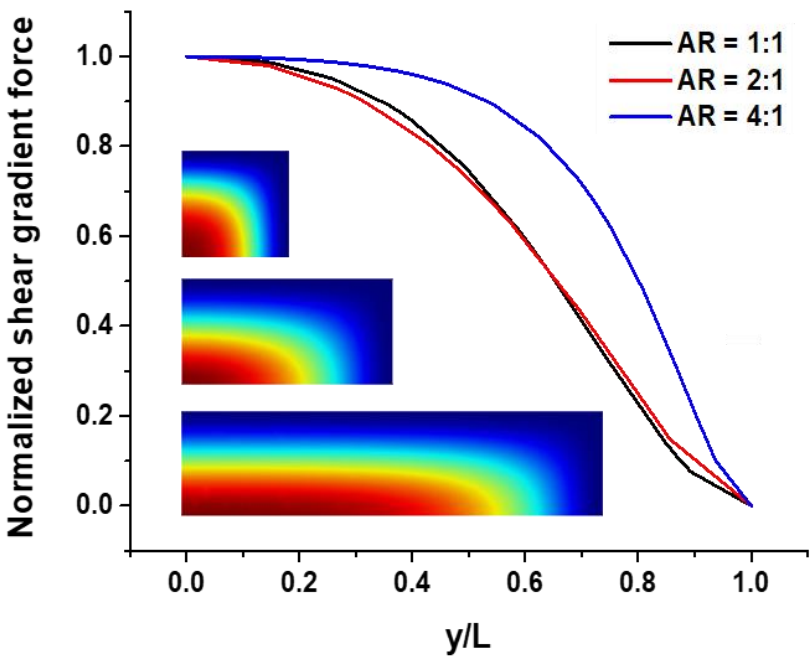

Figure 2.7. Normalized shear gradient lift forces with different channel aspect ratios, assuming that the particle size is 15 μm, the fluid density is 1 g/cm^3, and the dimensionless coefficient f_L is = 0.5.

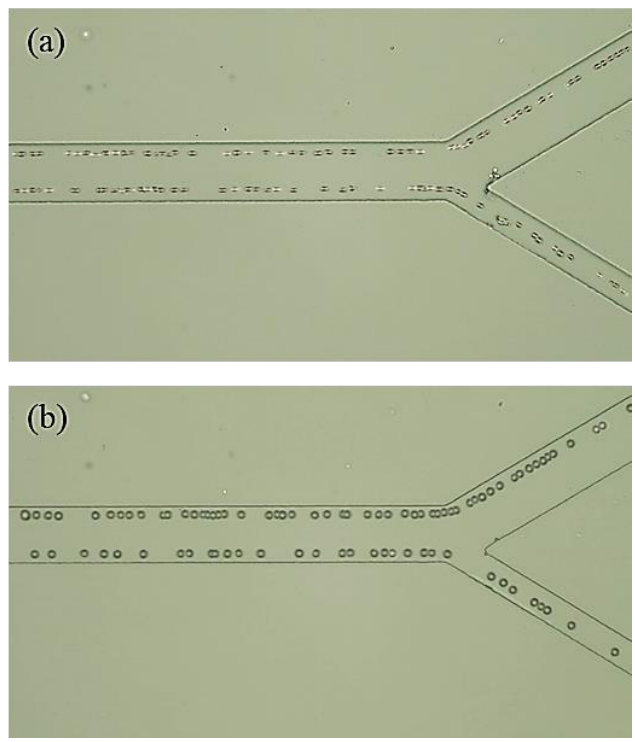

Figure 2.8. Particle migration in 2000 ppm PEO solution with the flow rate of 0.3 ml/hr depending on the particle sizes of (a) 10 μm and (b) 15 μm. A hundred of images are superposed for better observation of the particle migration.

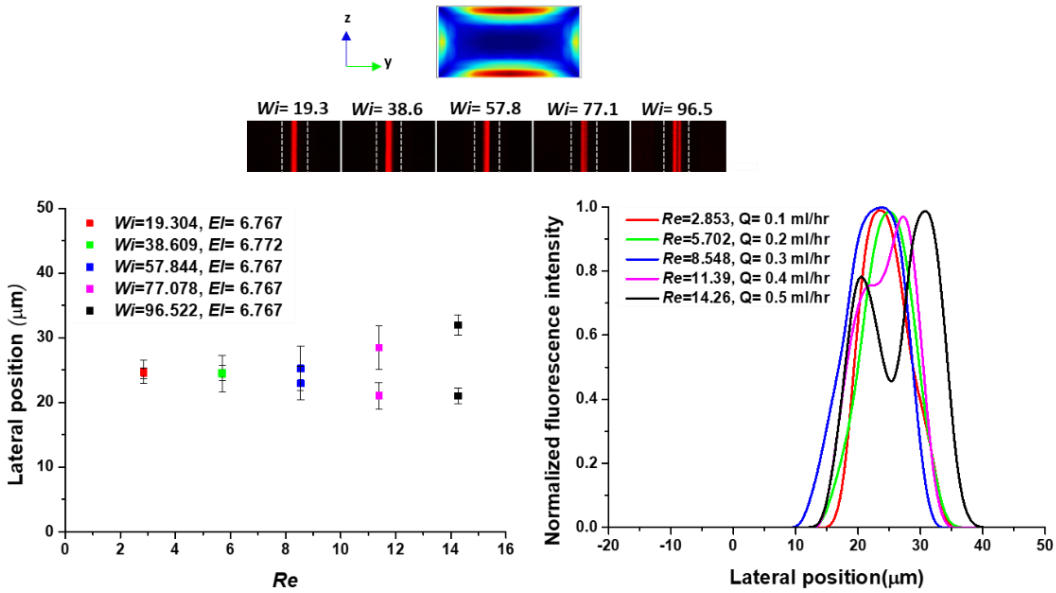

Figure 2.9. Particle equilibrium positions in 2:1 aspect ratio channel with double inlets. The distance between the two lines increases with an increase of the flow rate. Scale bar = 50 μm.

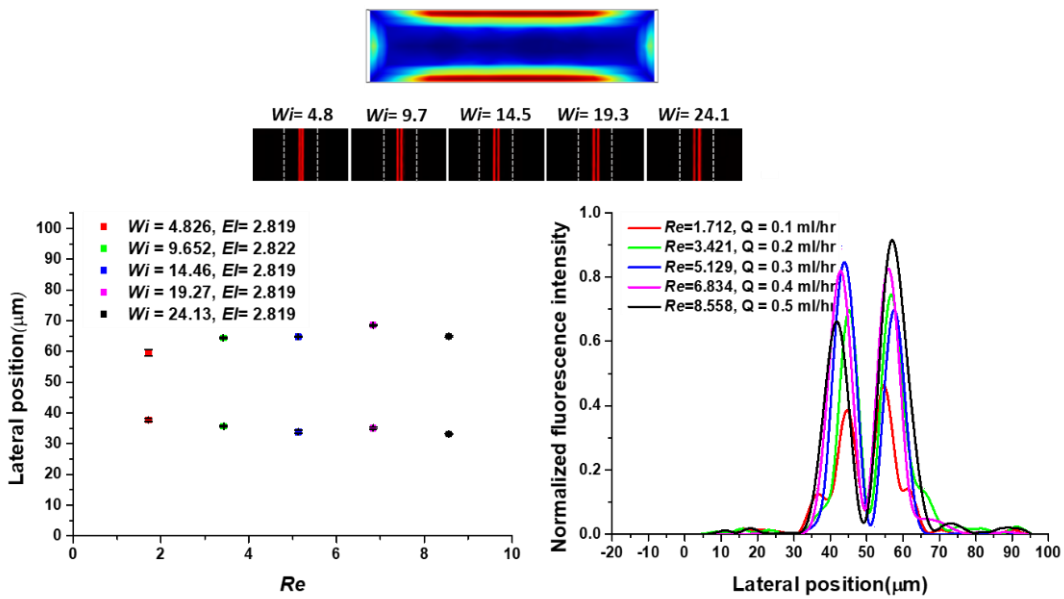

Figure 2.10. Particle equilibrium positions in 4:1 aspect ratio channel with double inlets. The two peaks of fluorescence intensity are observed over the entire *Wi* and *Re* ranges for the 4:1 aspect ratio channel. The distance between the two lines increases with an increase of the flow rate. Scale bar = 50 μm.

2.4.3. Polymer concentration effect

Polymer concentration in a non-Newtonian solution determines the viscoelastic properties of the solution when it flows through the confinement. Generally, the elasticity (*El*) increases with increase of the polymer concentration. In this study, we demonstrated that the flow is strongly influenced by the geometric effect. Although the particle suspension is injected into the high aspect ratio microchannel, the multiple line particle focusing behavior and gap between the focusing lines can be manipulated by the polymer concentration.

As shown in **Figure 2.11** and **Table 2.2**, the location and the number of particle focusing lines can be systematically tuned by changing the flow rate and the concentration of fluid. Under the fixed flow rate, 0.3 ml/hr, the polymer concentration is varied from 1500 ppm to 4000 ppm in order to examine the elasticity effect of the medium for the multiple particle focusing. When the concentration of the PEO solution is 1500 ppm, the double-line particle focusing is observed near the channel sidewall. When the elastic force generated by the elasticity of fluid is comparably smaller than the inertial force, the particles tend to migrate towards the channel sidewall (**Figure 2.12**). The distance between the two lines decreases with increasing the concentration of the PEO solution. When the concentration increases to 2500 ppm (El = 3.322), the particles are double-focused with shorter gap comparing to the double focusing in 1500 ppm solution (**Figure 2.13**). When the concentration becomes 3500 ppm (El = 10.05), the single-line particle focusing is observed (**Figure 2.14**). Focusing locations for each solution were evaluated by image processing by using particle fluorescence intensity analysis. In addition, the two particle focusing lines become estranged from each other as the flow rates increase as image processing results in **Figure 2.15**. This demonstrates that the double-line particle focusing occurs when the inertial force outweighs the elastic force at the same *El*, resulting in the particle migration towards the channel sidewall. On the contrary, as the fluid elasticity further increases (*i.e.*, *El* dominates), the particles move toward the centerline due to the increased elastic force. This leads to the single-line particle focusing as shown in **Figure 2.15**. Indeed, the double-line particle focusing is quasi-stable, which can be tuned by the elastic force of the fluid.

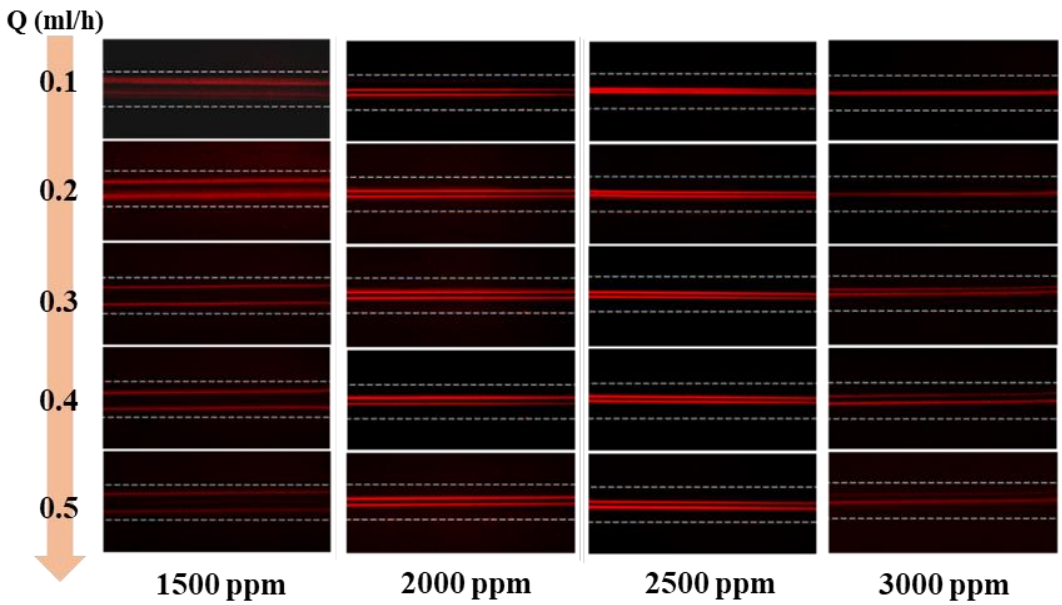

Figure 2.11. Double line particle focusing behavior under different concentration and the flow rate.

Table 2.2. Double line particle focusing behavior according to the polymer concentration (c [ppm]) and the flow rate (Q [ml/h]).

c \ Q	0.1	0.15	0.2	0.25	0.3	0.35	0.4	0.45	0.5	0.55
500	x	x	x	x	x	x	=	=	=	=
1000	x	x	x	x	x	x	=	=	=	=
1500	=	=	=	=	=	=	=	=	=	=
2000	=	=	=	=	=	=	=	=	=	=
2500	=	=	=	=	=	=	=	=	=	=
3000	-	-	-	-	=	=	=	=	=	=
3500	-	-	-	-	-	-	x	x	x	x
4000	-	-	-	-	-	-	-	x	x	x

x : No focusing behavior
= : Double line focusing
- : Single line focusing

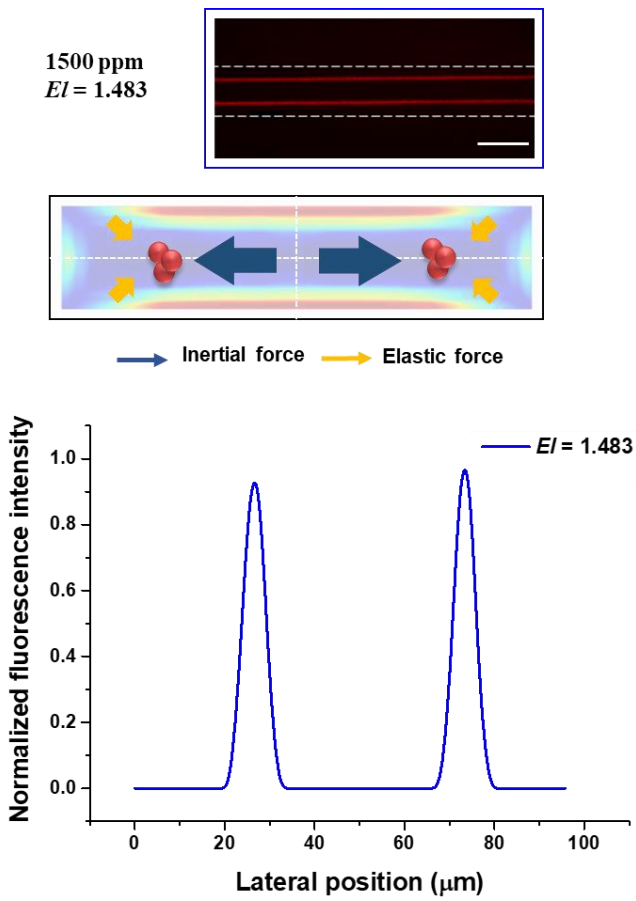

Figure 2.12. Particle focusing location in 1500 ppm PEO solution and force competition scheme in 4:1 microchannel. Scale bar indicates 100 μm.

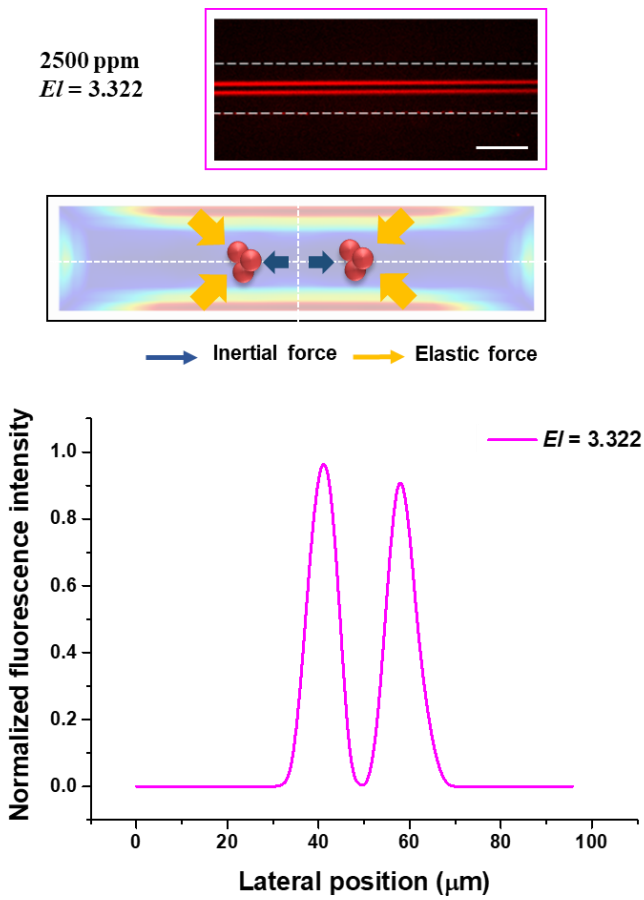

Figure 2.13. Particle focusing location in 2500 ppm PEO solution and force competition scheme in 4:1 microchannel. Scale bar indicates 100 μm.

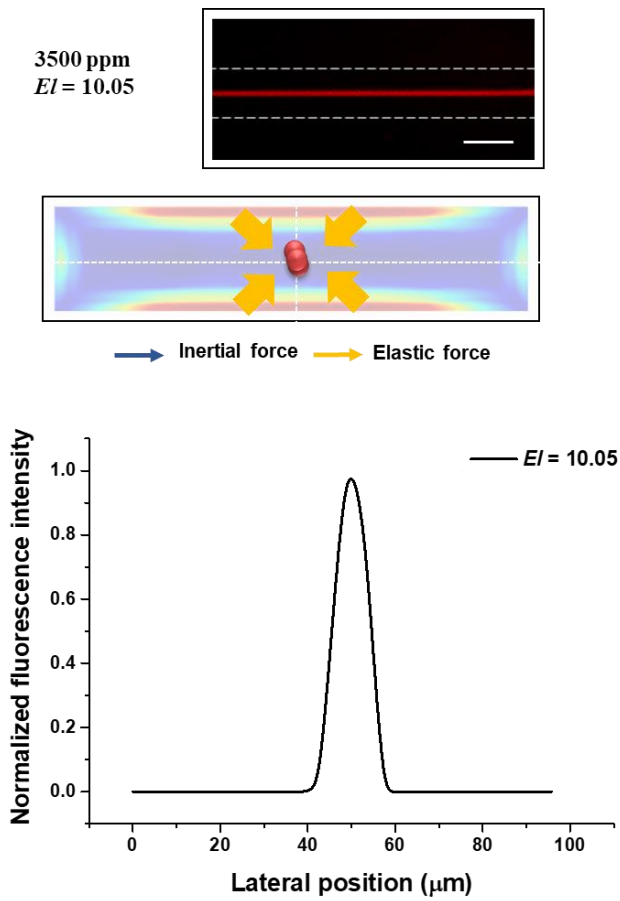

Figure 2.14. Particle focusing location in 3500 ppm PEO solution and force competition scheme in 4:1 microchannel. Scale bar indicates 100 μm.

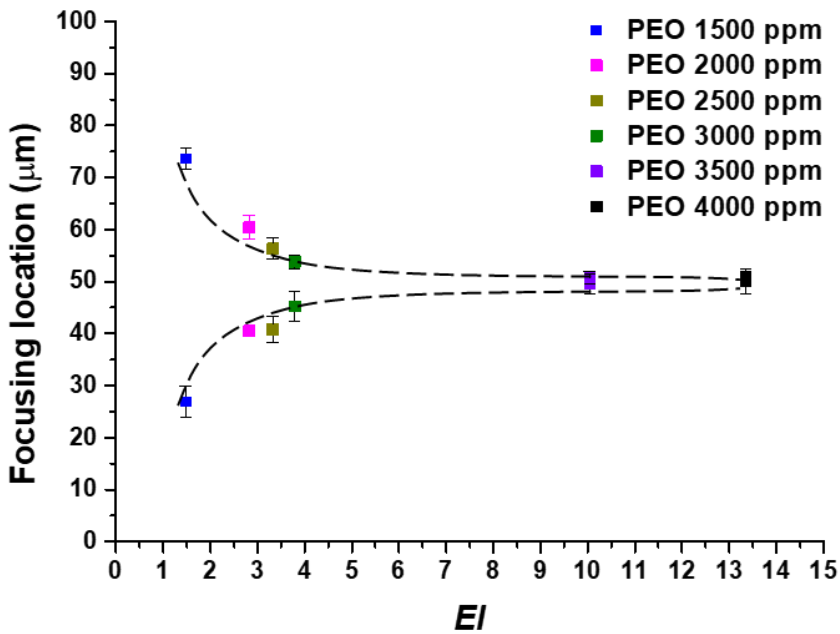

Figure 2.15. Plot of the focusing location as a function of *El*. As the fluid elasticity increases, the distance between the particle equilibrium positions decreases.

2.4.4. Channel inlet number effect

Previously, we explored the double line particle focusing behavior and mechanism by using a 4:1 rectangular microchannel with double inlets. And the double inlets induces wall-repulsion force and shear-gradient force at initial injected flow. These hydrodynamic forces allow the double line particle focusing at the downstream. Similar to the double line particle focusing experiment, another 4:1 rectangular microchannel with triple inlets was designed in order to confirm the inlet number effect for the multiple line particle focusing. The multiple-line focusing can be clarified as the particles are introduced at multiple inlets. (**Figure 2.16**). The particles suspended in the upper inlet are prone to align close to the top sidewall, creating a single-line particle focusing (**Figure 2.16 (a)**). When the particles are introduced through the multiple inlets, the multiple-line particle focusing is identified (**Figure 2.16 (c)**). The constriction of Y-shaped inlet bifurcates the streamlines of the particles that are introduced through the inlet, which can facilitate the multiple-line particle focusing in the straight channel. From these results, we confirm that the formation of the multiple-line particle focusing can be facilitated by the inlet geometry, *e.g.*, the number of channel inlets. The double-line particle focusing can also be observed in the single inlet channel with the 4:1 aspect ratio (**Figure 2.17**), meaning the inlet geometry is not a prerequisite factor but enhances the double-line focusing efficiently. The particles are pushed towards the channel walls due to the shear gradient lift force. When the shear gradient force outweighs the elastic force, the particles are finally aligned along the channel walls by the fluid elasticity at $El \sim 2.82$. The shear gradient lift force exerted on the particles is dependent on their particle sizes.[12,18,27,38,42] We also observed that the particle migration towards the side walls is more obvious when the particle size becomes larger (**Figure 2.8 (a)** and **2.8 (b)**).

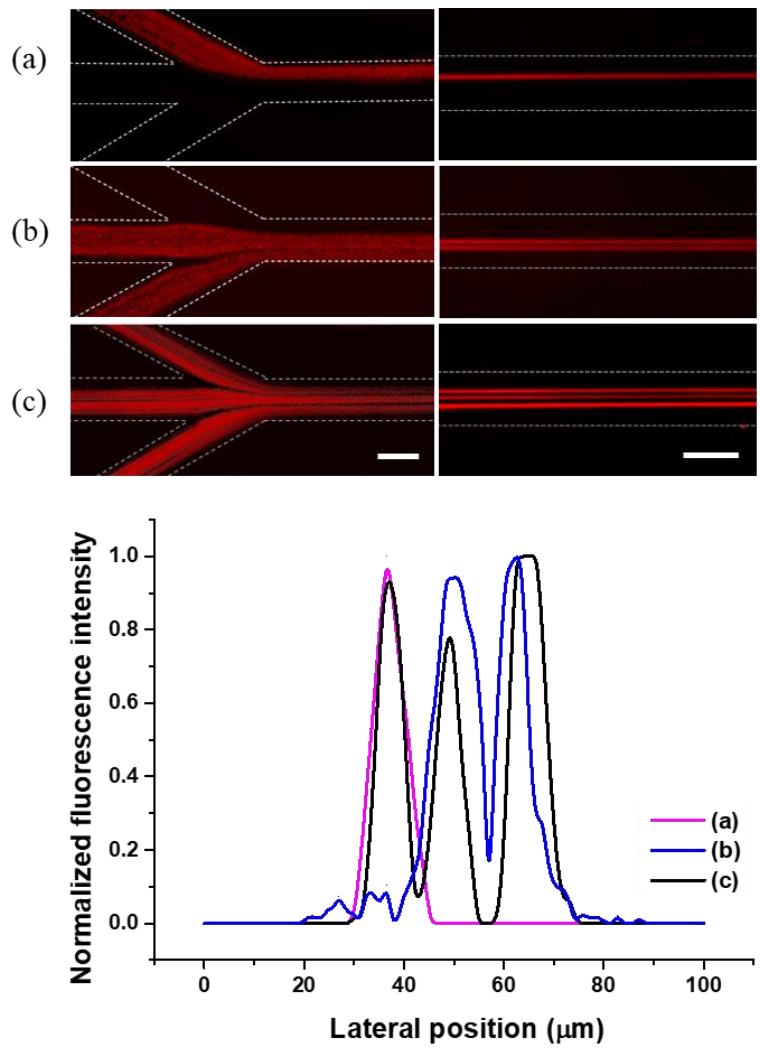

Figure 2.16. Multiple-line particle focusing in the triple-inlet microchannel: (a) Particles introduced into the upper inlet are aligned at a single position close to the top sidewall. (b) Particles injected through the middle and lower inlets are focused at the two different positions in the channel. (c) The three inlet channel generates the triple-particle focusing lines in the downstream channel. Scale bar = 100 μm.

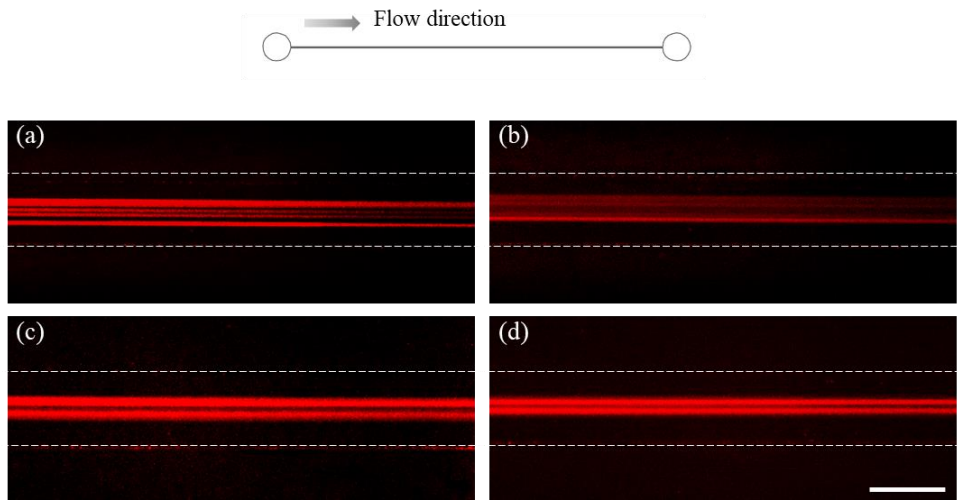

Figure 2.17. Particle focusing behavior in a single-inlet straight channel. (a - b) In 4:1 channel aspect ratio, particles are widely distributed at low flow rates (from 0.1 to 0.3 ml/hr). (c) The wide band is narrowed and becomes a double-line particle focusing when the flow rate exceeds 0.4 ml/hr. (d) The double-line particle focusing is formed when the flow rate is 0.5 ml/hr. The double-line particle focusing in the single-inlet straight channel is not as much obvious as in the double-inlet straight channel. Scale bar = 100 μm.

2.4.5. *Re – Wi* working space for multiple focusing

Our experimental results re-confirm that the particles suspended in a viscoelastic medium migrate towards the centerline of the channel due to the elastic force. However, if the inertial force becomes more dominant than the elastic force in high aspect ratio channels especially, the particles migrate towards the channel sidewalls, leading to the multiple-line particle focusing. It is confirmed that the multiple-line particle focusing is mainly generated by the force balance between the elastic and inertial forces, and can be facilitated by the geometry effect. The flow conditions in the concentration ranges of 500 to 2000 ppm PEO solutions do not occur any elastic or shear flow instability which may affect the equilibrium positions of the particles. To confirm this, we introduced a food dye and fluorescent PS particles through the upper inlet, and non-fluorescent PS particles through the lower inlet (**Figure 2.18**). There is no elastic or shear flow instability at the interface while molecular diffusion is achieved at the outlets (**Figure 2.18 (a)**). The fluorescent particles introduced through the upper inlet are focused at the off-centered line close to the upper sidewall, while the non-fluorescent particles introduced through the lower inlet are focused close to the lower sidewall (**Figure 2.18 (b)**). This result convinced us that the mechanism of the multiple focusing is based on the effect of channel geometry (*e.g.*, number of inlets and channel aspect ratio). An illustration of the focusing mechanism is described in **Figure 2.19**.

The relative importance of elastic and inertial forces in the flow can be captured quantitatively with the elasticity number (**Figure 2.20**). Most of previous studies on the particle migration in viscoelastic fluids focused on highly elastic fluids (El>>1). Lim *et al*. recently observed particle migration in weakly elastic fluids (El~0.1) towards the channel centerline over a wide range of $10^1 \leq \mathrm{Re} \leq 10^4$.[14] When El is larger than unity, the inertial force is overwhelmed by the elastic force. In our study, the particle migration is observed in the range of $10^{-1} \leq El \leq 10^1$ with different channel aspect ratios (**Figure 2.20 (a)** and **2.20 (b)**). Interestingly, we observe the transition between the multiple-line and single-line particle focusing within the flow conditions. Note that the multiple-line particle focusing is generated even at a low fluid elasticity (El~1.483) by not only the channel geometry but also the elasto-inertial force balance of a fluid. We anticipate that this study will help design microfluidic platforms for the enrichment and separation of micro and nanoparticles encountered in a variety of applications of biology, chemistry, and nanotechnology.

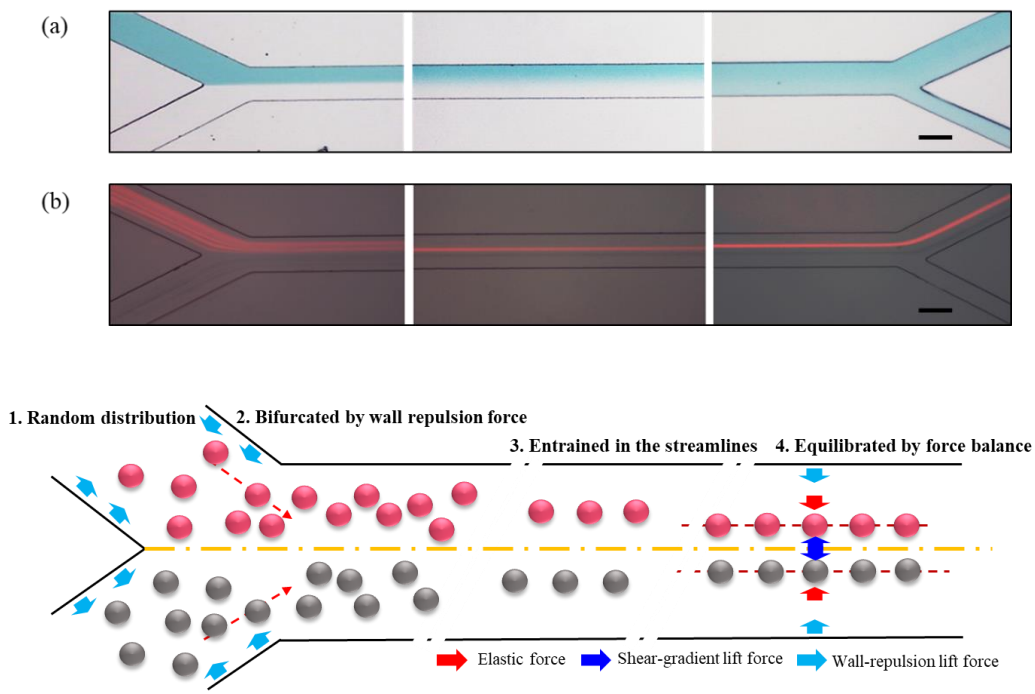

Figure 2.18. Inlet number effect verification. (a) A food dye is injected into the upper inlet channel. Molecular diffusion is completed at the channel outlet. (b) Fluorescent and non-fluorescent PS particles are introduced into the upper and lower inlets, respectively. Fluorescent particles (in red) are focused at the off-centered line close to the upper sidewall while non-fluorescent particles (in dark) are focused at the off-centered line close to the lower sidewall.

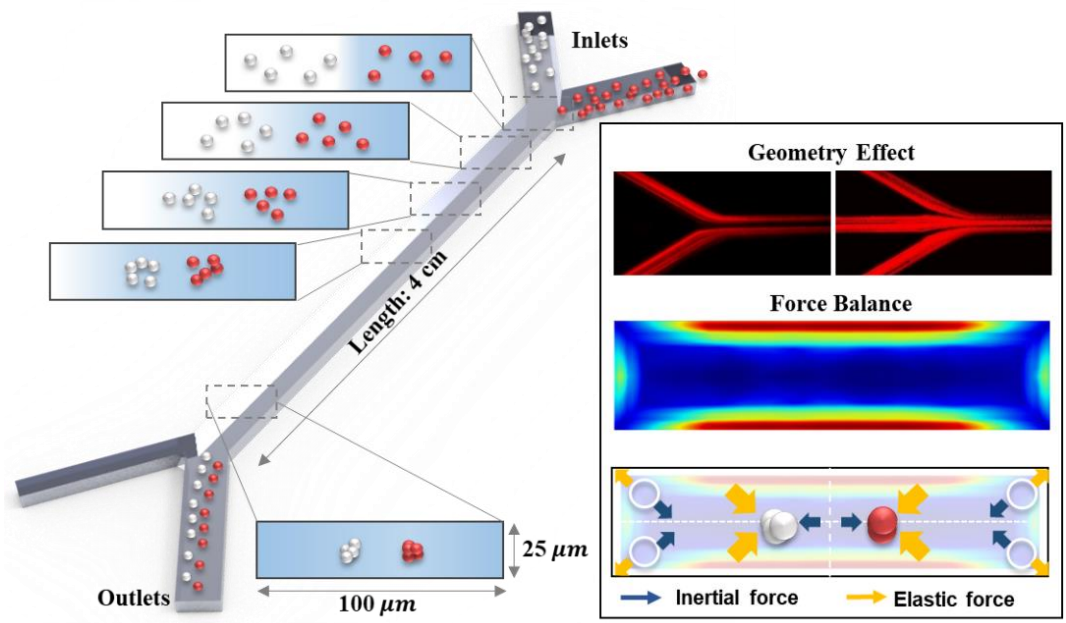

Figure 2.19. Effect of the inlet geometry of channel and the force balance between inertial and elastic forces for the multiple-line particle focusing: Schematic illustration of the geometry effect and the force balance. The multiple-line particle focusing is generated along with the molecular diffusion of the viscoelastic medium.

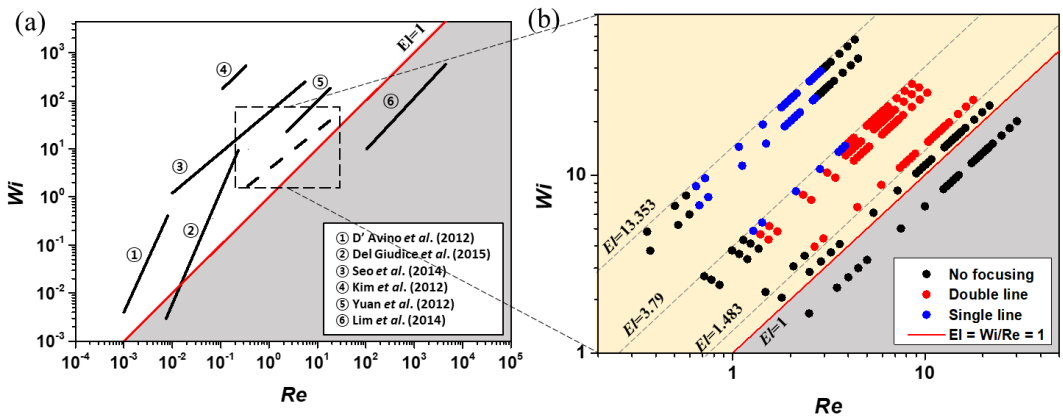

Figure 2.20. *Re* – *Wi* working space for the multiple-line particle focusing in the straight microchannels: (a) The red line represents that the elasticity number (*El*) is unity. The values of $El > 1$ indicates elasticity-dominant flow, whereas the values of $El < 1$ indicates inertia-dominant flow. The black lines correspond to the range of *Wi* and *Re* reported by different researchers. The previous studies were mostly carried out in the elasticity-dominant flow ($El > 1$). The dashed line corresponds to the range of *Wi* and *Re* explored in this study. (b) Magnified view of our experimental conditions. The blue dots and the red dots represent single-line and double-line particle focusing in the microchannel, respectively.

2.5. Summary

We investigated the multiple-line particle focusing by tuning elastic and inertial forces acting on particles suspended in a viscoelastic fluid. The effects of the channel geometry and aspect ratio on the particle focusing were examined. Numerical analysis was conducted to understand the underlying physics behind the particle focusing in a viscoelastic fluid. From the simulation we confirmed that the minimal region of the first normal stress difference became wider as the channel aspect ratio became higher, resulting in a wide distribution of the particle focusing in the mid-plane of the channel. The transition from the single-line to the double-line particle focusing occurred when the inertial force overwhelmed the elastic force in the high aspect ratio channel. However, the particles moved towards the centerline of the channel when the fluid elasticity was dominant over the fluid inertia ($El > 3.79$), thus leading to the single-line particle focusing. The multiple-line particle focusing was generated even at a low fluid elasticity ($1.483 < El < 3.79$). The multiple-line particle focusing can be facilitated by the inlet geometry, *e.g.*, the number of channel inlets owing to two reasons. First, the particles introduced through the channel with multiple inlets follow their streamlines and be entrained in the streamlines in a converging region of the straight channel, generating the multiple-line particle focusing along the straight channel. Second, the particles close to the wall at each inlet are sparse due to the wall repulsion force, which helps the rapid formation of the multiple-line particle focusing rather than in the case when introducing the particles in a single inlet channel. We expect this work will provide meaningful insights to understand particle focusing behaviors under viscoelastic flows. We also envision that this fundamental study will help design microfluidic platforms for the enrichment and separation of micro and nanoparticles encountered in a variety of applications of biology, chemistry, and nanotechnology.

2.6. References

1. Nam, J. *et al.* High-throughput malaria parasite separation using a viscoelastic fluid for ultrasensitive PCR detection. *Lab Chip* **16,** 2086–2092 (2016).
2. Cao, C., Zhou, D., Chen, T., Streets, A. M. & Huang, Y. Label-Free Digital Quantification of Lipid Droplets in Single Cells by Stimulated Raman Microscopy on a Microfluidic Platform. *Anal. Chem.* **88,** 4931–4939 (2016).
3. Paschew, G. *et al.* Autonomous Chemical Oscillator Circuit Based on Bidirectional Chemical-Microfluidic Coupling. *Adv. Mater. Technol.* **1,** 1600005 (2016).
4. Shaw, M. T. & MacKnight, W. J. *Introduction to Polymer Viscoelasticity: Third Edition*. *Introduction to Polymer Viscoelasticity: Third Edition* (2005). doi:10.1002/0471741833
5. Barnes, H. A. An introduction to Rheology. *Elsevier* (1989).
6. D'Avino, G. *et al.* Single line particle focusing induced by viscoelasticity of the suspending liquid: theory, experiments and simulations to design a micropipe flow-focuser. *Lab Chip* **12,** 1638 (2012).
7. Del Giudice, F., D'Avino, G., Greco, F., Netti, P. a. & Maffettone, P. L. Effect of fluid rheology on particle migration in a square-shaped microchannel. *Microfluid. Nanofluidics* **19,** 95–104 (2015).
8. HUANG, P. Y., FENG, J., HU, H. H. & JOSEPH, D. D. Direct simulation of the motion of solid particles in Couette and Poiseuille flows of viscoelastic fluids. *J. Fluid Mech.* **343,** S0022112097005764 (1997).
9. Kang, A. R. *et al.* Medium viscoelastic effect on particle segregation in concentrated suspensions under rectangular microchannel flows. *Korea Aust. Rheol. J.* **23,** 247–254 (2011).
10. Kim, B. & Kim, J. M. Elasto-inertial particle focusing under the viscoelastic flow of DNA solution in a square channel. *Biomicrofluidics* **10,** (2016).
11. Young Kim, J., Won Ahn, S., Sik Lee, S. & Min Kim, J. Lateral migration and focusing of colloidal particles and DNA molecules under viscoelastic flow. *Lab Chip* **12,** 2807 (2012).
12. Lee, D. J., Brenner, H., Youn, J. R. & Song, Y. S. Multiplex particle focusing via

hydrodynamic force in viscoelastic fluids. *Sci. Rep.* **3,** 3258 (2013).

13. Leshansky, A. M., Bransky, A., Korin, N. & Dinnar, U. Tunable nonlinear viscoelastic 'focusing' in a microfluidic device. *Phys. Rev. Lett.* **98,** (2007).
14. Lim, E. J. *et al.* Inertio-elastic focusing of bioparticles in microchannels at high throughput. *Nat. Commun.* **5,** 4120 (2014).
15. Lim, H., Nam, J. & Shin, S. Lateral migration of particles suspended in viscoelastic fluids in a microchannel flow. *Microfluid. Nanofluidics* **17,** 683–692 (2014).
16. Nam, J. *et al.* Hybrid capillary-inserted microfluidic device for sheathless particle focusing and separation in viscoelastic flow. *Biomicrofluidics* **9,** 64117 (2015).
17. Seo, K. W., Kang, Y. J. & Lee, S. J. Lateral migration and focusing of microspheres in a microchannel flow of viscoelastic fluids. *Phys. Fluids* **26,** (2014).
18. Yang, S., Kim, J. Y., Lee, S. J., Lee, S. S. & Kim, J. M. Sheathless elasto-inertial particle focusing and continuous separation in a straight rectangular microchannel. *Lab Chip* **11,** 266–273 (2011).
19. Yuan, D. *et al.* Dean-flow-coupled elasto-inertial three-dimensional particle focusing under viscoelastic flow in a straight channel with asymmetrical expansion-contraction cavity arrays. *Biomicrofluidics* **9,** (2015).
20. Segré, G. & Silberberg, A. Radial particle displacements in poiseuille flow of suspensions. *Nature* **189,** 209–210 (1961).
21. Ha, B., Park, J., Destgeer, G., Jung, J. H. & Sung, H. J. Transfer of Microparticles across Laminar Streams from Non-Newtonian to Newtonian Fluid. *Anal. Chem.* **88,** 4205–4210 (2016).
22. Amini, H., Sollier, E., Weaver, W. M. & Di Carlo, D. Intrinsic particle-induced lateral transport in microchannels. *Proc. Natl. Acad. Sci.* **109,** 11593–11598 (2012).
23. Bhagat, A. A. S., Kuntaegowdanahalli, S. S. & Papautsky, I. Enhanced particle filtration in straight microchannels using shear-modulated inertial migration. in *Physics of Fluids* **20,** (2008).
24. Bhagat, A. A. S., Kuntaegowdanahalli, S. S. & Papautsky, I. Inertial microfluidics for continuous particle filtration and extraction. *Microfluid. Nanofluidics* **7,** 217–226 (2009).
25. Chun, B. & Ladd, A. J. C. Inertial migration of neutrally buoyant particles in a square duct: An investigation of multiple equilibrium positions. *Phys. Fluids* **18,**

(2006).

26. Chung, A. J., Gossett, D. R. & Di Carlo, D. Three dimensional, sheathless, and high-throughput microparticle inertial focusing through geometry-induced secondary flows. *Small* **9,** 685–690 (2013).
27. Di Carlo, D. Inertial microfluidics. *Lab Chip* **9,** 3038 (2009).
28. Jain, A. & Posner, J. D. Particle dispersion and separation resolution of pinched flow fractionation. *Anal. Chem.* **80,** 1641–1648 (2008).
29. Park, J.-S., Song, S.-H. & Jung, H.-I. Continuous focusing of microparticles using inertial lift force and vorticity via multi-orifice microfluidic channels. *Lab Chip* **9,** 939–948 (2009).
30. Xiang, N. *et al.* Inertia-induced focusing dynamics of microparticles throughout a curved microfluidic channel. *Microfluid. Nanofluidics* **18,** 29–39 (2014).
31. Yamada, M., Nakashima, M. & Seki, M. Pinched flow fractionation: Continuous size separation of particles utilizing a laminar flow profile in a pinched microchannel. *Anal. Chem.* **76,** 5465–5471 (2004).
32. Zhang, J., Li, M., Li, W. H. & Alici, G. Inertial focusing in a straight channel with asymmetrical expansion-contraction cavity arrays using two secondary flows. *J. Micromechanics Microengineering* **23,** (2013).
33. Zhou, J. & Papautsky, I. Fundamentals of inertial focusing in microchannels. *Lab Chip* **13,** 1121 (2013).
34. Seo, K. W., Byeon, H. J., Huh, H. K. & Lee, S. J. Particle migration and single-line particle focusing in microscale pipe flow of viscoelastic fluids. *RSC Adv.* **4,** 3512–3520 (2014).
35. Malhotra, S. & Sharma, M. M. Settling of spherical particles in unbounded and confined surfactant-based shear thinning viscoelastic fluids: An experimental study. *Chem. Eng. Sci.* **84,** 646–655 (2012).
36. Song, H. Y., Lee, S. H., Salehiyan, R. & Hyun, K. Relationship between particle focusing and dimensionless numbers in elasto-inertial focusing. *Rheol. Acta* **55,** 889–900 (2016).
37. Li, G., McKinley, G. H. & Ardekani, A. M. Dynamics of particle migration in channel flow of viscoelastic fluids. *J. Fluid Mech.* **785,** 486–505 (2015).
38. Li, D., Lu, X. & Xuan, X. Viscoelastic Separation of Particles by Size in Straight

Rectangular Microchannels: A Parametric Study for a Refined Understanding. *Anal. Chem.* acs.analchem.6b03501 (2016). doi:10.1021/acs.analchem.6b03501

39. Sundararajan, N., Pio, M. S., Lee, L. P. & Berlin, A. A. Three-dimensional hydrodynamic focusing in polydimethylsiloxane (PDMS) microchannels. *J. Microelectromechanical Syst.* **13,** 559–567 (2004).
40. Zhou, J., Giridhar, P. V., Kasper, S. & Papautsky, I. Modulation of rotation-induced lift force for cell filtration in a low aspect ratio microchannel. *Biomicrofluidics* **8,** 44112 (2014).
41. Lu, X., Zhu, L., Hua, R. mao & Xuan, X. Continuous sheath-free separation of particles by shape in viscoelastic fluids. *Appl. Phys. Lett.* **107,** (2015).
42. Liu, C., Xue, C. & Hu, G. Sheathless Separation of Particles and Cells by Viscoelastic Effects in Straight Rectangular Microchannels. *Procedia Eng.* **126,** 721–724 (2015).
43. Romeo, G., D'Avino, G., Greco, F., Netti, P. a & Maffettone, P. L. Viscoelastic flow-focusing in microchannels: scaling properties of the particle radial distributions. *Lab Chip* **13,** 2802 (2013).
44. Del Giudice, F. *et al.* Particle alignment in a viscoelastic liquid flowing in a square-shaped microchannel. *Lab Chip* **13,** 4263–71 (2013).
45. DC, Montgomery & GC, R. Applied statistics and probability for engineers. *John wiley Sons* (2010).
46. Del Giudice, F. *et al.* Relaxation time of polyelectrolyte solutions: When μ -rheometry steps in charge. *J. Rheol. (N. Y. N. Y).* **61,** 13–21 (2017).
47. Muthukumar, M. & Freed, K. F. Theory of Concentration Dependence of Polymer Relaxation Times in Dilute Solutions. *Macromolecules* **11,** 843–852 (1978).
48. Liu, Y., Jun, Y. & Steinberg, V. Concentration dependence of the longest relaxation times of dilute and semi-dilute polymer solutions. *J. Rheol. (N. Y. N. Y).* **53,** 1069–1085 (2009).
49. Devanand, K. & Selser, J. C. Asymptotic Behavior and Long-Range Interactions in Aqueous Solutions of Poly(ethylene oxide). *Macromolecules* **24,** 5943–5947 (1991).
50. Dasgupta, B. R., Tee, S. Y., Crocker, J. C. & Frisken, B. J. Microrheology of polyethylene oxide using diffusing wave spectroscopy and single scattering. *Phys. Rev. E* (2002). doi:10.1103/PhysRevE.65.051505

51. Mach, A. J. & di Carlo, D. Continuous scalable blood filtration device using inertial microfluidics. *Biotechnol. Bioeng.* **107,** 302–311 (2010).

52. Di Carlo, D., Irimia, D., Tompkins, R. G. & Toner, M. Continuous inertial focusing, ordering, and separation of particles in microchannels. *Proc. Natl. Acad. Sci.* **104,** 18892–18897 (2007).

53. H. Ranchon, R. Malbec, V. Picot, A. Boutonnet, P.Terrapanich, P. Joseph, T. Leïchlé, A. B. 2016 DNA separation and enrichment using electro-hydrodynamic bidirectional flows in viscoelastic liquids. *Lab Chip* 25 (2016). doi:10.1039/C5LC01465D

54. Kang, K., Lee, S. S., Hyun, K., Lee, S. J. & Kim, J. M. DNA-based highly tunable particle focuser. *Nat. Commun.* **4,** 2567 (2013).

55. Gulati, S., Muller, S. J. & Liepmann, D. Flow of DNA solutions in a microfluidic gradual contraction. *Biomicrofluidics* **9,** (2015).

Chapter III.

Particle logic based on multiple focusing

3.1. Introduction

Recent advances in microfluidics are standing out technological challenges in a wide range of applications such as biological, medical, sensor and optical areas. In particular, microfluidic devices which are able to handle extremely small volume of fluid in the range of micro-liters to pico-liters are used in biological and analytical chemical applications due to the precise manipulation of fluid and particles in a microscopic environment. Moreover, many attempts have been made to embed various engineering technologies into the microfluidic platforms. On the other hand, digital electronics, which deal with discrete bands of analog levels, have attracted a great deal of attention especially in computer architecture due to their advantages over analog electronics, such as exact representation of signal and easy storage of information. Digital electronic circuits are generally constructed with logic gates based on the Boolean logic functions. Nowadays, they are implemented with help of various material systems, *e.g.*, quantum dot logic,[1,2] synthesis logic,[3,4] textile logic,[5] genetic logic,[6–9] and so on. [10–17]

Integration of microfluidics with electronics makes it possible to develop a new platform with functions of logic operation, fluidic transistors/diodes, circuit, and memory devices.[18–23] Especially, the binary logic operation is capable of performing simple calculations such as addition, multiplication and subtraction, which is the basis of the arithmetic unit in electronics. Integration of logic to other studies has been tried for the detection application or the explanation of peculiar property. Logic operation in electronics is expressed with binary number (or Boolean operation), 0 and 1, given as input and output value. For examples, AND operation is defined as multiplication of input A and B, which is described in **Figure 3.1 (a)** with a logic gate and a truth table. If input A and input B is added, the gate is defined as OR gate (**Figure 3.1 (b)**). Also, there is NOT gate indicating the opposite binary value of input value (**Figure 3.1 (c)**). These three logic gates are the

basic logic gate for adopting all logical calculation of inputs (*e.g.*, NOR, NAND, XOR…*etc*.).

For the logic operation in electronics, the control variable is only voltage in order to assign the binary number of input and output. Likewise, the control variable should be only one when the logical concept is integrated with microfluidics. For examples, existence of droplets/particles in a channel or on/off of an external force can be set as a control variable under the fixed flow conditions. Microfluidic computation has been fulfilled using an electrowetting-on-dielectric (EWOD) fluid control system or electorheological fluids with an external feedback.[24,25] Elastomeric pneumatic valves and switches employed for the microfluidic computation allows one to control fluid precisely, but generally accompanies complicated external systems as well.[20,26–30] On the other hand, droplet-based microfluidic devices have implemented the operation of basic logics, flip-flop memory, and cascadability with use of the hydraulic resistance relying upon the microfluidic droplet dynamics.[18,19,31–33] However, it is not easy to precisely control the position and trace of microparticles such as PS particle and blood cells in the microfluidic channel due to the negligible interaction between particles. Here, we devise a microfluidic inertia-elastic particle focusing system able to perform manifold logic operations with high accuracy. Existence of particles is selected as only variable and the other conditions (*e.g.*, particle size, flow rate and fluid elasticity) are fixed for a designed microchannel. While particle focusing has been vaguely explained as a method of particle manipulation in a continuous flow, the integration of particle focusing for logic devices designs the particle control more systematically for a facile sample treatment. By considering geometry of the microchannel, the logical outputs are determined and the result can be predicted theoretically according to the design of a device.

Passive particle manipulation has been widely investigated using viscoelastic properties of polymeric solutions. The combination of elastic and inertial forces results in the particle migration toward the equilibrium location based on the gradient of the normal stress difference developed in non-Newtonian flow.[34–45] In addition, nonlinearity of viscoelastic fluid has been applied to a microfluidic memory device with electronic functions.[21,46]

A new microfluidic logic device is introduced in this study based on particle dynamics in viscoelastic flow using hydrodynamic forces, intrinsic properties of fluids, and channel

confinement.[35,36,47] A binary number “0” or “1” is assigned at the input/output channels depending on the existence of particles, and then basic logics including XOR, AND, OR, Buffer, and NOT are implemented by using a combination of the binary numbers in the input/output channels. **Figure 3.2** shows a schematic illustration of the microfluidic logic device.

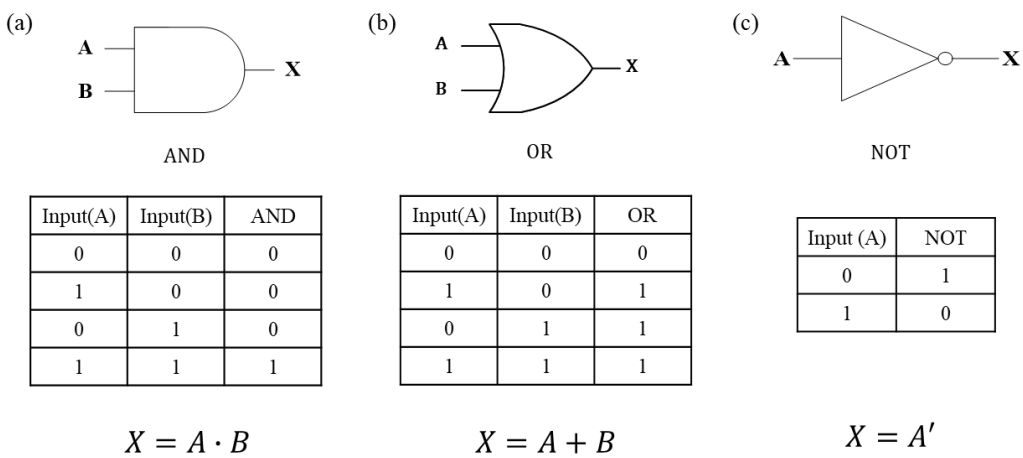

Input(A)	Input(B)	AND
0	0	0
1	0	0
0	1	0
1	1	1

$X = A \cdot B$

Input(A)	Input(B)	OR
0	0	0
1	0	1
0	1	1
1	1	1

$X = A + B$

Input (A)	NOT
0	1
1	0

$X = A'$

Figure 3.1. Basic logic gate for logic operation. (a) AND gate and truth table, (b) OR gate and truth table, (c) NOT gate and truth table.

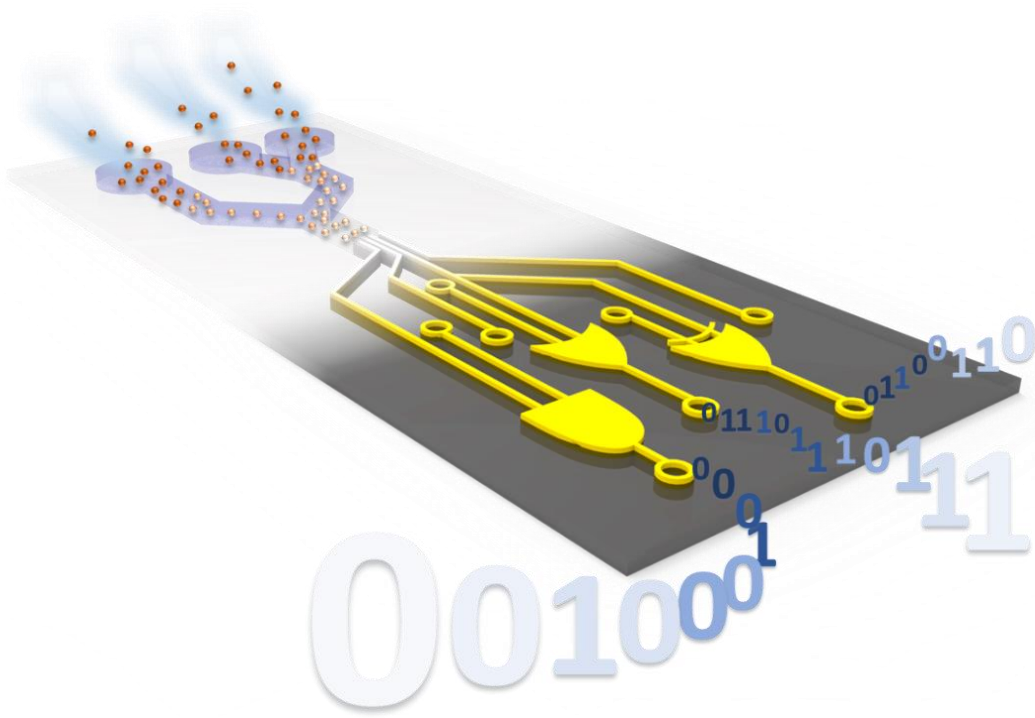

Figure 3.2. A schematic illustration of a microfluidic logic device.

3.2. Experimental

3.2.1. Design and fabrication of a microchannel

The microchannel is fabricated using a standard soft lithography method with Polydimethylsiloxane (PDMS) (Sylgard 184, Dow Corning) which was explained with **Figure 1.1** in Chapter I. A replica mold is prepared on a silicon wafer with negative photoresist (SU-8, Microchem Corp.) The PDMS solution composed of base and curing agents (10:1) is poured onto the SU-8 master. The mold is degassed in a vacuum chamber for 1 hour and cured in an oven at 65 ℃ for 6 hours. The PDMS channels are peeled off and punched using a puncher with a 1.5 mm diameter (Uni-Core, Harris) for tube connections. The channels are bonded onto a glass slide by using a plasma cleaner and heated at 120 ℃ for 1 hour to enhance the bonding strength.

The microfluidic device is designed to manipulate the particle focusing location in the channel (**Figure 3.3**), hydrodynamically. The cross-sectional aspect ratio (AR=*W*:*H*) of the microfluidic channel is 4:1, and 3 inlets are assigned as inputs A, B, and a supporting input, EN. The width of the channels for inputs A and B is 100 μm, and the width of the channel for the supporting input EN is 50 μm such as **Figure 3.3 (a)**. The channel length for the particle focusing is calculated by a single dimensionless parameter, $\Theta = Wi(L/W)(a/W)^2$, where Wi $(= \lambda\dot{\gamma} = 2\lambda Q/HW^2)$ is the Weissenberg number, λ is the relaxation time, Q is the flow rate, W is the channel width, H is the channel height, and L is the focusing length. When the viscoelastic fluid flows with a flow rate of 0.1 ml/hr, Wi is 4.4035 and Θ is 1.[34,35] This satisfies a condition necessary for the viscoelastic particle focusing. As a result, the calculated particle focusing length is approximately 6 mm. Since the length of the input channel is 25 mm, it is long enough to stabilize the position of particles. The supporting input EN, acts as a modulator for the logic operation. The inlet flows are converged, forming multiple particle focusing lines in the straight channel with a width of 100 μm and a length of 10 mm. The straight channel is referred to as a merging channel in this paper. The merging channel is connected to the expansion chamber (W= 3100 μm, H= 25 μm, and L= 1 cm). The entire geometry and dimension of the microfluidic channels are determined based on the numerical simulation. In particular, the width and

connection locations of the single inlet and the four outlets in the expansion chamber are tested and determined numerically. More details of the device are illustrated in **Figure 3.3 (b)**.

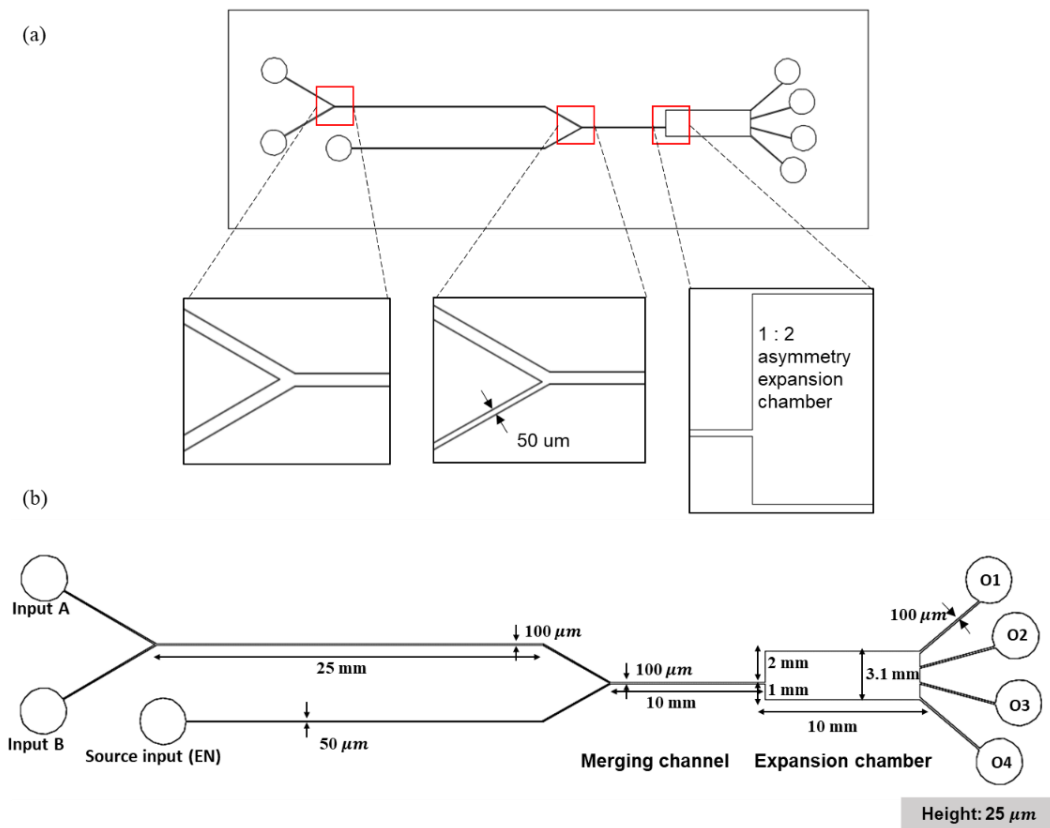

Figure 3.3. Design of a microchannel for logic operation. (a) Expanded images of microchannel segments (b) Detailed scale of a microchannel.

3.2.2. Sample preparation

Aqueous solution of 1500 ppm Polyethylene oxide (PEO, Mw= 2,000,000, Sigma-Aldrich) is prepared for the medium. Deionized (DI) water and glycerol are mixed at a ratio of 22 wt%. PEO powder is then added to the 22 wt% glycerol aqueous solution. Finally, 6.42 μm fluorescent polystyrene (PS) particles (1% w/v, Nile red, FP-6056-2, Spherotech Inc.) are suspended into the PEO solution with a small amount of TWEEN 20 (P1379-25ML, Sigma-Aldrich) to prevent aggregation of the particles.

We demonstrated multiple line focusing criteria with respect to *Re* and *Wi* in previous study and the multiple lines are stably formed when $1.483<El<3.79$ based on the criteria.[36] If *El* of the fluid is higher than 1.483, the location of the focusing lines are close to each other near the channel center and it affects the outputs. Therefore, a microfluidic logic device has to be designed according to the fluid elasticity. The distance between the focusing lines is manipulated by the flow rate control with fixed fluid elasticity. As the flow rate decreases, the multiple lines become closer to each other in the merging channel. The slight difference of the focusing locations affects to the particle path at the downstream. Since the multiple lines have to be well-separated when they pass through the expansion chamber, 0.1 ml/hr of the flow rate is properly selected for the best performance.

Concentration of the fluorescent particles is fixed as around 0.017 vol% which allows enough fluorescence intensity to observe the particle migration. The microchannel is flushed with a viscoelastic medium to prevent the adhesion of particles onto the channel wall and air bubble generation. The solution is injected into the microchannel using a syringe pump (KDS 200, KD Scientific) with a flow rate (Q) of 0.1 ml/hr. An inverted optical microscope (IX 53, Olympus) and a charge-coupled device (CCD) camera (AcquCAM 23G, VISIONHI) are used to observe the particle flow. The lateral positions of the particles are measured by image-processing with Image J and an Image-Pro software.

3.2.3. Rheological properties of the solution

The rheological properties of a viscoelastic solution are measured by using a rotational (MCR-301, Anton Paar) and a Capillary Breakup Extensional Rheometer (CaBER-1, ThermoHakke). The steady shear viscosity ($\eta = 15.8$ mPa $\cdot$ s) and the relaxation time ($\lambda = 19.8$ ms) are determined by the experiments. A diluted polyethylene oxide (PEO) solution is chosen for the viscoelastic medium since the solution shows proper viscous and elastic properties. For the viscoelastic fluid, the elasticity number (El) is defined as $El = Wi/Re$, which is the ratio of the Weissenberg number ($Wi = \lambda\dot{\gamma} = 2\lambda Q/HW^2$) and the Reynolds number ($Re = \rho U D_h/\eta$). Here, $\dot{\gamma} = 2U/W = 2Q/HW^2$ is the characteristic shear rate, and $D_h = 2WH/(W + H)$ is the hydraulic diameter of the rectangular channel. Since this dimensionless number includes the channel geometry information, it varies across the microfluidic logic device.

3.3. Numerical analysis

Numerical simulation is carried out to analyze the effect of channel aspect ratios on the first normal stress difference by using the commercial program COMSOL Multiphysics based on Finite element method (FEM). For the simulation, the steady-state momentum equation is expressed as

$$\rho\left(\frac{\partial \boldsymbol{u}}{\partial t} + (\boldsymbol{u}\cdot\nabla)\boldsymbol{u}\right) = \nabla\cdot(-p\boldsymbol{I} + \eta_s(\nabla\mathbf{u} + (\nabla\boldsymbol{u})^T) + \boldsymbol{T}) \tag{3-1}$$

and the extra stress contribution is given by

$$\boldsymbol{T} + \lambda\left(\frac{\partial \boldsymbol{T}}{\partial t} + (u\cdot\nabla)\boldsymbol{T} - [(\nabla\boldsymbol{u})\cdot\boldsymbol{T} + \boldsymbol{T}\cdot(\nabla\boldsymbol{u})^T]\right) = 2\eta_p(\nabla\boldsymbol{u} + (\nabla\boldsymbol{u})^T) \tag{3-2}$$

, where $\boldsymbol{u}$ is the velocity vector, λ is the characteristic relaxation time, η_p and η_s are the viscosities of polymer and solvent, respectively, and the total viscosity (η) is $\eta_p + \eta_s$. These two equations are solved together with the continuity equation to confirm the effect of the N_1 distribution.

3.4. Results and Discussion

3.4.1. Mechanism of microfluidic logic operation

The Boolean operators in the microfluidic logic device are implemented according to the presence and absence of particle suspension flow in a channel. For example, if a particle travels through input/output channels, the logical value "1" is assigned to the channel. Otherwise, the channel has the logical value "0". In order to manipulate the particle focusing locations, the inlet assigned as "1" is only under continuous flow. When an inlet has the logical value of "0", it means that particle suspension is not injected into the inlet. And it can be interpreted that only the medium flows through the output channel without particles. The focusing location of particles in the upstream channel is of great importance since the existence and absence of the particles in the downstream channels is determined by the location. Furthermore, multiple-line particle focusing in the channel is needed for operating multiple logic gates simultaneously. Basically, the viscoelastic complex fluids enable the generation of the multiple-line particle focusing in the microfluidic channel with a high aspect ratio.[36] In the current study, the PEO solution is employed for the particle focusing. The elastic force acting on the particle ($F_E \sim a^3 \nabla N_1$) in the complex fluid is estimated using the first normal stress difference ($N_1 = \tau_{xx} - \tau_{yy}$) of the fluid, where a is the particle diameter, τ_{xx} is the normal stress in flow direction and τ_{yy} is the normal stress in velocity gradient direction in our coordinate system. The particles are likely to migrate laterally towards the channel center with the minimal value of N_1 due to the imbalance between the elastic force and the inertial force.[42,43] In a high aspect ratio microchannel, the focusing location can be controlled more actively by using the shear-gradient lift force ($F_{L.S}$) depending on the channel configuration and confinement, such as the inlet number and injection location.[36] High channel aspect ratio leads to broad plateau region of minimal N_1, so as the stable region for the particle migration become wider than that in the low aspect ratio channel. Also, the particles introduced through the channel with multiple inlets follow their streamlines and be entrained in the streamlines in a straight merging channel due to wall-repulsion force at each inlet and shear-gradient force enhanced by the multiple inlets. By the balance of the elastic and inertial forces, the multiple-line

particle focusing is generated along the channel. The microfluidic logic device consists of 4:1 aspect ratio and the 3 inlets for the multiple particle focusing lines. An expansion chamber is an additional part in order to utilize the particle streamlines for logic operations based on the focusing locations at the merging channel. For the proper operation of the logic gates, 1500 ppm PEO aqueous solution is adopted as a medium in the microfluidic device, of which the fluid elasticity ($El = Wi/Re = \lambda\eta(W + H)/\rho H W^2$) is 1.483.

3.4.2. Multiple focusing for logic operation

Figure 3.4 presents the results of multiple-line particle focusing in the merging channel. The distribution of N_1 in the channel is numerically calculated to explain the mechanism of the multiple-line focusing as shown in **Figure 3.4 (a)**. As the channel aspect ratio becomes high, N_1 distribution can generate the broad in-plane particle focusing, which facilitates the multiple-line particle focusing in the merging channel. The focusing locations are changed according to the applied input condition [AB]=[00], [10], [01], and [11]. Since particles are injected through EN constantly, a supporting single focusing line is generated in the merging channel for all the experiments. The elastic and inertial forces that particles undergo results in different particle focusing patterns in the channel according to the input condition. When A and B are equal to "0" as shown in **Figure 3.4 (b-i)**, a single focusing line of the particles supplied from EN is located at the center of the merging straight channel (**Figure 3.4 (c-i)**). When the particles are injected into the input, A or B (**Figure 3.4 (b-ii)** and **3.4 (b-iii)**), the double focusing lines are generated in the input channel and then co-exist as a single line from EN in the merging channel. If the particle suspension is injected into only one of input channels, the flow detours along the other input channel. That is why the focusing band, *i.e.*, double-line particle focusing can occur in the input channels. As well as the distribution of N_1, the position of particle focusing line is determined by the main streamlines. Once two different flows are converged, the resulting streamlines change depending on the flow rate. As a result, the particles in the converging region migrate towards the side wall close to the input channel. At the same time, the shear-gradient force due to the channel confinement pushes the particles to off-centered locations. Since the focusing line formation is also affected by wall-repulsion force entrained from the injection,

the number of focusing lines is equal to the number of inlet flows. The shear-gradient force and the wall-repulsion force are categorized as the inertial force and the competition between inertial and elastic forces in the merging channel is schematically represented in **Figure 3.4 (a)**. When both A and B represent “1” implying the particle injection (**Figure 3.4 (b-iv)**), clear triple focusing lines are generated in the merging channel as shown in **Figure 3.4 (c-iv)**. In this sense, the double focusing lines generated in the input channel are clearer and closer each other than the lines in the cases of [10] and [01] in the merging channel. The focused particles from the inlets are constrained into the merging channel and the final locations of the multiple focusing lines are determined at the merging channel before reaching the expansion chamber.

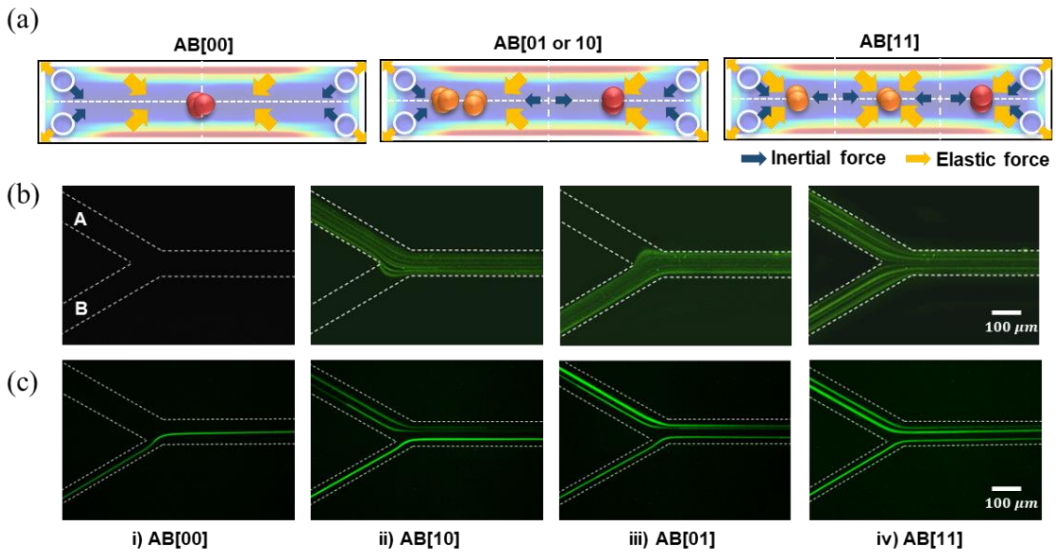

Figure 3.4. Multiple-line particle focusing developed in the merging channel. (a) Numerical simulation results of the first normal stress difference distribution in the 4:1 aspect ratio microchannel and schematic of force competition for the multiple particle focusing locations in the cross-sectional N_1 distribution. (b) Fluorescent images of particle injection in the inlets, A and B and (c) particle migration in the merging channel.

3.4.3. Particle migration at expansion chamber

The particles aligned in the merging channel go into an expansion chamber through the entrance positioned at the third location of the lateral surface of the expansion chamber. This asymmetric geometry is designed and fabricated to control the multiple particle lines in the expansion chamber more efficiently based on the simulation results of the elastic force distribution and streamlines as shown in **Figure 3.5 (a)**. The streamlines indicate the possible focusing region of the particles for each input and the calculated streamlines from the inlets of EN, A, and B are colored in red, green, and blue, respectively. Particle migration is identified by using fluorescent particles (**Figure 3.5 (b)**). The fluid elasticity allows particles to be sorted in the chamber with high resolution depending on the size, which is the so-called 'elasto-inertial pinched flow fractionation (EiPFF)'. As well as the particle sorting, the particle focusing efficiency is enhanced with increasing the elastic force. Similar to EiPFF mechanism, the multiple focusing lines are manipulated in the expansion chamber. The focusing locations of the particles are measured for each input condition by using image-processing as shown in **Figure 3.6** and the separation resolution ($R_{ij} = \frac{\Delta x_{ij}}{2(s_i+s_j)}$) between the focusing lines is evaluated for the confirmation of multiple focusing, where Δx_{ij} is the distance between the focusing lines, and the s_i and s_j is the standard deviation of the *i*-th and *j*-th focusing locations. The higher value in the **Figure 3.6 (a)** represents the better separation of the focusing lines.

Meanwhile, the merging channel length can affect the desired focusing locations for logic operation. The length of merging channel is designed as 10 mm. In fact, the effect of the merging channel length on the particle focusing is negligible since the inlet channel length is significantly large for the particle focusing. The length of the inlet channels is set as 25 mm, which is long enough to satisfy the essential condition for the particle focusing and the focusing length is calculated as 6 mm by using the relation, $\Theta = Wi(L/W)(a/W)^2$, when the viscoelastic fluid flows with a flow rate of 0.1 ml/hr, Weissenberg number (Wi) of 4.4035 and Θ of 1. The parameter Θ indicates the required value to trap all the particles within the 'inner band' when the particle suspension flows in a pipe ($\Theta \cong 1$).[40] The focused particles from the inlets are constrained into the merging channel and the final locations of the multiple focusing lines are determined at the merging

channel before reaching the expansion chamber. The focusing locations at the end of the channel might be influenced by the merging channel length. Due to the balance of the forces, the focusing locations are more stabilized compared with those at the entrance of the channel as shown in **Figure 3.7**. While the single focusing line keeps the initial location along the straight channel when AB is [00], the triple lines are slightly gathered towards the channel center by the fluid elasticity when AB is [01]. If the merging channel is too short, the focusing lines might be scattered at the expansion chamber resulting in error or low efficiency for the logic outputs.

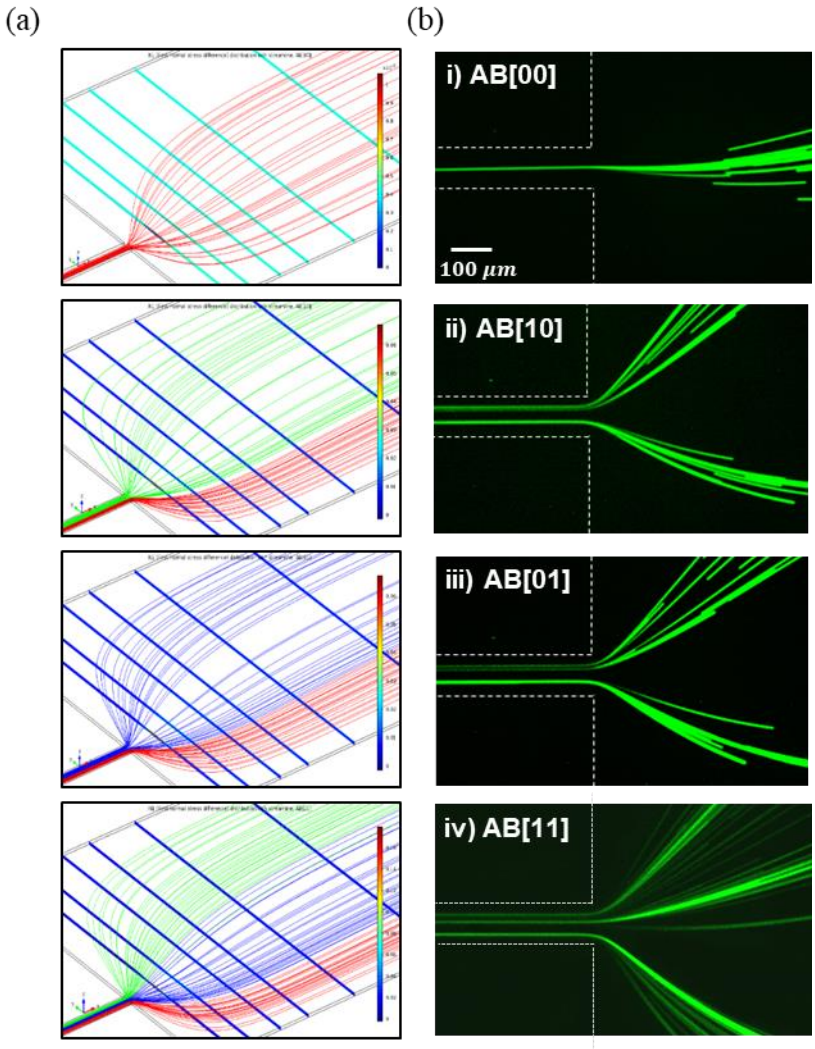

Figure 3.5. Multiple-line particle focusing developed in the expansion chamber. (a) N umerical simulation results of the first normal stress difference distribution in the exp ansion chamber using Multiphysics COMSOL and colored lines are stream lines from inlets (EN: red, Input A: green, Input B: blue). (b) Fluorescent images of particle m igration in the expansion chamber.

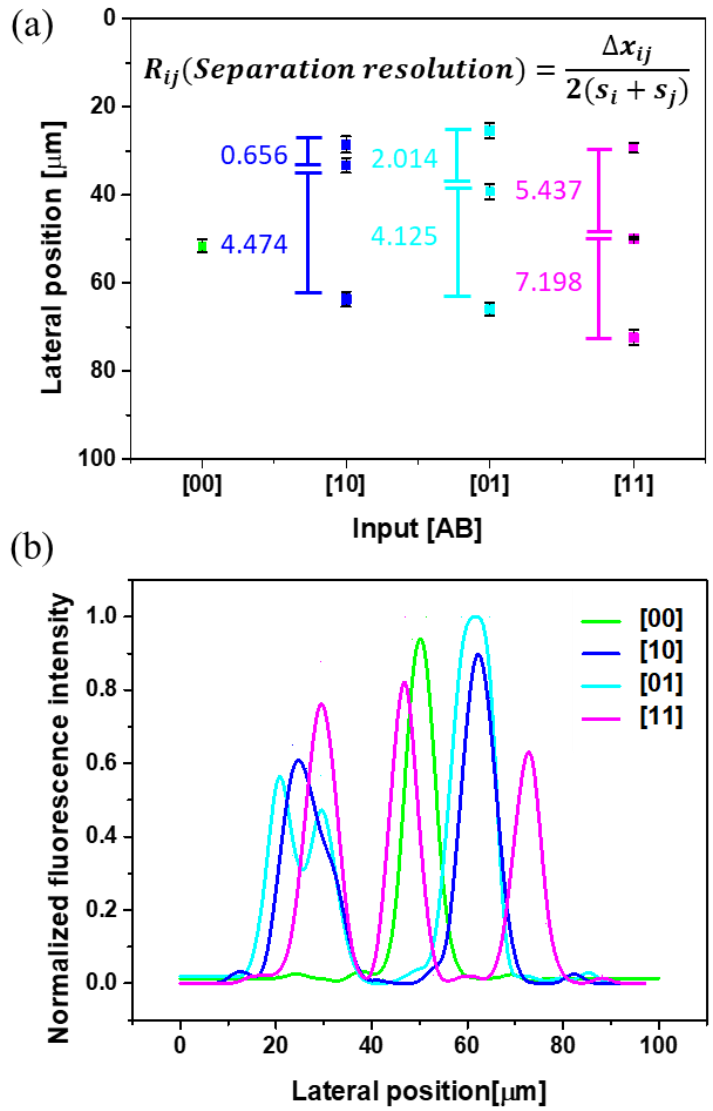

Figure 3.6. Measured focusing locations by image-processing with (a) Image-pro software and evaluated separation resolution of the multiple particle focusing lines for each input condition. (b) Fluorescence intensity of the focusing lines obtained by ImageJ.

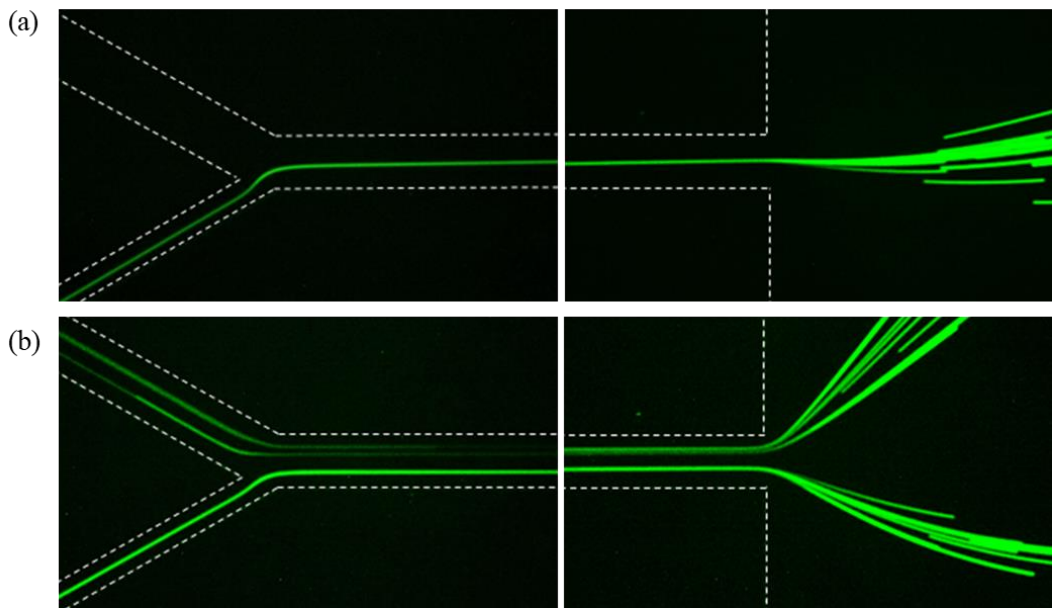

Figure 3.7. Comparison of the focusing location at the entrance and end of the merging channel. (a) When AB is [00], (b) When AB is [01].

3.4.4. XOR, OR and AND gates

The viscoelastic fluid in the chamber exits through 4 outlets, which represent specific outputs in the logic gate proposed in this study (**Figure 3.8**). The ranges of lateral positions for outlets 1, 2, 3, and 4 are 0~557 μm, 557~1550 μm, 1550 ~2543 μm, and 2544 ~ 3100 μm, respectively. The locations and dimension of the outlets are optimized numerically. **Figure 3.8** shows fluorescent particle images of the outputs obtained when inputs [00], [01], [10], and [11] are applied to the microfluidic device. Depending on the location of particle focusing lines in the channels, the particles go out through the outlets. Indeed, the focusing location generated in not only the input channel but also the merging channel plays a key role in determining the output binary number. When particle suspension is introduced into both A and B, *i.e*., [11], the triple focusing lines are slightly moved downwards due to the relatively enhanced inertial force. As a result, the outputs of outlets 2, 3, and 4 are found to be "1". On the other hand, when the input A or B is "0", *i.e*., [10] or [01], the outputs of outlets 1, 2, and 3 become "1". The outputs based on particle extraction in the outlets are evaluated using the normalized fluorescence intensity (**Figure 3.9 (a)**). Also, we carried out the uncertainty analysis for the scattered peaks of the normalized fluorescence intensity (**Figure 3.9 (b)**). Scattered peaks of the intensity are rearranged by the mean values and standard deviation within the 95 % confidence interval. The probability of the particle appearance at each output was evaluated by the fluorescence intensity since it has correspondence with the lateral positions of the particles at the end of expansion chamber. With 95% of confidence interval, we obtained the representative value of the peaks for the logic operation. For example, when [AB] is [01], the normalized fluorescence intensity is 0.63 ± 0.05 and the lateral position is $308.39\pm14.28\mu m$ at the output 1 (O1) which is within the confidence interval of $280.41\leq \mu(\mu m) \leq 336.37$. From this, logic gates are assigned to the outputs and the corresponding logic circuit is finally established as presented in **Figure 3.9 (b)**.

The three elementary logic gates, *i.e*., XOR, OR, and AND are implemented simultaneously using a single microfluidic platform (**Figure 3.10**). It is identified that the microfluidic logic gates can successfully perform logic operations, *i.e*., Boolean functions yield a single binary output according to a pair of binary inputs. The results of microfluidic logic operations are compared to electronic logic gates. Inputs A and B are controlled by

toggle switches and connected to logic gate IC chips (XOR, OR, and AND) on a breadboard. The outputs are identified with use of LED lights (**Figure 3.11**). The supporting input EN corresponds to the operating voltage. By using electronic system design tool VIVADO® (Xilinix Inc., USA), inputs and outputs are depicted as signal waves (**Figure 3.11(i)**).

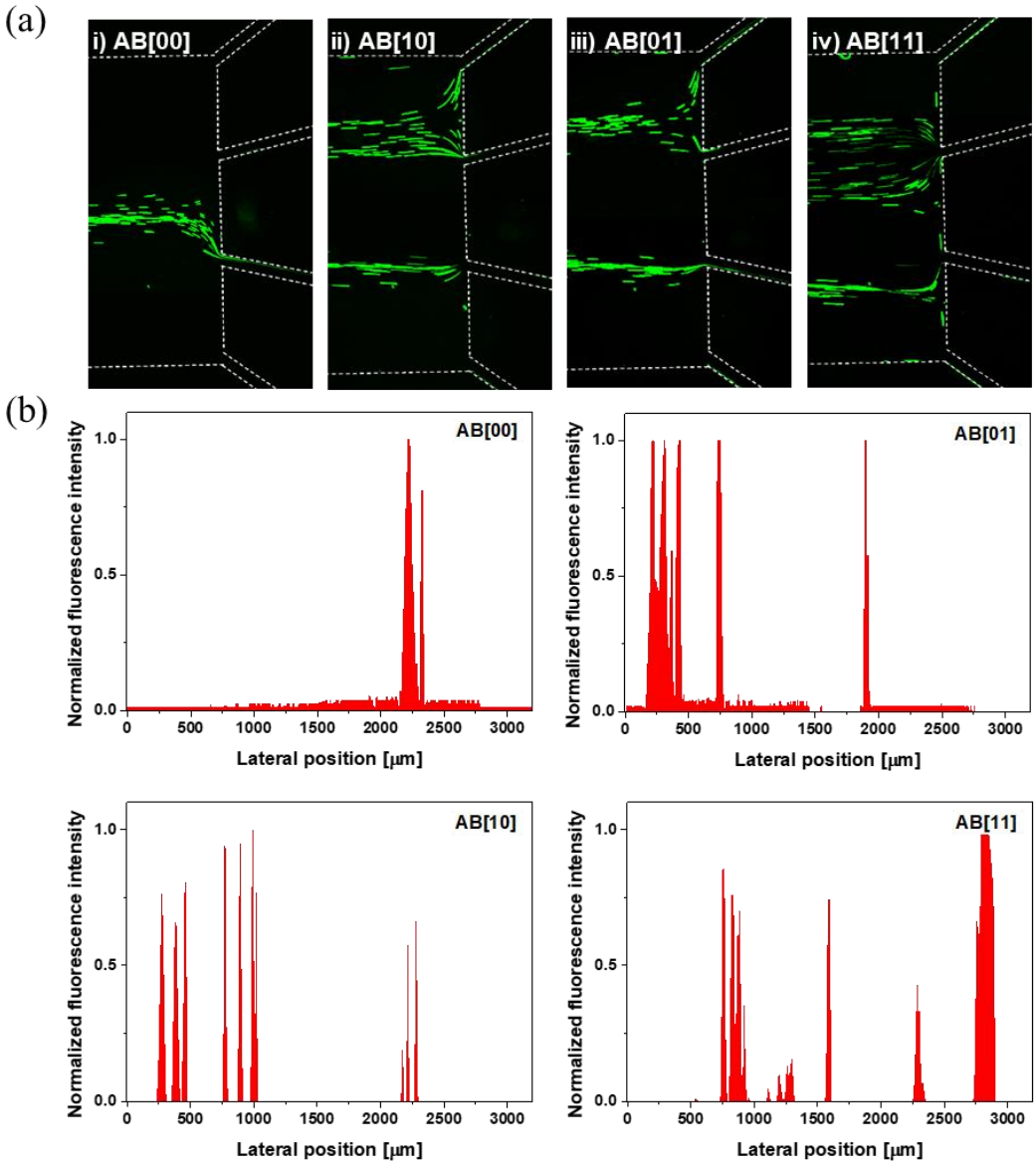

Figure 3.8. Logic operations implemented using multiple-line particle focusing. (a) Fl uorescence images of particle migration in the outlets for 4 cases: AB [00], [10], [01] and [11] and (b) measured fluorescence intensity of the particles.

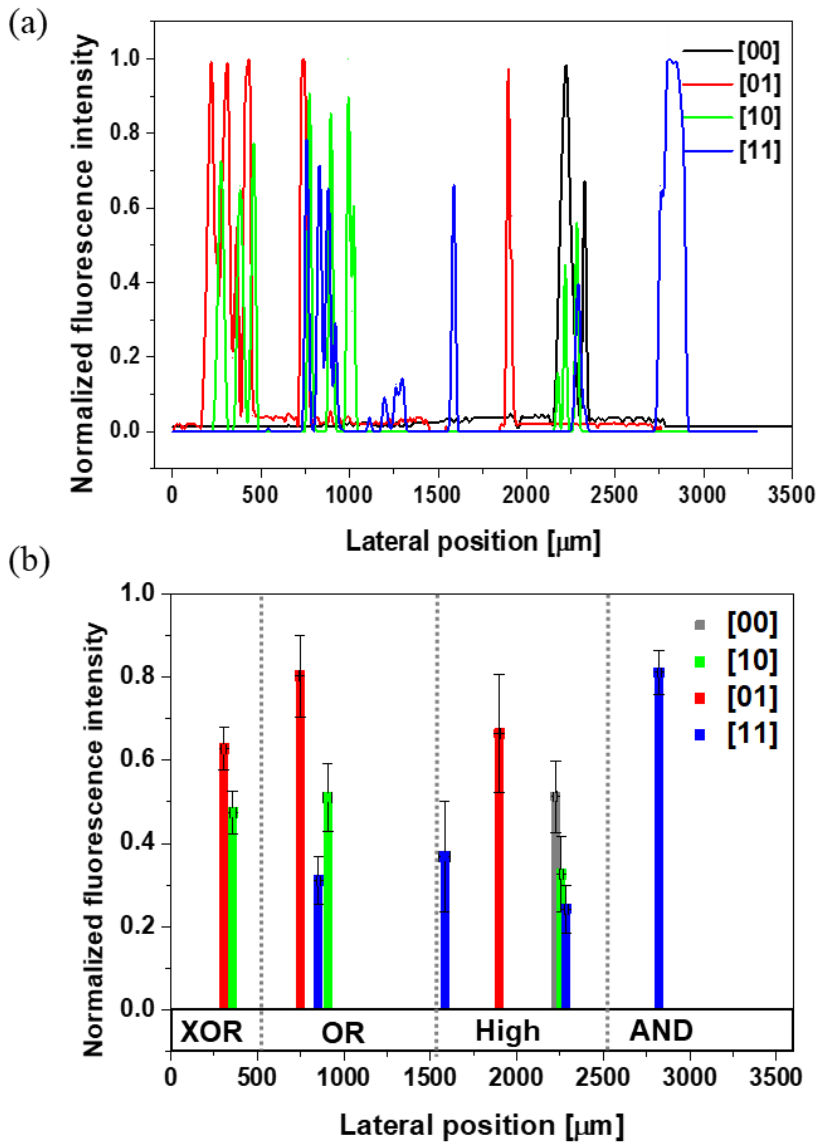

Figure 3.9. Superimposed normalized fluorescence intensity graph built to categorize outputs with particle flow. (a) Scattered intensity peaks of fluorescent particles, (b) re arranged intensity with 95 % confidence interval and corresponding logic circuit for X OR, OR and AND operations.

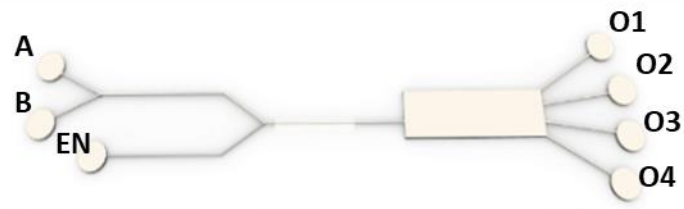

A	B	AND	OR	XOR
0	0	0	0	0
1	0	0	1	1
0	1	0	1	1
1	1	1	1	0

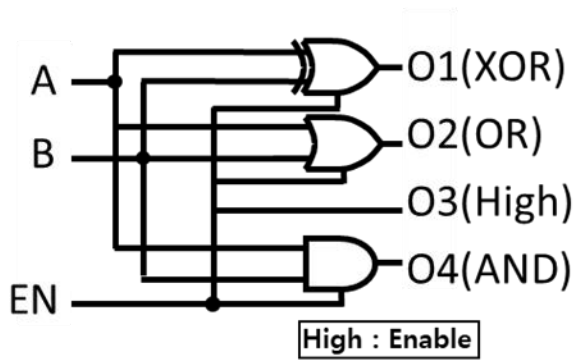

Figure 3.10. Corresponding logic gate operation to particle migration in a microchannel and a circuit and a truth table for XOR, OR and AND operations.

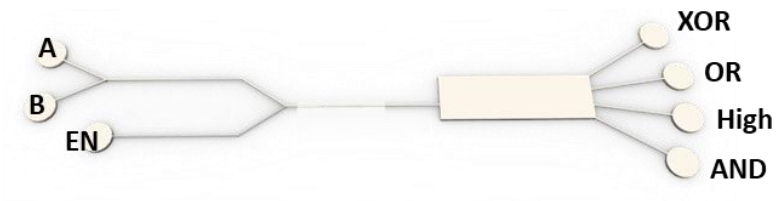

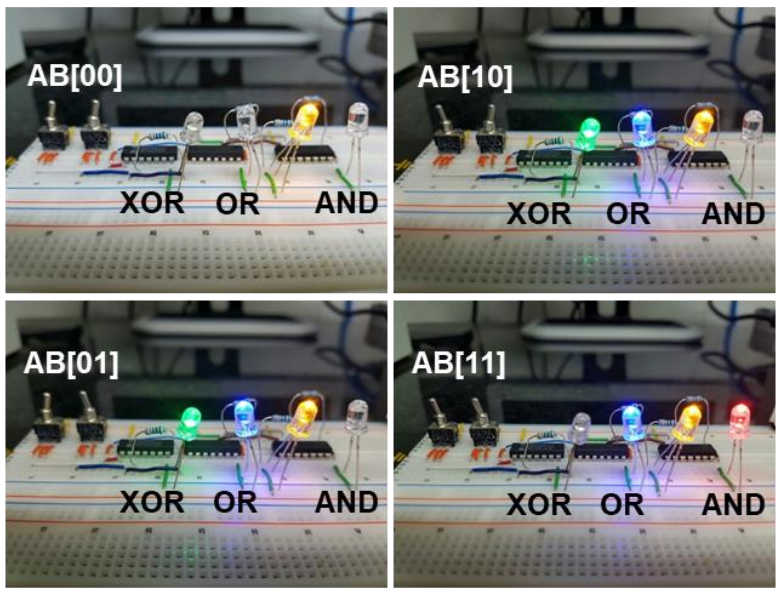

i)

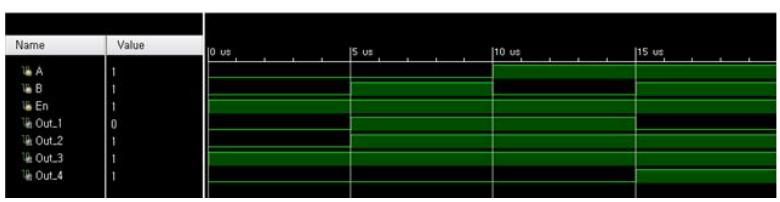

Figure 3.11. Common electronic logic circuit matched with the microfluidic logic device. By using two input logic IC chips, logic operations (XOR, OR, and AND) were compared to the outputs in a microfluidic device. (i) Inputs and Outputs can be described as signal waves by using electronic system design tool VIVADO® (Xilinx Inc., USA).

3.4.5. Particle concentration and size effect

Additional analysis on the experimental results was conducted with 0.017 wt% of the particle concentration, which was sufficient weight fraction for the clear fluorescent images. In order to confirm the particle concentration effect, we carried out an additional experiment with 0.1 wt% solution. Although there might be a difference in focusing efficiency, the microfluidic logic operation is insensitive to the particle concentration (**Figure 3.12**). We anticipate that high concentration of the particles makes the focusing line more clear and enhance throughput without change of the logic operation.

The microfluidic logic device is designed to have an expansion chamber, thus, the pinched flow obviously affects the particles. Kang *et al*. has studied elasto-inertial pinched flow fractionation (EiPFF) under DNA dilute solution flow.[38] When the particles enter the expansion chamber, the lateral migration velocity is different due to the particle size resulting in size separation. Here, we designed the microchannel for hydrodynamically generated multiple line particle focusing. The logic device in this study is specifically designed only for 6.4 μm particles (blockage ratio of about 0.25) to realize the XOR, OR, and AND gates. For the various particle sizes, the logical outputs cannot be defined as the same as that of the channel using 6.4 μm particles because of the particle size effect. The particle size effect was investigated in the previous work.[36] As the particle size increases, double focusing lines are located near the walls since the shear-gradient lift force is enlarged by proportionality of a^3 under the viscoelastic flow, where a is the particle diameter. In the microfluidic logic device, the larger particles are focused near the channel walls before reaching the merging channel, therefore, the focusing locations in the merging channel and expansion chamber are determined by their initial focusing position (**Figure 3.13 (a)**). Different from the pinched flow fractionation, the particles keep the initial streamlines along the initially injected positions. Therefore, the focusing location of the particles critically affects the outputs of logic operation. For the state of AB [11], particles of three sizes are employed to investigate the size effect on the logic function. As shown **Figure 3.13 (b)**, particles of 10 and 15 μm in diameter pass towards the outlet 1 as designed for XOR gate, although there should be no particle in the outlet 1 when AB is equal to [11]. The logic device in the manuscript is specifically designed only for 6.4 μm particles (blockage ratio of about 0.25) to realize the XOR, OR, and AND gates. Another

microfluidic logic device can be designed according to the particle sizes by expecting the multiple focusing locations.

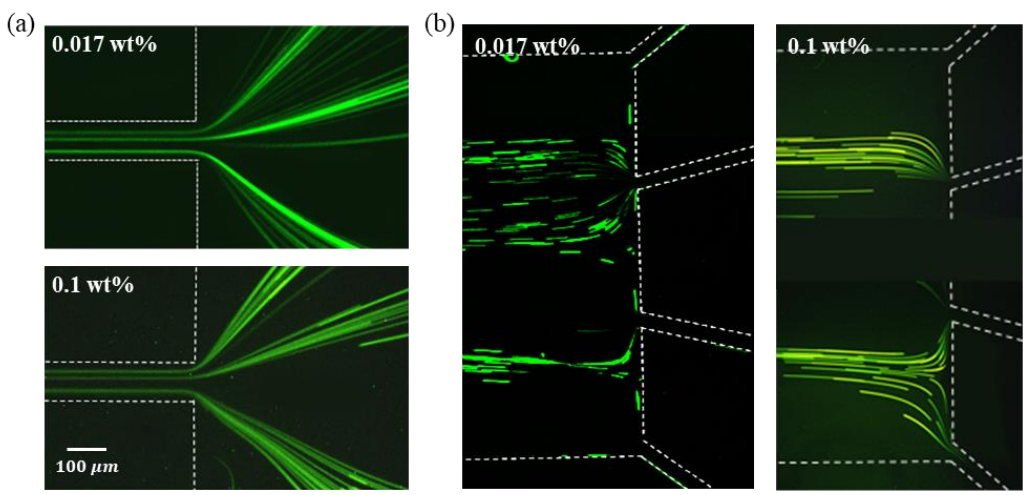

Figure 3.12. When [AB] is [11], the experimental results were compared according to the particle concentration.

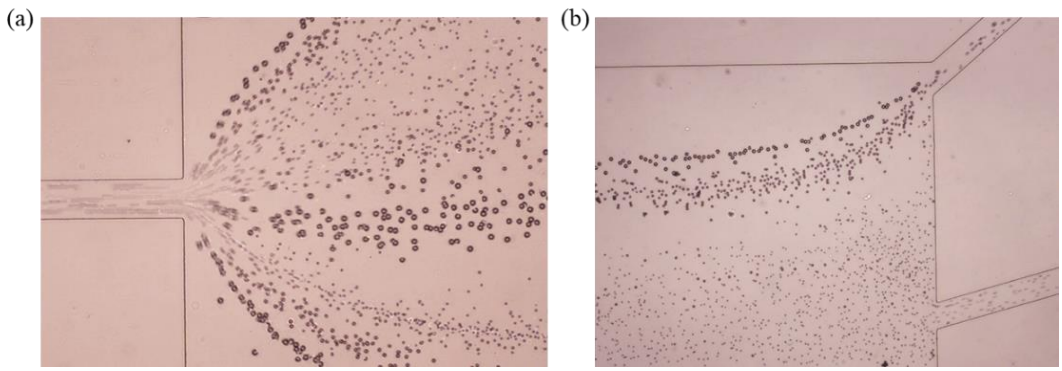

Figure 3.13. Particle size effect in a microfluidic logic device. (a) 3 sizes of particles are injected into the microfluidic logic device when AB is [11]. The particles are entering to the expansion chamber through the merging channel keeping their focusing locations. (b) The output 1 is designed as XOR gate for only 6.42 μm particles. However, the larger particles are easy to be extracted out through output 1 since the focusing locations of 10 and 15 μm particles from input A is weighed to the upper wall of the merging channel.

3.4.6. NOT and Buffer gates

In a continuous flow, it is a challenge to implement an NOT gate by using particle movement. However, the microfluidic logic device using multiple-line particle focusing shows remarkably enhanced performance and possibility. Figure 3.14 shows the NOT and Buffer operations in the device. The logic operations of the outputs are dependent only on input A, while input B is set as another supporting input, EN. When input A is "0", the particles move towards outlet 1, indicating output "1" (**Figure 3.14 (a)**). However, input "1" leads to output "0" (**Figure 3.14 (b)**). With help of the same mechanism, outlet 4 can act as a Buffer gate, which duplicates the input value. The particle locations near each output were also measured by image-processing and clear peaks were obtained by adopting 95 % confidence interval (**Figure 3.15 (b)**). The relevant logic circuit and truth table of the single input microfluidic logic gates are presented in **Figure 3.16**. The electronic logic gates are also confirmed as the results of microfluidic binary operation (**Figure 3.17**). Basic logic gates including AND, OR, XOR, Buffer and NOT are gained at each output depending on inlet flow. Furthermore, another logic gate or calculation can be designed by using different geometry of the channel. The further consideration is needed to realize the microfluidic logic calculation (*e.g.*, multiplexer, adder and *etc*.) based on viscoelastic particle focusing.

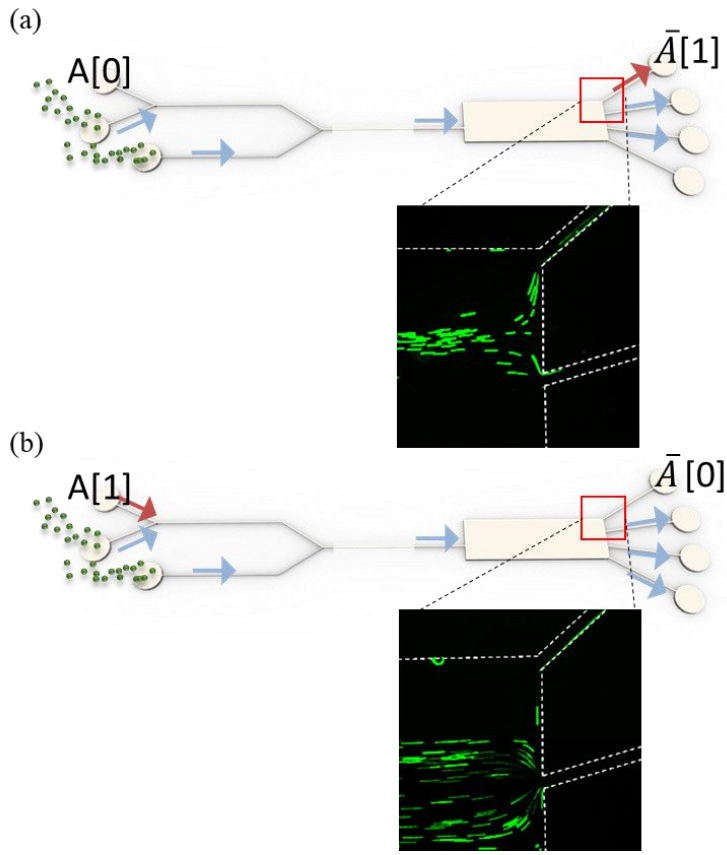

Figure 3.14. Logic operations implemented using multiple-line particle focusing. Fluor escence images of particle migration in the outlets for 2 cases: (a) A[0] and (b) A[1].

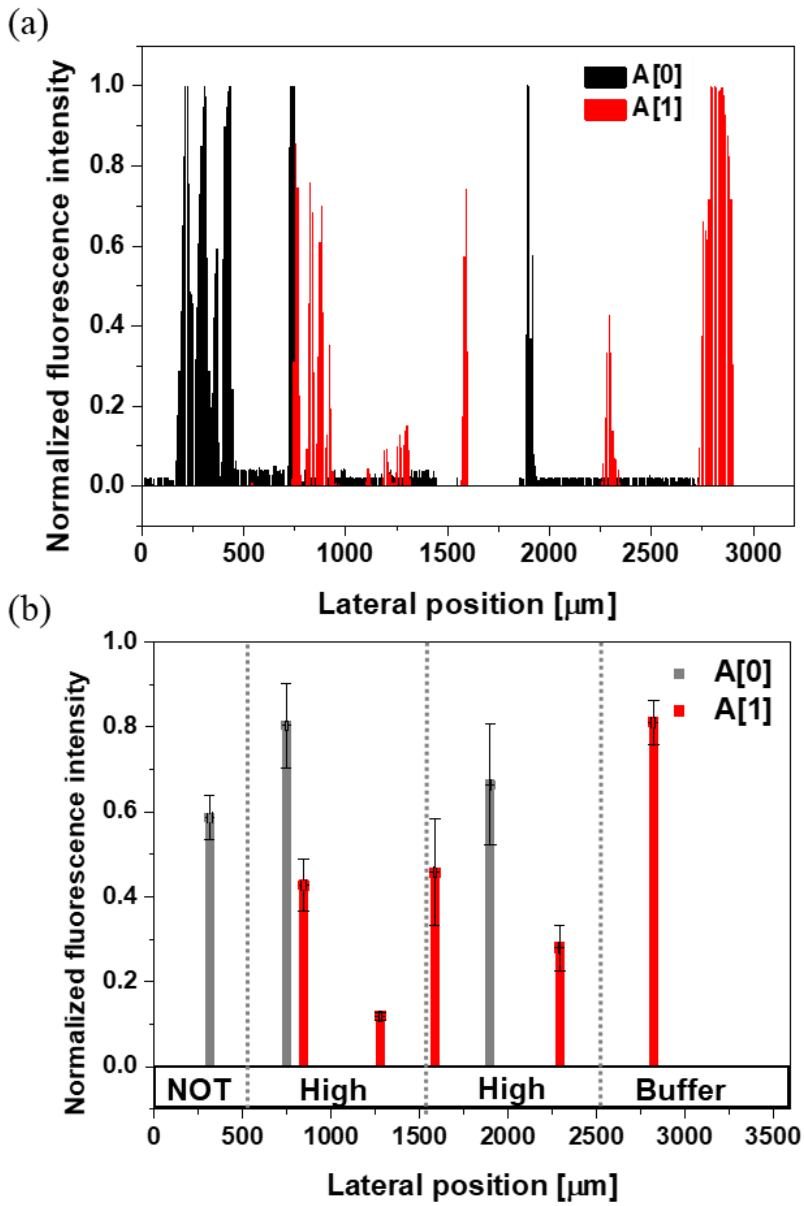

Figure 3.15. Superimposed normalized fluorescence intensity graph for NOT and Buf fer operation. (a) Scattered intensity peaks of fluorescent particles, (b) rearranged inte nsity with 95 % confidence interval and corresponding logic circuit.

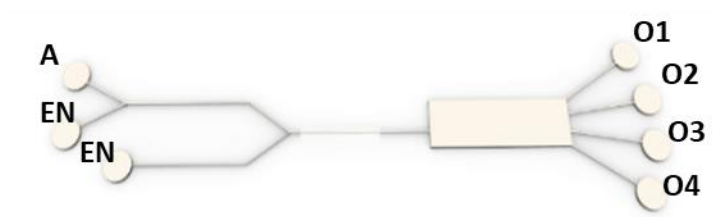

A	NOT	Buffer
0	1	0
1	0	1

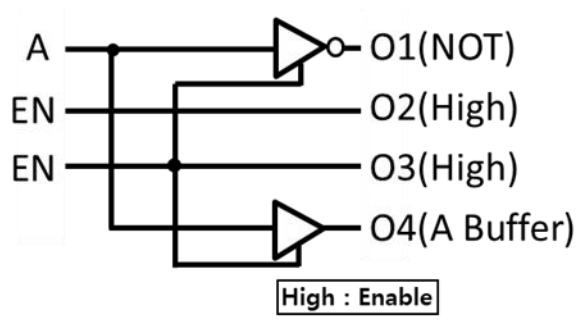

Figure 3.16. Logic circuits and truth tables implemented in the microfluidic device for NOT gate and Buffer logic gates.

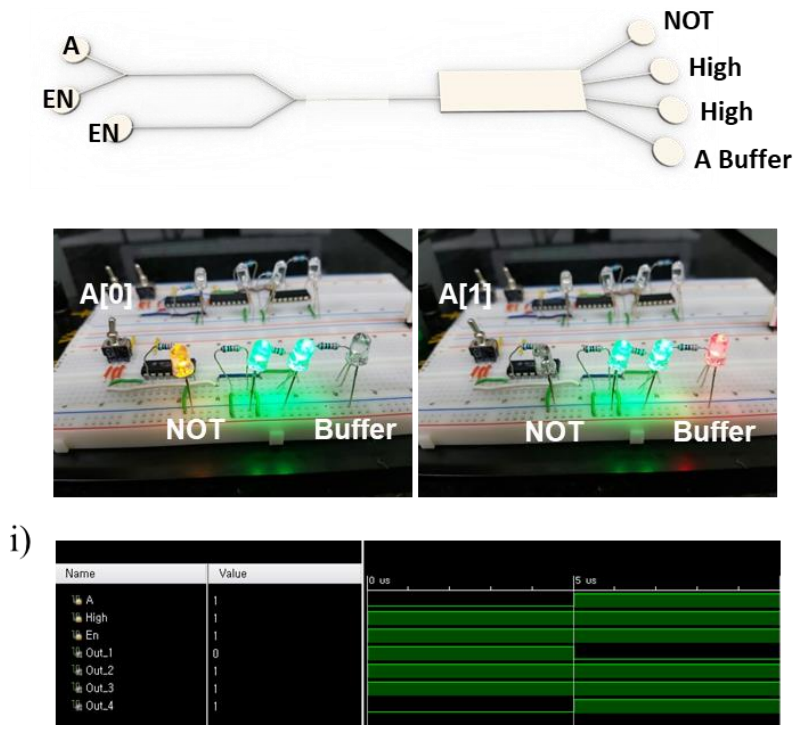

Figure 3.17. Common electronic logic circuit matched with the microfluidic logic device. By using one input logic IC chips, NOT and Buffer operation were realized by electronic logic and i) signal waves.

3.5. Summary

We demonstrate a microfluidic logic device using particle dynamics in the viscoelastic flow. Elementary logic gates are implemented in a microfluidic platform with use of multiple line particle focusing. Numerical simulation of viscoelastic fluids in the device is carried out to understand the mechanism of the multiple line focusing and to determine the dimension and geometry of the microfluidic device able to operate the logic gates. The particle migration in the microfluidic device is manipulated via the control of elastic and inertial forces of fluid. The fluidic logic circuits proposed in this study are compared with common electronic logic circuits. The findings show that the microfluidic logic gates based on the inertia-elastic particle focusing enables a wide range of such operations as XOR, OR, AND, NOT, and Buffer. We foresee that the microfluidic logic device introduced can show a possibility of developing new fascinating platforms by merging different engineering technologies.

3.6. References

1. Kim, H., Bose, R., Shen, T. C., Solomon, G. S. & Waks, E. A quantum logic gate between a solid-state quantum bit and a photon. *Nat. Photonics* **7,** 373–377 (2013).
2. Monroe, C., Meekhof, D. M., King, B. E., Itano, W. M. & Wineland, D. J. Demonstration of a fundamental quantum logic gate. *Phys. Rev. Lett.* **75,** 4714–4717 (1995).
3. Siuti, P., Yazbek, J. & Lu, T. K. Synthetic circuits integrating logic and memory in living cells. *Nat. Biotechnol.* **31,** 448–52 (2013).
4. Qu, D. H., Ji, F. Y., Wang, Q. C. & Tian, H. A double INHIBIT logic gate employing configuration and fluorescence changes. *Adv. Mater.* **18,** 2035–2038 (2006).
5. De Rossi, D. Electronic textiles: a logical step. *Nat. Mater.* **6,** 328–329 (2007).
6. Bonnet, J., Yin, P., Ortiz, M. E., Subsoontorn, P. & Endy, D. Amplifying genetic logic gates. *Science (80-.).* **340,** 599–603 (2013).
7. Elbaz, J. *et al.* DNA computing circuits using libraries of DNAzyme subunits. *Nat. Nanotechnol.* **5,** 417–422 (2010).
8. Elbaz, J., Wang, Z. G., Orbach, R. & Willner, L. pH-stimulated concurrent mechanical activation of two DNA ‘tweezers’. A ‘SET-RESET’ logic gate system. *Nano Lett.* **9,** 4510–4514 (2009).
9. Li, W., Yang, Y., Yan, H. & Liu, Y. Three-input majority logic gate and multiple input logic circuit based on DNA strand displacement. *Nano Lett.* **13,** 2980–2988 (2013).
10. Han, J. Computing: Naturally random. *Nat. Nanotechnol.* **10,** 1011–1012 (2015).
11. Liu, X., Aizen, R., Freeman, R., Yehezkeli, O. & Willner, I. Multiplexed aptasensors and amplified dna sensors using functionalized graphene oxide: Application for logic gate operations. *ACS Nano* **6,** 3553–3563 (2012).
12. Li, F., Anzel, P., Yang, J., Kevrekidis, P. G. & Daraio, C. Granular acoustic switches and logic elements. *Nat. Commun.* **5,** 5311 (2014).
13. Nikitin, M. P., Shipunova, V. O., Deyev, S. M. & Nikitin, P. I. Biocomputing based on particle disassembly. *Nat. Nanotechnol.* **9,** 716–722 (2014).

14. Park, K. S., Jung, C. & Park, H. G. 'Illusionary' Polymerase activity triggered by metal ions: Use for molecular logic-gate operations. *Angew. Chemie - Int. Ed.* **49,** 9757–9760 (2010).
15. Park, K. S., Seo, M. W., Jung, C., Lee, J. Y. & Park, H. G. Simple and universal platform for logic gate operations based on molecular beacon probes. *Small* **8,** 2203–2212 (2012).
16. Prezioso, M. *et al.* A single-device universal logic gate based on a magnetically enhanced memristor. *Adv. Mater.* **25,** 534–538 (2013).
17. Ikeda, M. *et al.* Installing logic-gate responses to a variety of biological substances in supramolecular hydrogel-enzyme hybrids. *Nat. Chem.* **6,** 511–8 (2014).
18. Prakash, M. & Gershenfeld, N. Microfluidic Bubble Logic. *Science* **274501,** 832–836 (2007).
19. Stucki, J. D. & Guenat, O. T. A microfluidic bubble trap and oscillator. *Lab a Chip - Miniaturisation Chem. Biol.* **15,** 4393–4397 (2015).
20. Mosadegh, B., Bersano-Begey, T., Park, J. Y., Burns, M. a & Takayama, S. Next-generation integrated microfluidic circuits. *Lab Chip* **11,** 2813–2818 (2011).
21. Groisman, A., Enzelberger, M. & Quake, S. R. Microfluidic memory and control devices. *Science* **300,** 955–958 (2003).
22. Zhan, W. & Crooks, R. M. Microelectrochemical logic circuits. *J. Am. Chem. Soc.* **125,** 9934–9935 (2003).
23. Zhao, Y. & Chakrabarty, K. Fault diagnosis in lab-on-chip using digital microfluidic logic gates. *J. Electron. Test. Theory Appl.* **27,** 69–83 (2011).
24. Gong, J. & Kim, C.-J. C. J. All-electronic droplet generation on-chip with real-time feedback control for EWOD digital microfluidics. *Lab Chip* **8,** 898–906 (2008).
25. Barbulovic-Nad, I., Yang, H., Park, P. S. & Wheeler, A. R. Digital microfluidics for cell-based assays. *Lab Chip* **8,** 519–26 (2008).
26. Beebe, D. J. *et al.* Functional hydrogel structures for autonomous flow control inside microfluidic channels : Abstract : Nature. *Nature* **404,** 588–590 (2000).
27. Oh, K. W., Lee, K., Ahn, B. & Furlani, E. P. Design of pressure-driven microfluidic networks using electric circuit analogy. *Lab Chip* **12,** 515–45 (2012).
28. Nam, Y., Kim, M. & Kim, T. Pneumatically controlled multi-level microchannel for separation and extraction of microparticles. *Sensors Actuators, B Chem.* **190,**

86–92 (2014).

29. Ramalingam, N. *et al.* Fluidic Logic Used in a Systems Approach to Enable Integrated Single-Cell Functional Analysis. *Front. Bioeng. Biotechnol.* **4,** (2016).
30. Devaraju, N. S. G. K. & Unger, M. A. Pressure driven digital logic in PDMS based microfluidic devices fabricated by multilayer soft lithography. *Lab Chip* **12,** 4809 (2012).
31. Cartas-Ayala, M. A., Raafat, M. & Karnik, R. Self-sorting of deformable particles in an asynchronous logic microfluidic circuit. *Small* **9,** 375–381 (2013).
32. Mertaniemi, H., Forchheimer, R., Ikkala, O. & Ras, R. H. A. Rebounding droplet-droplet collisions on superhydrophobic surfaces: From the phenomenon to droplet logic. *Adv. Mater.* **24,** 5738–5743 (2012).
33. Cristobal, G., Benoit, J. P., Joanicot, M. & Ajdari, A. Microfluidic bypass for efficient passive regulation of droplet traffic at a junction. *Appl. Phys. Lett.* **89,** (2006).
34. D'Avino, G. *et al.* Single line particle focusing induced by viscoelasticity of the suspending liquid: theory, experiments and simulations to design a micropipe flow-focuser. *Lab Chip* **12,** 1638 (2012).
35. Del Giudice, F., D'Avino, G., Greco, F., Netti, P. a. & Maffettone, P. L. Effect of fluid rheology on particle migration in a square-shaped microchannel. *Microfluid. Nanofluidics* **19,** 95–104 (2015).
36. Yang, S. H., Lee, D. J., Youn, J. R. & Song, Y. S. Multiple-Line Particle Focusing under Viscoelastic Flow in a Microfluidic Device. *Anal. Chem.* **89,** 3639–3647 (2017).
37. Howard, M. P., Panagiotopoulos, A. Z. & Nikoubashman, A. Inertial and viscoelastic forces on rigid colloids in microfluidic channels. *J. Chem. Phys.* **142,** (2015).
38. Kang, K., Lee, S. S., Hyun, K., Lee, S. J. & Kim, J. M. DNA-based highly tunable particle focuser. *Nat. Commun.* **4,** 2567 (2013).
39. Kim, B. & Kim, J. M. Elasto-inertial particle focusing under the viscoelastic flow of DNA solution in a square channel. *Biomicrofluidics* **10,** (2016).
40. Lee, D. J., Brenner, H., Youn, J. R. & Song, Y. S. Multiplex particle focusing via hydrodynamic force in viscoelastic fluids. *Sci. Rep.* **3,** 3258 (2013).

41. Lim, E. J. *et al.* Inertio-elastic focusing of bioparticles in microchannels at high throughput. *Nat. Commun.* **5,** 4120 (2014).
42. Lim, H., Nam, J. & Shin, S. Lateral migration of particles suspended in viscoelastic fluids in a microchannel flow. *Microfluid. Nanofluidics* **17,** 683–692 (2014).
43. Yang, S., Kim, J. Y., Lee, S. J., Lee, S. S. & Kim, J. M. Sheathless elasto-inertial particle focusing and continuous separation in a straight rectangular microchannel. *Lab Chip* **11,** 266–273 (2011).
44. Yuan, D. *et al.* Dean-flow-coupled elasto-inertial three-dimensional particle focusing under viscoelastic flow in a straight channel with asymmetrical expansion-contraction cavity arrays. *Biomicrofluidics* **9,** (2015).
45. Del Giudice, F. *et al.* Particle alignment in a viscoelastic liquid flowing in a square-shaped microchannel. *Lab Chip* **13,** 4263–71 (2013).
46. Groisman, A. & Quake, S. R. A microfluidic rectifier: Anisotropic flow resistance at low Reynolds numbers. *Phys. Rev. Lett.* **92,** 94501–1 (2004).
47. Romeo, G., D'Avino, G., Greco, F., Netti, P. a & Maffettone, P. L. Viscoelastic flow-focusing in microchannels: scaling properties of the particle radial distributions. *Lab Chip* **13,** 2802 (2013).

Chapter IV.

Smart particle valve for logic circuit

4.1. Introduction

Manipulation of microparticles using a microfluidic device is of fundamental importance in biological, pharmaceutical, and medical sciences. Control methods of suspended particles have been extensively studied for decades in passive and active ways. In a typical passive control method, the particles are aligned or separated by size when experiencing the balance of forces that occur in the flow of Newtonian[1–8] and non-Newtonian fluids.[9–19] Some researches for the active control of particles have been reported using acoustic,[20–24] dielectrophoresis,[25–29] optical power,[30–33] and microvalve systems.[34–38] Especially, the microvalves for the particle/flow control are operated by external stimuli, allowing precise and local manipulation. The flow is generally switched by the fluidic resistance difference induced by transition of fascinating materials such as hydrogel,[37,38] thermo-reversible gelation polymer,[39] elastomer,[40–42] and shape memory polymer.[43,44] The smart materials integrated into the microfluidic system remains challenging, with complex structure and microfabrication issues being a precise particle path control.

Shape memory polymers (SMPs)[45,46] own the functionality to recover their original permanent shape after the shape is deformed. It operates by applying external stimuli such as heating and light irradiation. Molecular chains of SMPs consist of fixing and switching segments, which are related with shape-memory and shape-recovery, respectively. For amorphous SMPs, molecular configuration of the switching segments is transformed depending on the phase state, from glassy to rubbery and vice versa. Large modulus drops due to molecular structure difference drives the shape memory-recovery behavior. Based on this smart function, SMPs have been applied in many research fields such as micro-optics,[47,48] dry adhesion,[49–51] antireflection,[52] and biometrics.[53]

If the ability of SMPs is integrated with the microfluidic system, the flow can be

controlled using pre-entered shape programing, which has great potential for microfluidic fields. So far, few studies about SMPs for a microscale application have been developed with self-designed synthesis methods. Droplets/water wetting was controlled according to the surface hydrophilicity change by the deformable microstructure.[54–57] Also, one of SMPs was used as a microchannel replica instead of poly(dimethylsiloxane) (PDMS). By local heating of the polymer, the water flow was blocked by closing the channel.[43]

In the passive system, microparticles are focused at equilibrium positions by the force balance of elastic force and inertial lift forces under viscoelastic flow. This phenomenon is based on the normal stress difference gradient developed in polymeric solution flow. In the previous works[14], we have demonstrated the multiple-line particle focusing by hydrodynamic mechanism with the forces acting on the particles. Since the rigid particles have negligible interaction and their size is small compared to the channel dimension, it is hard to control the focusing position and the flow path of the particles and as far as we know, the related researches have rarely been reported.

In order to manipulate the path of focused particles as intended, we built the strategy to replace a constituent material of the microchannel from PDMS to the transparent acrylic SMP (Shape memory copolyacrylate, SMCPAc) which was chemically designed and synthesized in our group.[46] Near body temperature, one outlet branch of the SMCPAc microchannel was programmed for the focused particle control. If the focused particles can be adjustable by external stimuli, a microparticle in a fluid can be assigned as a logical value while droplet based logic operation has been mainly addressed in the microfluidic system. With the local deformation of the SMCPAc microchannel, the path of the particles at the downstream was manipulated based on the difference of the hydraulic pressure. After demonstration of the particle control, we suggest a microfluidic logic circuit as an application of the particle valve principle.

4.2. Experimental

4.2.1. Synthesis of SMCPAc

A shape memory polymer should be designed as a basic material of this study. We employed SMCPAc (shape memory copolyacrylate, SMCPAc) developed in our previous work.[46] A precursor solution consisted of two monomers mixed at the same ratio (methyl methacrylate (MMA, Daejung Chem., Republic of Korea) and butyl methacrylate (BMA, Daejung Chem., Republic of Korea)) and a cross-linker (polyethyleneglycol dimethacrylate (PEGDMA), Mw=525, Sigma-Aldrich, United States). The volumetric ratio of the monomers to the cross-linker was 1:2. In the solution, 0.2 wt% of a photo initiator (phenylbis(2, 4, 6-trimethylbenzoyl) phosphine oxide (BAPOs), Sigma-Aldrich, United States) was incorporated into the precursor solution. The precursor solution was vigorously mixed with a vortex mixer for 30 minutes and then used in the synthesis. The synthetic scheme was described in **Figure 4.1**.

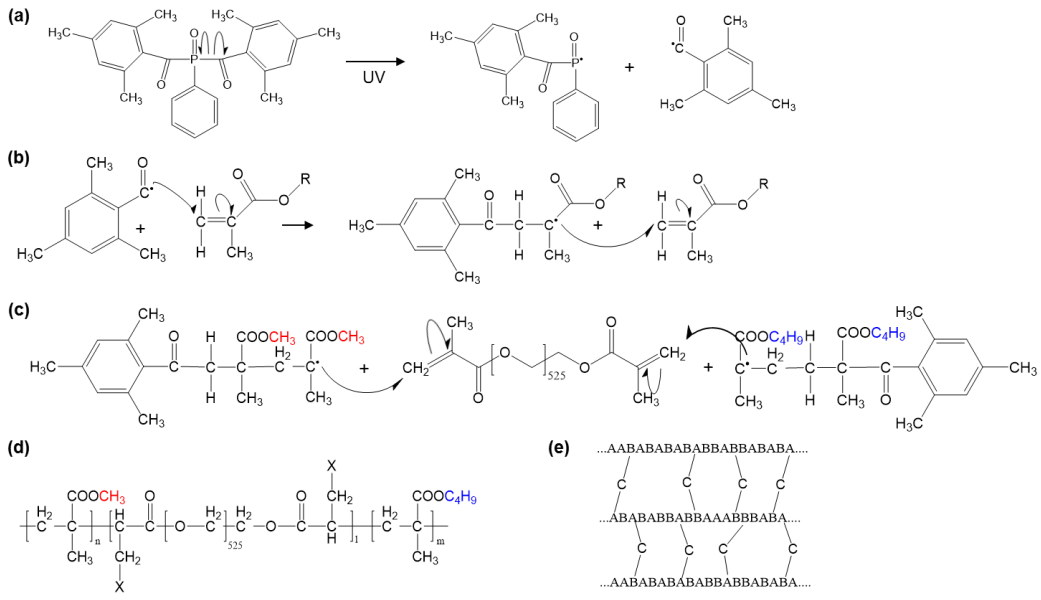

Figure 4.1. Chemical reaction scheme for SMCPAc synthesis. (a) Initiation of the reaction by irradiation of UV light. (b) Extension of the prepolymer chains by the generated free radical electrons. (c) Crosslinking reaction between the pre-polymer chains and the crosslinker. (d) Suggested chemical structure of the SMCPAc. (e) Schematic illustration of the SMCPAc consisted of the monomers ('A' and 'B' indicate MMA and BMA, respectively) and the crosslinker ('C' means PEGDMA).

4.2.2. Design and fabrication of a microchannel

A SMCPAc microchannel was replicated using the negative poly(dimethylsiloxane), a PDMS mold. The microchannel with a channel aspect ratio (AR=W/H) of 4 consists of two inlets and two outlets. The fabrication process capable of multiple replication of the mold was selected in order to prevent the damage of a SU-8 master. A prepolymer and a curing agent of the PDMS were mixed together and poured onto the SU-8 master. After degassing the mixture in a vacuum chamber for 1 hour, it was cured at 70°C for 4 hours. The negative PDMS channel was peeled off from the master. In order to replicate the positive ultraviolet (UV) resin channel, the UV resin (NOA 68, EO Edmund) was poured over the negative PDMS replica and irradiated with UV light (λ~365 nm) for 2 hours at room temperature. Then the positive UV resin mold was peeled off and the surface was silanated for 6 hours by vapor deposition of trichloro(1H,1H,2H,2H-perfluoro-octyl)silane to easily detach the SMCPAc channel.

A mold for the fabrication of the SMCPAc channel was made of the positive UV resin channel and a slide glass with 1 mm spacers. The precursor of SMCPAc was injected into the gap and synthesized by UV irradiation (λ=~365 nm) for 15 minutes at 40℃. The transparent SMCPAc channel was detached from the mold and punched with the Harris Uni-Core 1.5-mm-diameter puncher (Sigma-Aldrich, United States), enabling the connection of the tubes to reservoirs. For the stability of the tubing, the PDMS was bonded at the location of the reservoirs. The SMCPAc channel was bonded onto an ITO glass spin-coated with PDMS using a plasma-treatment for stronger bonding strength. The thickness of the PDMS film coated on the ITO glass was about 1 mm. The fabrication process of SMCPAc channel and cross-section of the fabricated microchannel are schematically illustrated in **Figure 4.2** and **Figure 4.3**.

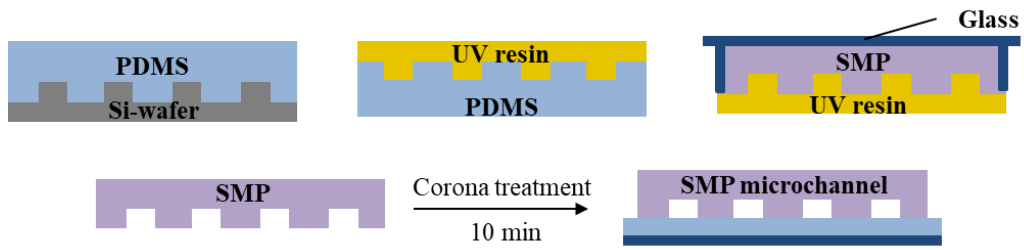

Figure 4.2. A schematic illustration for fabrication of SMCPAc microchannel.

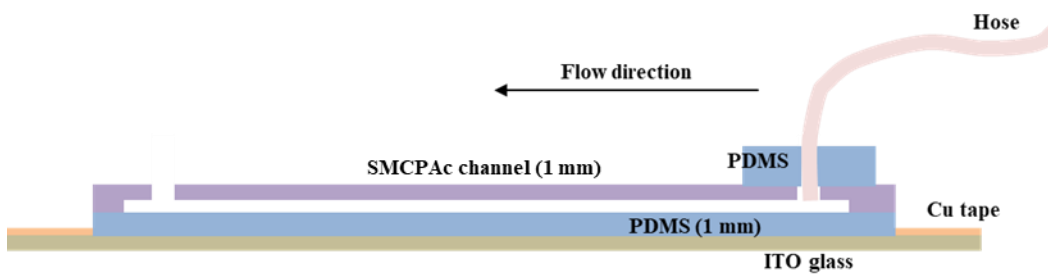

Figure 4.3. Cross-sectional conformation of fabricated SMCPAc microchannel.

4.2.3. Experimental setup

Polyethylene oxide (PEO, Mw=2M, Sigma-Aldrich, United States) powder was dissolved into 22 wt% aqueous-glycerol solutions to produce the diluted polymer solutions. 2500 ppm of the diluted PEO solution, which has high elasticity, was prepared to neglect the shear-gradient lift force hydrodynamically induced in the microchannel. Fluorescent polystyrene (FPS) particles (Polysciences, United States) with a 6.42 μm diameter were suspended in a viscoelastic medium with a small amount of the surfactant TWEEN® 20 (Sigma-Aldrich, United States). The solution was injected into the microchannel using a KDS 200 syringe pump (KD Scientific, United States) with the flow rate of 0.1 ml/hr.

For the shape programming process, the SMCPAc channel has to be heated up to the operation temperature of 40℃. For Joule heating, a power supply (APS 3005S, ATTEN Ins.) was connected to the copper tapes attached at the both ends of an ITO glass. Silver paste was used for reducing contact resistance between the copper tapes and the ITO glass. Simultaneously, the PS particles suspended in the PEO solution were injected into the SMCPAc microchannel by using a syringe pump.

By using an IX 53 inverted optical microscope (Olympus, United States) and a AcquCAM 23G charge-coupled device (CCD) camera, the particle migration was observed in the microchannel. Particle focusing location was analyzed using Image-Pro Plus (Media Cybernetics, Inc., United States) and ImageJ (National Institutes of Health, United States) software.

4.2.4. Thermomechanical properties of SMCPAc

Thermomechanical property of SMCPAc was investigated by running a dynamic mechanical analysis (DMA) machine (TA Q800 DMA, United States) as shown in Figure 4.4. The cut specimen to 1×5.3×40 mm^3 was held in the tensile mode clamp. Storage and loss modulus of the sample were examined under 0.2% strain, 1 Hz frequency, 125% force track, 0.001 N preload, and 5℃/min heating rate.

A cyclic stress-strain-temperature curve was obtained using the same machine, TA Q800 DMA. A 3-point-bending test was proceeded after holding the same specimen used in the tensile test. After heating the specimen above transition onset temperature (T_{onset}, 40℃ in our case), 2% strain was applied at the center of the specimen. After then, the specimen was cooled to 0℃ for shape-fixing. After unloading, the specimen was heated up to 40℃.

4.2.5. Rheological properties of flow

Dilute polyethylene oxide (PEO) solution is used as a viscoelastic medium due to its viscous and elastic properties. The rheological properties of viscoelastic solutions, such as the steady shear viscosity (η) and the relaxation time (λ), are measured by using a rotational rheometer (MCR-301, Anton Paar) and a capillary breakup extensional rheometer (CaBER-1, ThermoHakke), respectively. In the previous study, the distance between the double particle focusing lines was closer as the concentration increase of PEO solution from 1500 ppm to 3000 ppm. Due to the channel geometrical features of y-shaped inlets, the particle equilibrium regions can be bifurcated. And it facilitates double-line particle focusing by the additional shear-gradient force. In order to generate high elastic force outweighing the inertial forces, 2500 ppm PEO solution was selected and the double line particle focusing was observed with the short distance between the focusing lines in the channel. Since the temperature of the deformed microchannel increased up to 40℃ in the shape-recovery process, the viscosity of 2500 ppm PEO solution was also measured at 40℃.

For the 2500 ppm PEO solution, the elastic force (Wi) is more dominant than the

inertial force (*Re*) as elasticity (*El*=*Wi*/*Re*=$\frac{\lambda\eta(W+H)}{\rho W^2 H}$) becomes larger than unity. The Reynolds number(*Re)* is a dimensionless number that indicates the comparison of inertial and viscous effects, which is defined as $Re = \frac{\rho u D_h}{\eta} = \frac{2\rho Q}{\eta(W+H)}$, where H is the channel height, W is the channel width, ρ is the fluid density, u is the fluid velocity, and $D_h = 2WH/(W+H)$ is the hydraulic diameter of the rectangular channel. The elastic force is described by the Weissenberg number, *Wi*, which is defined as $Wi = \lambda\dot{\gamma}_c = \frac{2\lambda Q}{HW^2}$, where$\dot{\gamma}_c$ is the shear rate. The fluid elasticity is characterized by the ratio of *Re* to *Wi*. In this study, the elasticity of the solution was calculated according to the temperature increase. The viscosities were measured by increasing the temperature by using a rotational bulk-rheometer MCR 301 (**Figure 4.5**). At room temperature, *El* is above the unity as 1.366. As the temperature increases up to 40℃, the elasticity decreased as 0.933 due to the decrease of the solution viscosity.

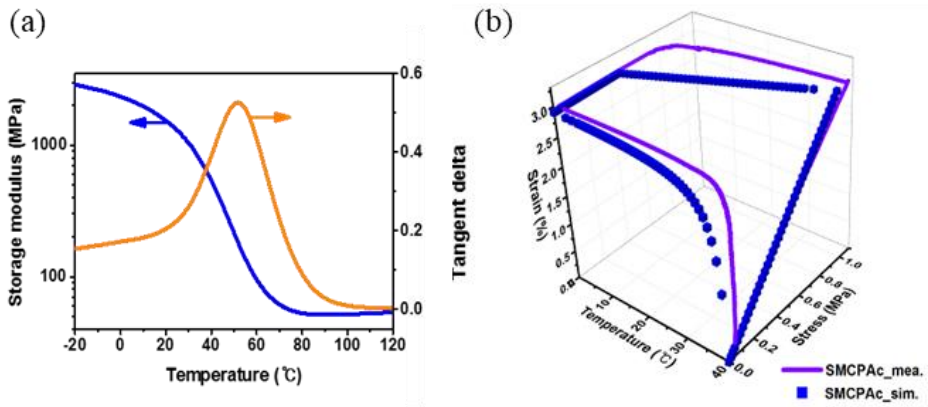

Figure 4.4. Thermomechanical analysis results for SMCPAc. (A) Storage modulus and tangent delta of the SMCPAc as a function of temperature. (B) Stress-strain-temperature curve for the SMCPAc.

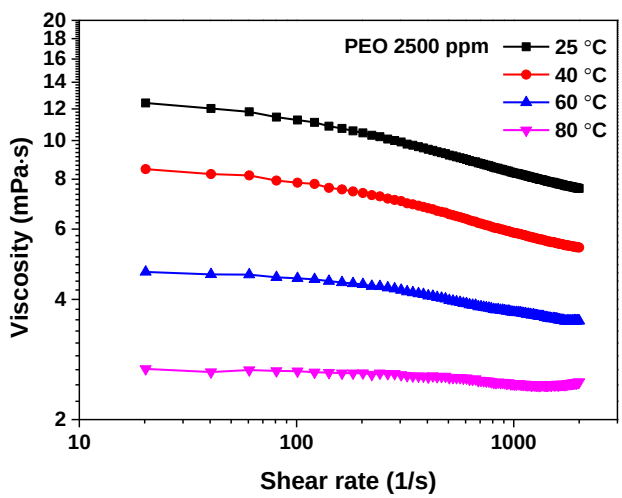

Figure 4.5. Viscosities of 2500 ppm Poly(ethylene oxide) aqueous solution measured at different temperature (25℃, 40℃, 60℃, 80℃).

4.3. Numerical analysis

4.3.1. Shape memory-recovery simulation

Numerical analysis was performed to model the shape memory behavior of SMCPAc theoretically and to confirm stress distribution of the material during deformation. ABAQUS/CAE, a commercial finite element method program, was employed in the simulation with codded subroutines UMAT and SDVINI. A hyperelastic model, Neo-Hookean model, was a constitutive model of the material with assumptions that strain energy exists as a form of Helmholtz potential during deformation of the material and the material is isothermal and compressible.

The mechanism of a shape memory polymer is as follows. The strain energy is generated on the region that receives stress and stored during glass transition. Due to the increased stiffness of SMCPAc after the cooling process, SMCPAc maintains its deformed figure even after unloading. The following heating process restores the original shape of SMCPAc by lowering the stiffness through phase transition from glassy state to rubbery state.

Khanolkar *et al.*[58,59] proposed the hyperelastic model as follows and we referred their works to simulate our material. The material properties should be varied with temperature condition. Two parts of strain energy function (ψ), glassy phase parts (α) and rubbery phase parts $(1-\alpha)$, were simultaneously considered in modeling. Constitutive equations of SMCPAc were defined as

$$\psi_t = (1-\alpha)\psi_r + \int_{t_i}^{\tau} \psi_g d\tau \tag{4-1}$$

$$\psi_r = C_{10}\left(\bar{I}_{\kappa_r} - 3\right) + \frac{1}{D_1}\left(J_{\kappa_r} - 1\right)^2 \tag{4-2}$$

$$\psi_g = C_{20}\left(\bar{I}_{\kappa_{g(t)}} - 3\right) + \frac{1}{D_2}\left(J_{\kappa_{g(t)}} - 1\right)^2 \tag{4-3}$$

, where ψ_t is the total stored strain energy function, ψ_r is the stored strain energy function at rubbery regions, ψ_g is the stored strain energy function at glassy regions, $\bar{I}_{\kappa_r}$

and $\bar{I}_{\kappa_{g(t)}}$ are the first invariants of isochoric parts of the right Cauchy-Green deformation tensor, and J_{κ_r} and $J_{\kappa_{g(t)}}$ are the Jacobian matrices of material deformation. Subscripts 'r' and 'g' indicate the properties about rubbery phase and glassy phase, respectively. $C_{10}(=\mu_r/2)$, $C_{20}(=\mu_g/2)$ are the material input parameters for hyperelastic models related to shear modulus (μ), and $D_1(=2/K_r)$, $D_2(=2/K_g)$ related to bulk modulus (K).

Above material functions are continuously updated following a change of phase states relevant with temperature condition. In the subroutine code, it was assumed that phase transition is linearly proportional to the glassy state fraction (α). Glassy region content (α) is governed by temperature variation as

$$\alpha = \frac{T_{rub}-T}{T_{gla}-T_{rub}} \tag{4-4}$$

, where T_{rub} is the temperature when fully rubbery state, T_{gla} is the temperature when fully glassy state, and T is the current temperature condition.

The UMAT subroutine code was produced to model the non-linear material behaviors of SMCPAc. Based on Kirchhoff stress-Newman strain rate, stiffness tensor matrix (ℂ) was developed as

$$\mathbb{C}_{IJ} = \frac{1}{2}\left(\mathbb{C}_{ijkl} + \mathbb{C}_{ijlk}\right) \tag{4-5}$$

$$\begin{aligned}\mathbb{C}_{ijkl} = \Bigg\{&(1-\alpha)\left\{\left(\frac{2\boldsymbol{C}_{10}}{J_{\kappa_a}}\right)\left(\delta_{ik}\overline{\boldsymbol{B}}_{a_{ij}} + \overline{\boldsymbol{B}}_{a_{ik}}\delta_{jl}\right) + \left(-\frac{4}{3}\frac{\boldsymbol{C}_{10}}{J_{\kappa_a}}\right)\left(\delta_{kl}\overline{\boldsymbol{B}}_{a_{ij}} + \overline{\boldsymbol{B}}_{a_{kl}}\delta_{ij}\right) + \right.\\ &\left.\left(\frac{4}{9}\frac{C_{10}}{J_{\kappa_a}}\right)(tr\overline{\boldsymbol{B}}_a)\delta_{kl}\delta_{ij} + \left(\frac{2}{D_1}\right)\left(2J_{\kappa_a}-1\right)\delta_{kl}\delta_{ij}\right\} + (\alpha)\left\{\left(\frac{2\boldsymbol{C}_{20}}{J_{\kappa_{g(t)}}}\right)\left(\delta_{ik}\overline{\boldsymbol{B}}_{g_{ij}} + \overline{\boldsymbol{B}}_{g_{ik}}\delta_{jl}\right) + \right.\\ &\left.\left(-\frac{4}{3}\frac{\boldsymbol{C}_{20}}{J_{\kappa_{g(t)}}}\right)\left(\delta_{kl}\overline{\boldsymbol{B}}_{g_{ij}} + \overline{\boldsymbol{B}}_{g_{kl}}\delta_{ij}\right) + \left(\frac{4}{9}\frac{C_{20}}{J_{\kappa_{g(t)}}}\right)(tr\overline{\boldsymbol{B}}_g)\delta_{kl}\delta_{ij} + \left(\frac{2}{D_2}\right)\left(2J_{\kappa_{g(t)}}-1\right)\delta_{kl}\delta_{ij}\right\}\Bigg\}\end{aligned} \tag{4-6}$$

, where δ_{ij} is Kronecker delta and $\overline{\mathbf{B}}$ is the isochoric parts of deformation components for glassy and rubbery state. The UMAT code is invoked to update the stress and phase

states of each node with a use of the SDIVINI code at the end of every time step. The material parameters required in the simulation were obtained from the experimental results of isothermal tensile tests at different temperatures as tabulated in **Table 4.1** and **Table 4.2**.

A 3-D model was built regarding the real channel geometry. SMCPAc rectangular microchannel with aspect ratio of 4:1 was located above PDMS layer with the same thickness along y-direction (**Figure 4.6**). Two layers were merged like as one domain and 8 node linear brick meshes were generated for the calculation. The finer mesh was generated only along the edges of the channel in order to prevent time-consuming process. An analytical rigid plate was described for loading boundary condition. The bottom of merged domain was pinned for all directions. The steps for the simulation were consist of loading, cooling, unloading, and heating. In the loading step, the glassy region content (α) was 0.125 at the temperature of 40℃. When the analytical rigid plate pressed the upper surface of SMCPAc part, 4:1 microchannel was distorted as the similar shape in the SEM image. The deformed shape was fixed at the cooling step (α=0.625). At the followed unloading step, the plate was slowly removed from the SMCPAc and PDMS layer was fully-recovered since it doesn't have shape memory function. Finally, the deformed SMCPAc microchannel shape was recovered at the heating step. The von Mises stress was contoured in Results and Discussion section.

Table 4.1. The employed hyper-elastic material parameters for SMCPAc.

	SMCPAc
T_r [a] [°C]	60
T_g [b] [°C]	-20
C_{10} [MPa]	6
C_{20} [MPa]	370
D_1 [1/MPa]	0.06
D_2 [1/MPa]	0.001
ν [c] [-]	0.35

Table 4.2. The employed linear elastic material parameters for PDMS.

	PDMS
E [d] [MPa]	13.2
ν [-]	0.45

[a] T_r: Temperature for fully rubbery phase;
[b] T_g: Temperature for fully glassy phase;
[c] ν: Poisson's ratio.
[d] E: Young's modulus;

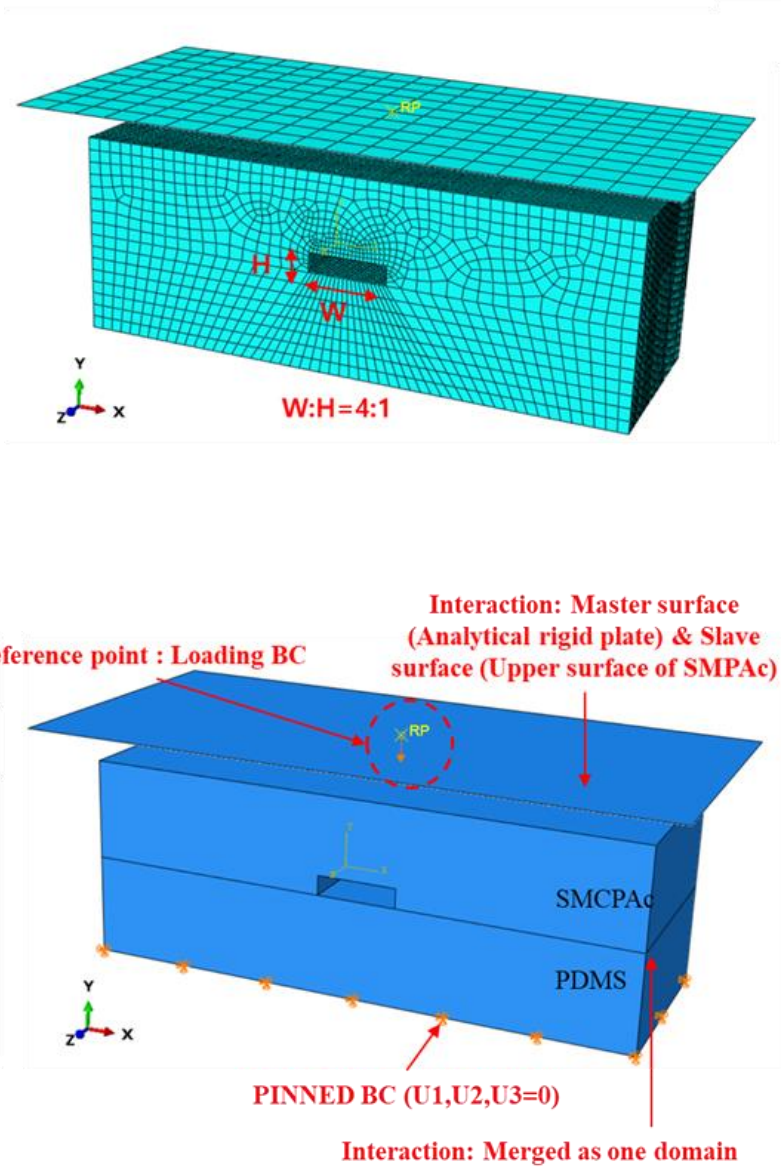

Figure 4.6. Geometrical design, mesh, and boundary condition for the structural analysis.

4.3.2. Heat transfer analysis

In order to predict a temperature increase of the SMCPAc microchannel through the PDMS film on the ITO glass, heat transfer between the materials was theoretically calculated by using the commercial program COMSOL Multiphysics based on finite element method (FEM). The PDMS film was designed to have thickness of 1 mm. To solve the temperature distribution of the SMCPAc layer, the following governing equation was given.

$$\rho C_p \frac{\partial T}{\partial t} = \nabla \cdot (k \nabla T) + Q \tag{4-7}$$

, where ρ is the density, C_p is the heat capacity, k is the thermal conductivity, and Q is the heat source. The input variables above were given as intrinsic material properties for each layer. The heat source (Q) was defined as P_b/A for the heating process, where P_b is the supplied power and A is the surface area of the layer. For the cooling process, the heat source was defined as zero. The convective heat flux condition was set as the boundary condition as follow.

$$q_0 = n_s \cdot k \nabla T = h \cdot (T_{ext} - T) \tag{4-8}$$

, where n_s is the surface normal vector, h is the convective heat transfer coefficient, and T_{ext} is the external temperature.

4.3.3. Hydraulic resistance calculation

Numerical simulation was carried out to analyze pressure difference of the deformed channel cross-section by using the commercial program COMSOL Multiphysics based on finite element method (FEM). Since we used the polymer solution with viscoelastic properties, the first normal stress difference distribution (N_1) was also considered during the calculation.

For the simulation, the steady-state momentum equation of Navier-Stokes equations was expressed as

$$\rho\left(\frac{\partial \mathbf{u}}{\partial t} + (\boldsymbol{u}\cdot\nabla)\boldsymbol{u}\right) = \nabla\cdot(-pI + \eta_s(\nabla\boldsymbol{u} + (\nabla\boldsymbol{u})^T) + \boldsymbol{T}) \quad (4\text{-}9)$$

And the extra stress source was given by

$$\boldsymbol{T} + \lambda\left(\frac{\partial \boldsymbol{T}}{\partial t} + (\boldsymbol{u}\cdot\nabla)\boldsymbol{T} - [(\nabla\boldsymbol{u})\cdot\boldsymbol{T} + \boldsymbol{T}\cdot(\nabla\boldsymbol{u})^T]\right) = 2\eta_p(\nabla\boldsymbol{u} + (\nabla\boldsymbol{u})^T) \quad (4\text{-}10)$$

, where $\boldsymbol{u}$ is the velocity vector, λ is the characteristic relaxation time, η_p and η_s are the viscosities of polymer and solvent, respectively, and the total viscosity (η) is defined as $\eta_p + \eta_s$. These two equations are solved together with the continuity equation of Navier-Stokes equations. The pressure and velocity fields were obtained for the cases of non-deformed and deformed channel cross-section.

4.4. Results and Discussion

4.4.1. Objective of the study

In previous study, we demonstrated double line particle focusing under viscoelastic flow by using channel geometrical effects.[14] The designed microchannel was used for focusing particles suspended in polymeric solution based on the elasto-inertial force competition in this study. Width and height of a used microchannel was 100 μm and 25 μm, and it has 2 inlets and 2 outlets with y-shaped geometry. Here, the aligned particles with double lines at the downstream was manipulated by the local shape programming causing the outlet pressure difference and **Figure 4.7** shows a schematic illustration. If a shape of channel cross-section is deformed by the locally applied force and subsequently programmed, the magnitude of hydraulic resistance in the channel can be changed comparing to that in the original shape channel. The difference of resistance directly determines the particle flow since the hydraulic resistance is related to the hydraulic pressure distribution in the microchannel. As an application of the particle control using the SMP function, we materialized the Boolean logic value on the microchannel system for the logical control of the particles at microscale. Here, the existence of the particles in a channel indicates binary logical number, 1, for the microfluidic logic operation. For example, the inlet A is assigned as the binary number 1 when the PEO solution with particles is injected into an inlet A. If the pure PEO solution without particles is injected into an inlet B, the inlet B indicates the binary value 0. In this study, the shape deformation of the channel cross-section determines the particle streamlines due to the difference of the local hydraulic resistance. Thus, the status of the channel deformation is included as the input variable for the logic operation and it is nominated as S. Consequently, the SMCPAc microchannel corresponds to the integrated logic circuit of $A + S \cdot B$ and the detailed description about logical operation will be given later. By using Joule-heating, the microchannel was heated for the deformation and the experimental setup is simply illustrated in **Figure 4.8**.

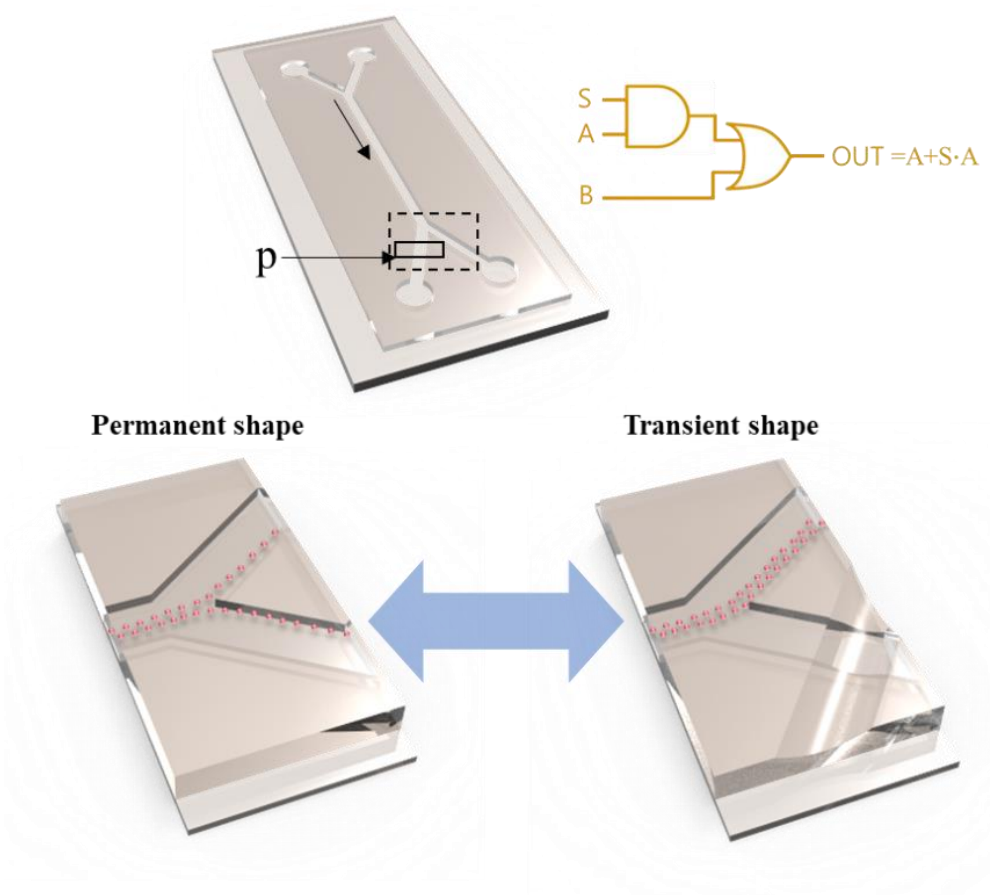

Figure 4.7. Schematic description of particle path control by shape programming of a SMCPAc-based microchannel. The particle path control of a microchannel by shape programming.

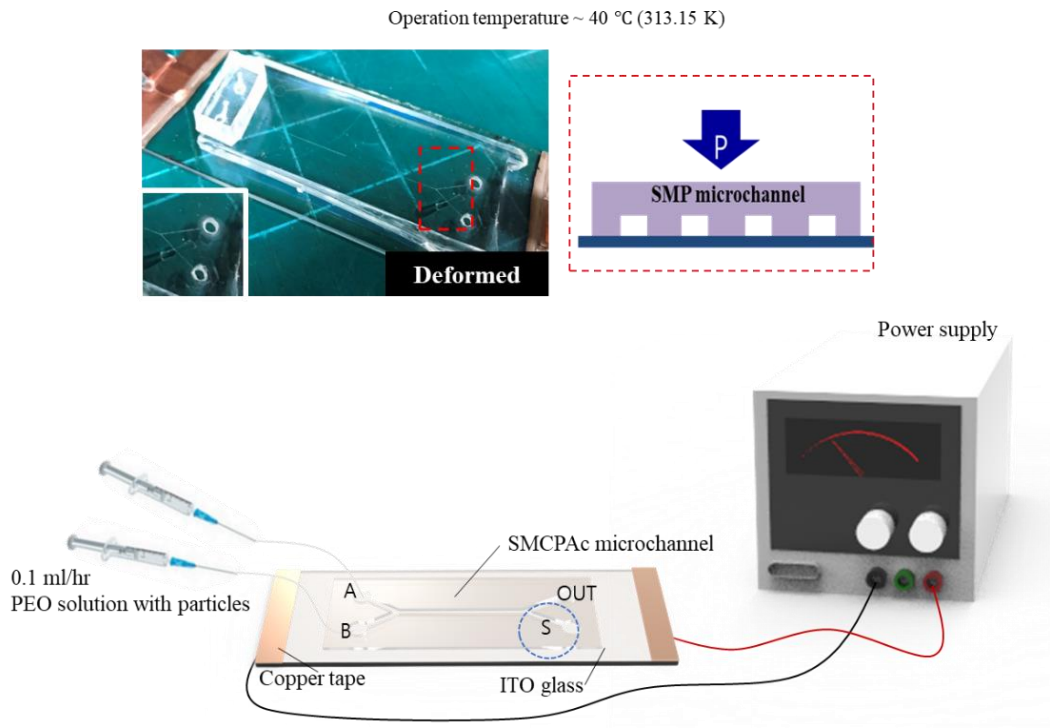

Figure 4.8. Experimental setup for operation of the shape programming and active logic operation.

4.4.2. Simulation results

4.4.2.1. Heat transfer

In order to predict a temperature increase of the SMCPAc microchannel through the PDMS film on the ITO glass, heat transfer between the materials was theoretically calculated by using the commercial program COMSOL Multiphysics based on finite element method (FEM) (**Figure 4.9**). Detail simulation method is demonstrated in Numerical Analysis section. The substrate consists of the ITO glass and the PDMS film. As a result of the simulation, the upper surface temperature of the PDMS-ITO substrate was compared with that of the ITO glass without PDMS film for verifying the heat transfer through the SMCPAc microchannel. The thickness of the PDMS thin film was experimentally measured as 1 mm. The power was given with 2.1 W (7 V, 0.3A) and applied for 2 minutes for heating the microchannel. The applied voltage was removed right after the heating process and the microchannel was cooled under the natural convection condition. As results, while 7 V was applied, the surface temperature reached a maximum value about 317 K (43.85℃) after 2 minutes as shown in **Figure 4.9 (b)**. After removing the power source, the channel was cooled down to room temperature, which is below the operation temperature, for 2 minutes. The numerical analysis results were well matched experimentally, so they were used as appropriate conditions in actual experiments.

4.4.2.2. Hydraulic pressure and resistance

Local hydraulic pressure and resistance were numerically calculated to analyze pressure difference of the deformed channel cross-section, by using the finite element method. An upper convective Maxwell (UCM) model was employed as a viscoelastic constitutive model of the polymer solution and the simulation method is given in Numerical Analysis section. Considering the effects by the stress development in viscoelastic flow, the pressure and velocity fields in the channel were obtained as shown in **Figure 4.10**. The particles are focused at the downstream by the force balance between the elastic force originated from

intrinsic properties of the fluid and the inertial force induced by flow condition. The elastic force acting on the particles is governed by the first normal stress difference ($N_1 = \tau_{xx} - \tau_{yy}$) of the flow, where τ_{xx} is the normal stress along the flow direction and τ_{yy} is the normal stress along the perpendicular direction of the flow. The minimal value of the first normal stress difference distribution is widely formed by the geometrical feature of the channel, which corresponds to the equilibrium region of the particles. Also, the double inlets induce the additional inertial forces. The particles introduced from the double inlets are entrained in the initially injected streamlines and forced by the wall-repulsion force ($F_{L,W}$) and the shear gradient force ($F_{L,S}$) for each inlet. When each streamline merges to the straight channel, the particles are multiple focused at the channel center region due to the force balance by the geometrical features.

In this study, we controlled the path of the double particle focusing lines by the difference of the hydraulic pressure using a shape-programmable function of the SMCPAc channel. When the channel outlets have a permanent shape, the pressure and velocity fields symmetrically develop along the channel downstream. Thus, the double particle focusing lines are bifurcated by the Y-shaped outlets. If the one outlet is deformed by the external force, the hydraulic pressure of the deformed outlet becomes higher than that of another non-deformed outlet. Consequently, the double focused particles flow through the non-deformed outlet with a relatively lower pressure, and no particle flows through the deformed outlet. In **Figure 4.10**, the change of pressure difference (Δp) after the channel deformation was numerically calculated. It was confirmed that the pressure magnitude of the deformed outlet is 1.099 times higher than that of the non-deformed outlet, resulting in the maximum velocity. The local hydraulic resistance ($R_H = \frac{\Delta p}{Q}$) was also calculated for each shape of the channel, where Q is the flow rate. By substituting the terms of the pressure and the flow rate obtained from numerical calculation to the equation above, the resistance of the deformed output is evaluated to be 1.83 times higher than that of the original shape output.

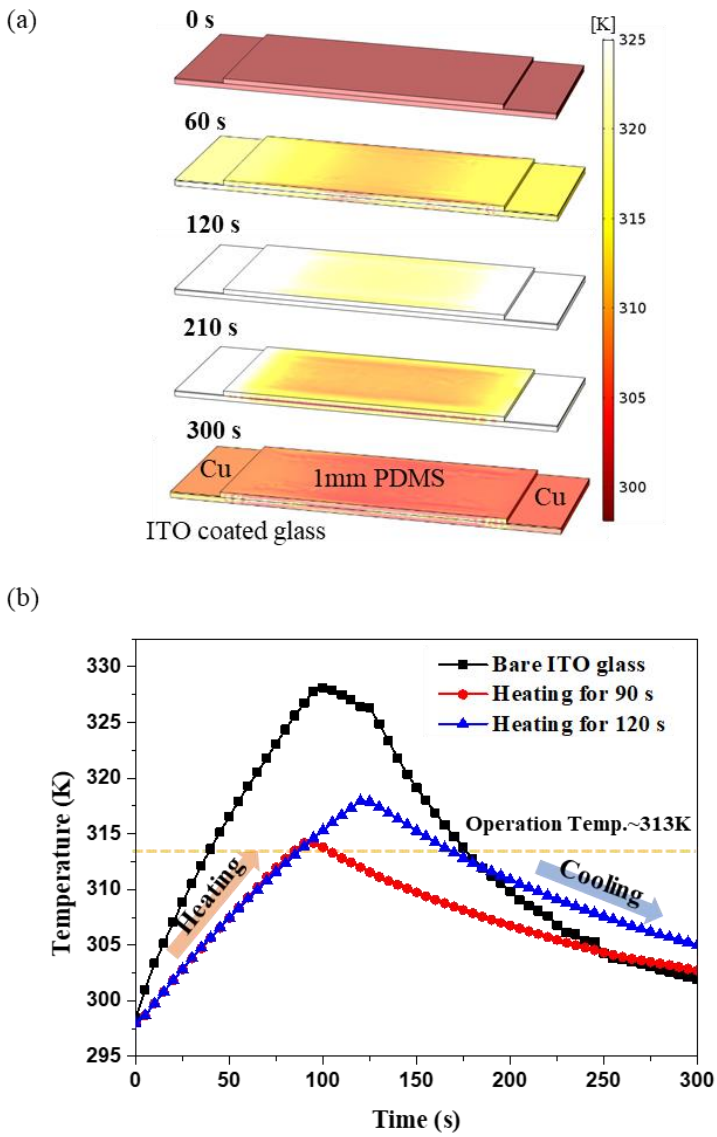

Figure 4.9. Numerical calculation results for heat transfer analyses of the SMCPAc microfluidic system. (a) Temperature gradient of the PDMS-covered ITO glass with time step (b) Comparison of the temperature gradient between the bare ITO glass and the PDMS-covered ITO glass while Joule-heating.

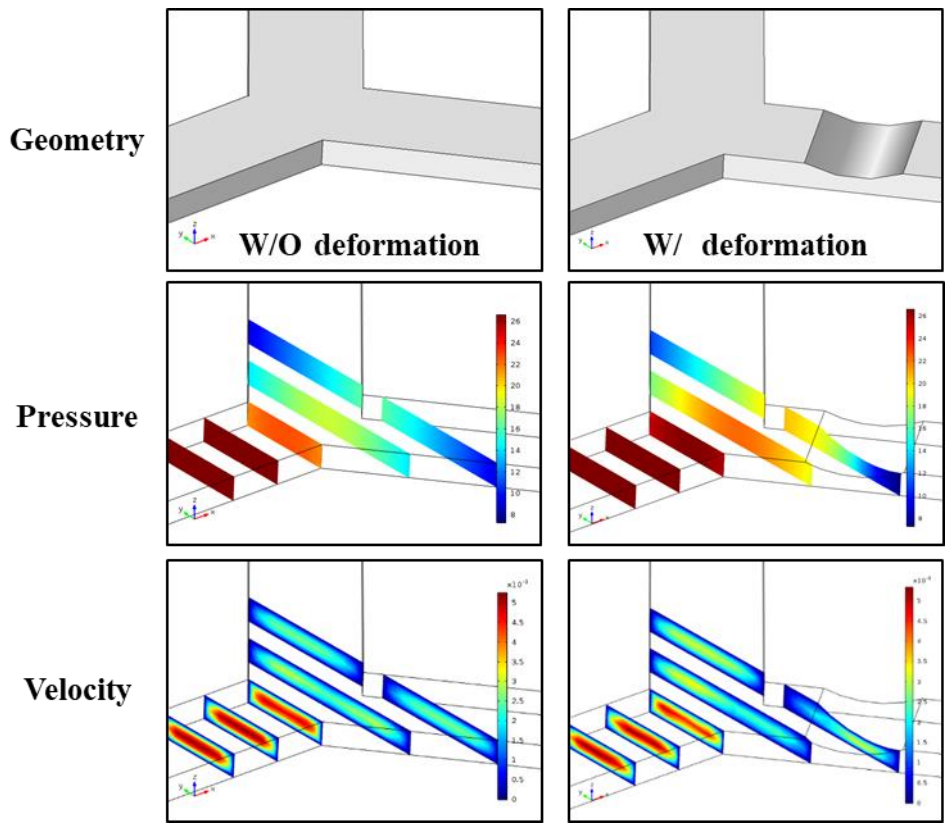

Figure 4.10. Numerical calculation results for hydraulic pressure analyses of the SMCPAc microfluidic system. Pressure (Pa) and velocity field (m/s) distribution according to a shape-state of the microchannel under the viscoelastic flow.

4.4.2.3. Channel shape memory-recovery

Numerical analysis was carried out to theoretically figure out shape memory-recovery behavior of the microchannel system by using ABAQUS/CAE with user subroutines. The von-Mises stress contours of the system were visualized as simulation results and are shown in **Figure 4.11**. A hyperelastic Neo-Hookean model[52,59,60], which assumes the existence of stored strain energy as a form of Helmholtz potential when deforming a material, was employed as a constitutive model of the SMCPAc with temperature dependent material variables. On the other hand, the PDMS was modeled as a linear elastic model using only Young's modulus. Details about the simulation method are explained in Numerical Analysis section.

In the rubbery state at 40 ℃, the microchannel was deformed by applying a compressive force (**Fig. 4.11 (i→ii)**). In this state, the stiffness of the SMCPAc is higher than that of the PDMS, so a larger stress is distributed in the SMCPAc region. The applied stress was saved as entropic elastic energy by the cooling process which generates glassy regions in the SMCPAc (**Fig. 4.11 (ii→iii)**). This phenomenon was considered in modeling by updating the glassy phase part (α) depending on temperature. The stored energy at the SMAPc region was not released even after the subsequent unloading step because it cannot overcome the increased stiffness of the SMCPAc by the generated glassy regions (**Fig. 4.11 (iii→iv)**). However, the elastic energy stacked at the PDMS region was easily released immediately after the unloading step began. In heating up to 40℃ again, the rubbery regions were created by micro Brownian motion of polymeric chains and the shape recovery to the permanent original state was triggered (**Fig. 4.11 (iv→i)**).

The slight mismatch of the deformed channel shape between the observed and simulated shapes is presumed to be due to the assumptions of linear proportional phase transition and ignoring the viscoelastic properties of the material. Notwithstanding, the numerical modeling successfully visualized the stress distribution in the system and explained the underlying story for shape memory-recovery behavior.

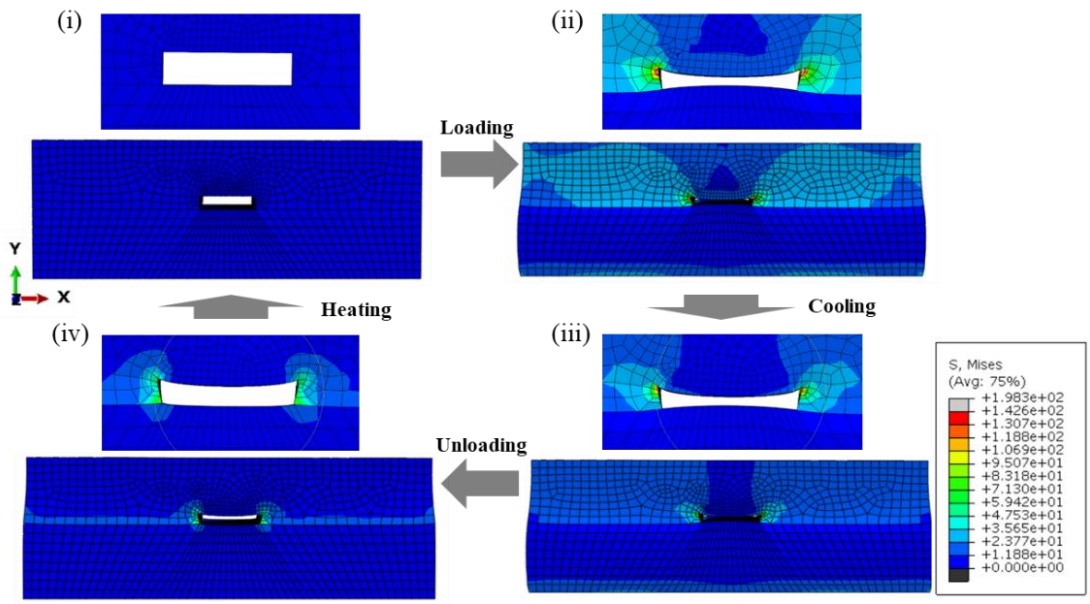

Figure 4.11. Numerical analysis results for the shape memory-recovery behavior of the SMCPAc microchannel; Von Mises stress contours at (i) the initial state, (ii) the deformed state, (iii) the cooled state, (iv) the unloaded state, and (iv → i) the shape-recovery of the microchannel.

4.4.3. Analytical calculation of hydraulic resistance

The cross-sectional channel shape was measured by analyzing the taken SEM (scanning electron microscope) images (**Figure 4.12**). The initial hydraulic diameter ($D_i = \frac{2WH}{(W+H)}$) was measured as 41.489 μm. After the microchannel was heated up to 40℃ by using the 7 V power supply, it was pressed by a thin rectangular object with dimension of 4×0.8 mm^2. After the shape fixing process by cooling the channel at room temperature, the average deformed diameter (D_d) was examined as 31.526 μm. Shape fixity (S_f) was defined as

$$S_f = \frac{D_d - D_i}{D_s - D_i} \times 100 \quad (4\text{-}11)$$

, where D_s is the hydraulic diameter at maximum deformation and it was evaluated to be approximately 91.39 %. The deformed channel was recovered to its original shape by Joule heating again. The channel heights after the shape programming process and recovery process were compared by analyzing the SEM images. Shape recovery ratio (R_r) was defined as

$$R_r = \frac{D_d - D_f}{D_d - D_i} \times 100 \quad (4\text{-}12)$$

, where D_f is the channel hydraulic diameter after the shape recovery step. The shape recovery ratio of the SMCPAc microchannel was about 77.49%. This value is high enough to be used repeatedly for shape-programmable devices. In particular, the high shape recovery ratio is a very significant precondition of the basic material in this study because it is directly related to the accuracy of the particle control.

The hydraulic diameter difference of outlets causes difference of the flow rate of fluids flowing through each outlet. The flow rate of original channel (Q_o) and the flow rate of deformed channel (Q_d) was simply calculated by the relation of $Q \propto D_h^4$. The flow rate ratio $\left(\frac{Q_d}{Q_o}\right)$ was about 0.295 meaning that approximately 70% of streamlines in the straight channel flow towards the non-deformed outlet when one of the outlets was deformed. By

substituting the measured channel width and height from SEM images, the hydraulic resistance (R_H) of original shape and deformed shape was analytically calculated. The definition of R_H as follows was used,

$$R_H = \frac{\Delta p}{Q} = \frac{12\eta L}{wh^3\left(1-\frac{h}{w}\left(\frac{192}{\pi^5}\sum_{n=1,3,5}^{\infty}\frac{1}{n^5}\tan h\left(\frac{n\pi w}{2h}\right)\right)\right)} \cong \frac{12\eta L}{wh^3\left(1-0.63\frac{h}{w}\right)} \quad (4\text{-}13)$$

, where Q is the flow rate, L is the unit length, w and h is the channel width and height, and η is the fluid viscosity. The resistance of the cross-section with original rectangular shape was calculated as 2564.79 GPa·s/m^3, while the resistance of deformed channel was 6018.09 GPa·s/m^3. Consequently, the resistance of the deformed output is evaluated to be 2.35 times higher than that of the original shape output. As a result of this mathematical calculation, the quantitative difference of hydraulic pressure by shape programming could be predicted theoretically.

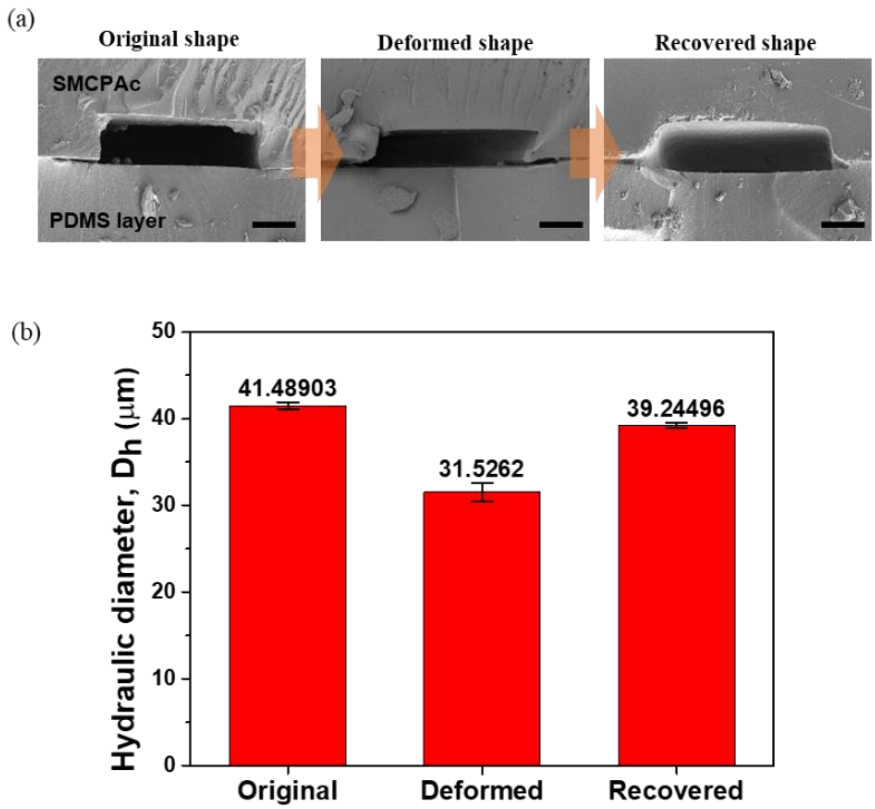

Figure 4.12. Shape memory-recovery behavior of the SMCPAc microchannel. Observed SEM images on each shape-state and their hydraulic diameter. (a) Cross-sectional figures at initial, after the shape-programming, and after the shape-recovery step. The scale bar indicates 25 μm. (b) Evaluated hydraulic diameters for each shape of the microchannel from the SEM images.

4.4.4. Experimental verification

Finally, the path control of the double focused particles was experimentally verified as shown in **Figure 4.13**. The particle solution composed of 6.42 μm diameter fluorescent polystyrene (PS) particles and the 2500 ppm PEO solution were introduced into the inlets with 0.1 ml/hr of the flow rate. The PS particles were randomly dispersed in the particle solution through the inlets. By the force balance of the elastic force and inertia, the particles were double focused at the downstream. **Figure 4.13** shows optical images of the particle flow in an original and a deformed microchannel. The particles were introduced into both inlets. The injected particles through the upper inlet were aligned at the upper location of the channel width near the outlets, while the particles from the lower inlet were focused at the lower position at the downstream. As predicted in the numerical results, the double particle focusing lines separately exited through each outlet due to the symmetrical pressure distribution of outlets. When the outlet below was deformed by applying weight, the most particles move towards the upper outlet which has relatively lower pressure.

In the previous works, the microchannel for the desired logic operations should be custom designed at the initial step since the particles were passively controlled without options after passive manipulation. In the meanwhile, in this study, an active microfluidic logic system was realized by using the shape programmable polymer (*i.e.*, SMCPAc), which can be turned on and off by external stimuli and forces. The Boolean numbers, 0 and 1, are implemented according to the presence and absence of the flow with dispersed particles in a channel. If the solution with the particles are injected into the A inlet, A is assigned to the logical value 1. If the pure solution without the particles flows through the B inlet, B inlet has the logical value 0. Here, the particle existence in an outlet is influenced by the channel deformation, thus, the channel shape can be one of the logical variables. For the logic operation, three logical inputs were defined as S for the channel deformation, A and B for the particle presence. The output O (*e.g.*, upper outlet in **Figure 4.14**) was determined by the combination of inputs. The aligned particles from the lower inlet flow were only influenced by the channel deformation causing the increase of hydraulic pressure. Condition of A, B, and S was tabulated in **Figure 4.14(b)** by using a binary number. As a result, the integrated logic circuit, $A + S \cdot B$, corresponds with the microfluidic system using SMCPAc.

Due to the higher pressure and resistance of the shape-programmed output, particles suspended in viscoelastic flow were pushed towards the other output, which retained its original shape, even when the particles are hydrodynamically aligned. The path control of the particles by local deformation allows a new microfluidic logic operation, resulting in an integrated logic circuit in this study. We foresee that simple and sophisticated treatment methods will be helpful in fields of Point-of-care (POC), Lab on a chip (LOC), and health-medical care with logical functions.

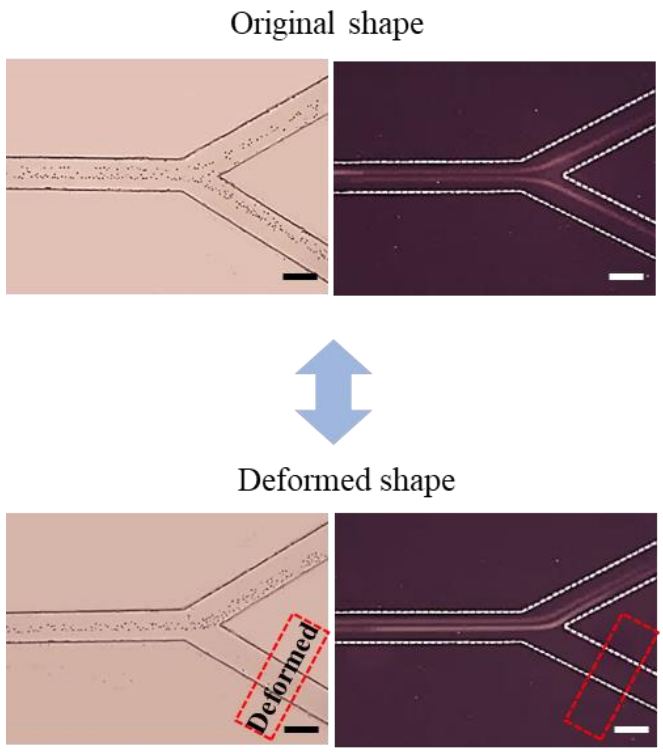

Figure 4.13. Smart particle manipulation by shape memory effect of the microchannel. (A) Double focused particles flow through both outlets with the same pressure distribution when the channel is non-deformed. When the lower outlet (red dashed box) is deformed and programmed, the double focused particles flow towards the upper outlet. The scale bar indicates 100 μm.

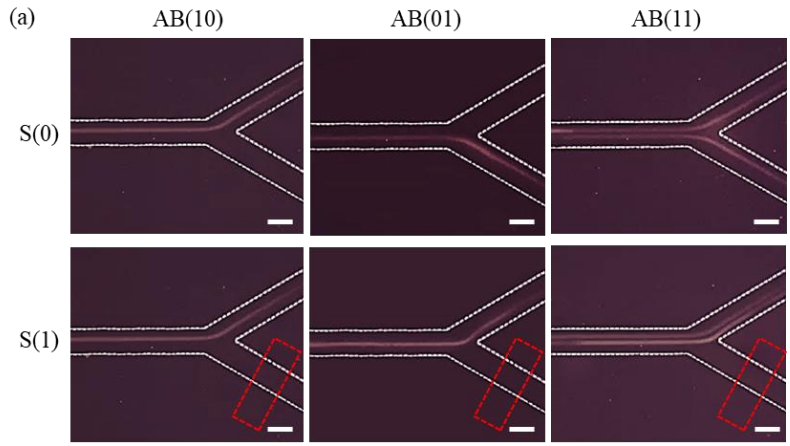

(b)

S	A	B	OUT
0	0	0	0
0	1	0	1
0	0	1	0
0	1	1	1
1	0	0	0
1	1	0	1
1	0	1	1
1	1	1	1

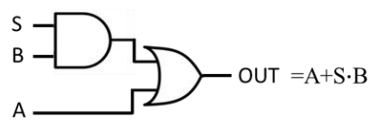

Figure 4.14. Logical operation by using shape memory effect. (a) Logical operation of the upper outlet when the inlets (A and B) and the channel shape (S) are assigned as logical values. (Particle existence:1, Deformed lower outlet (S):1, otherwise:0) (b) An integrated logic circuit and a truth table for the upper outlet. The scale bar indicates 100 μm.

4.5. Summary

We demonstrate a new smart method of the particle manipulation in a microfluidic system by using a transparent shape memory polymer, SMCPAc. By replacing PDMS with SMCPAc as a constituent material of microfluidic devices, the active logic system was facile driven with only shape programming and recovery. The shape memory function of the microchannel near body temperature was observed from the SEM images and its underlying story was numerically figured out. The double particle focusing lines under the viscoelastic flow were generated on each outlet when the channel is in its original shape. However, when the shape programming occurred on one side, no particle line was formed in the deformed side. The hydraulic pressure distribution was numerically calculated in order to understand the control mechanism. The difference of the local hydraulic resistance between the non-deformed outlet and the deformed outlet play a pivotal role for the control. The designed microsystem corresponds to the integrated logic circuit, $A + S \cdot B$, according to the presence of the particles in a channel. We ensure that this smart particle control method based on the shape memory polymer and viscoelastic flow can be a breakthrough solution enabling both advanced particle separation systems and fluidic logic devices.

4.6. References

1. Chun, B. & Ladd, A. J. C. Inertial migration of neutrally buoyant particles in a square duct: An investigation of multiple equilibrium positions. *Phys. Fluids* **18,** (2006).
2. Matas, J. P., Morris, J. F. & Guazzelli, É. Inertial migration of rigid spherical particles in Poiseuille flow. *J. Fluid Mech.* **515,** 171–195 (2004).
3. Zhou, J. & Papautsky, I. Fundamentals of inertial focusing in microchannels. *Lab Chip* **13,** 1121 (2013).
4. Bhagat, A. A. S., Kuntaegowdanahalli, S. S. & Papautsky, I. Enhanced particle filtration in straight microchannels using shear-modulated inertial migration. in *Physics of Fluids* **20,** (2008).
5. Park, J.-S., Song, S.-H. & Jung, H.-I. Continuous focusing of microparticles using inertial lift force and vorticity via multi-orifice microfluidic channels. *Lab Chip* **9,** 939–948 (2009).
6. Amini, H., Sollier, E., Weaver, W. M. & Di Carlo, D. Intrinsic particle-induced lateral transport in microchannels. *Proc. Natl. Acad. Sci.* **109,** 11593–11598 (2012).
7. Guan, G. *et al.* Spiral microchannel with rectangular and trapezoidal cross-sections for size based particle separation. *Sci. Rep.* **3,** 1475 (2013).
8. Di Carlo, D. Inertial microfluidics. *Lab Chip* **9,** 3038 (2009).
9. Villone, M. M., D'Avino, G., Hulsen, M. A., Greco, F. & Maffettone, P. L. Simulations of viscoelasticity-induced focusing of particles in pressure-driven micro-slit flow. *J. Nonnewton. Fluid Mech.* **166,** 1396–1405 (2011).
10. Young Kim, J., Won Ahn, S., Sik Lee, S. & Min Kim, J. Lateral migration and focusing of colloidal particles and DNA molecules under viscoelastic flow. *Lab Chip* **12,** 2807 (2012).
11. Lee, D. J., Brenner, H., Youn, J. R. & Song, Y. S. Multiplex particle focusing via hydrodynamic force in viscoelastic fluids. *Sci. Rep.* **3,** 3258 (2013).
12. D'Avino, G. *et al.* Single line particle focusing induced by viscoelasticity of the suspending liquid: theory, experiments and simulations to design a micropipe flow-focuser. *Lab Chip* **12,** 1638 (2012).

13. Howard, M. P., Panagiotopoulos, A. Z. & Nikoubashman, A. Inertial and viscoelastic forces on rigid colloids in microfluidic channels. *J. Chem. Phys.* **142,** (2015).
14. Yang, S. H., Lee, D. J., Youn, J. R. & Song, Y. S. Multiple-Line Particle Focusing under Viscoelastic Flow in a Microfluidic Device. *Anal. Chem.* **89,** (2017).
15. Del Giudice, F., D'Avino, G., Greco, F., Netti, P. a. & Maffettone, P. L. Effect of fluid rheology on particle migration in a square-shaped microchannel. *Microfluid. Nanofluidics* **19,** 95–104 (2015).
16. Yuan, D. *et al.* Dean-flow-coupled elasto-inertial three-dimensional particle focusing under viscoelastic flow in a straight channel with asymmetrical expansion-contraction cavity arrays. *Biomicrofluidics* **9,** (2015).
17. Leshansky, A. M., Bransky, A., Korin, N. & Dinnar, U. Tunable nonlinear viscoelastic 'focusing' in a microfluidic device. *Phys. Rev. Lett.* **98,** (2007).
18. Lim, E. J. *et al.* Inertio-elastic focusing of bioparticles in microchannels at high throughput. *Nat. Commun.* **5,** 4120 (2014).
19. Lu, X., Zhu, L., Hua, R. mao & Xuan, X. Continuous sheath-free separation of particles by shape in viscoelastic fluids. *Appl. Phys. Lett.* **107,** (2015).
20. Wiklund, M. & Hertz, H. M. Ultrasonic enhancement of bead-based bioaffinity assays. *Lab Chip* **6,** 1279 (2006).
21. Petersson, F., Nilsson, A., Holm, C., Jönsson, H. & Laurell, T. Separation of lipids from blood utilizing ultrasonic standing waves in microfluidic channels. *Analyst* **129,** 938–943 (2004).
22. Kapishnikov, S., Kantsler, V. & Steinberg, V. Continuous particle size separation and size sorting using ultrasound in a microchannel. *J. Stat. Mech. Theory Exp.* (2006). doi:10.1088/1742-5468/2006/01/P01012
23. Hawkes, J. J. & Coakley, W. T. Force field particle filter, combining ultrasound standing waves and laminar flow. *Sensors Actuators, B Chem.* **75,** 213–222 (2001).
24. Li, F., Anzel, P., Yang, J., Kevrekidis, P. G. & Daraio, C. Granular acoustic switches and logic elements. *Nat. Commun.* **5,** 5311 (2014).
25. Vahey, M. D. & Voldman, J. An equilibrium method for continuous-flow cell sorting using dielectrophoresis. *Anal. Chem.* **80,** 3135–3143 (2008).
26. Gagnon, Z. & Chang, H. C. Aligning fast alternating current electroosmotic flow

fields and characteristic frequencies with dielectrophoretic traps to achieve rapid bacteria detection. *Electrophoresis* **26,** 3725–3737 (2005).

27. Cheng, I. F., Chang, H. C., Hou, D. & Chang, H. C. An integrated dielectrophoretic chip for continuous bioparticle filtering, focusing, sorting, trapping, and detecting. in *Biomicrofluidics* **1,** (2007).
28. Gordon, J. E., Gagnon, Z. & Chang, H. C. Dielectrophoretic discrimination of bovine red blood cell starvation age by buffer selection and membrane cross-linking. *Biomicrofluidics* **1,** (2007).
29. Gascoyne, P. R. C. & Vykoukal, J. Particle separation by dielectrophoresis. *Electrophoresis* **23,** 1973–1983 (2002).
30. Chiou, P. Y., Ohta, A. T. & Wu, M. C. Massively parallel manipulation of single cells and microparticles using optical images. *Nature* **436,** 370–372 (2005).
31. Ohta, A. T. *et al.* Optically controlled cell discrimination and trapping using optoelectronic tweezers. *IEEE J. Sel. Top. Quantum Electron.* **13,** 235–242 (2007).
32. Roichman, Y., Wong, V. & Grier, D. G. Colloidal transport through optical tweezer arrays. *Phys. Rev. E - Stat. Nonlinear, Soft Matter Phys.* **75,** (2007).
33. Wang, X. *et al.* Enhanced cell sorting and manipulation with combined optical tweezer and microfluidic chip technologies. *Lab Chip* **11,** 3656 (2011).
34. Zeng, S., Li, B., Su, X., Qin, J. & Lin, B. Microvalve-actuated precise control of individual droplets in microfluidic devices. *Lab Chip* **9,** 1340 (2009).
35. Roberts, D. C. *et al.* A piezoelectric microvalve for compact high-frequency, high-differential pressure hydraulic micropumping systems. *J. Microelectromechanical Syst.* **12,** 81–92 (2003).
36. Cartas-Ayala, M. A., Raafat, M. & Karnik, R. Self-sorting of deformable particles in an asynchronous logic microfluidic circuit. *Small* **9,** 375–381 (2013).
37. Beebe, D. J. *et al.* Functional hydrogel structures for autonomous flow control inside microfluidic channels : Abstract : Nature. *Nature* **404,** 588–590 (2000).
38. Kwon, G. H. *et al.* Electrically-driven hydrogel actuators in microfluidic channels: fabrication, characterization, and biological application. *Lab Chip* **10,** 1604 (2010).
39. Ozaki, K. *et al.* Microfluidic cell sorter with flow switching triggered by a sol-gel transition of a thermo-reversible gelation polymer. *Sensors Actuators, B Chem.* **150,** 449–455 (2010).

40. Finkelmann, H., Greve, A. & Warner, M. The elastic anisotropy of nematic elastomers. *Eur. Phys. J. E* **5,** 281–293 (2001).
41. Del Giudice, F. *et al.* Rheometry-on-a-chip: measuring the relaxation time of a viscoelastic liquid through particle migration in microchannel flows. *Lab Chip* **15,** 783–792 (2015).
42. S??nchez-Ferrer, A. *et al.* Liquid-crystalline elastomer microvalve for microfluidics. *Adv. Mater.* **23,** 4526–4530 (2011).
43. Ebara, M., Uto, K., Idota, N., Hoffman, J. M. & Aoyagi, T. Rewritable and shape-memory soft matter with dynamically tunable microchannel geometry in a biological temperature range. *Soft Matter* **9,** 3074 (2013).
44. Vyawahare, S., Sitaula, S., Martin, S., Adalian, D. & Scherer, A. Electronic control of elastomeric microfluidic circuits with shape memory actuators. *Lab Chip* **8,** 1530 (2008).
45. Xie, T. Recent advances in polymer shape memory. *Polymer (Guildf).* **52,** 4985–5000 (2011).
46. Park, J. H., Kim, H., Youn, J. R. & Song, Y. S. Strategic Design and Fabrication of Acrylic Shape Memory Polymers. *Smart Mater. Struct.* **26,** 85026 (2017).
47. Xu, H. *et al.* Deformable, programmable, and shape-memorizing micro-optics. *Adv. Funct. Mater.* **23,** 3299–3306 (2013).
48. Xie, T., Xiao, X., Li, J. & Wang, R. Encoding localized strain history through wrinkle based structural colors. *Adv. Mater.* **22,** 4390–4394 (2010).
49. Eisenhaure, J. D., Xie, T., Varghese, S. & Kim, S. Microstructured shape memory polymer surfaces with reversible dry adhesion. *ACS Appl. Mater. Interfaces* **5,** 7714–7717 (2013).
50. Tao, X. & Xingcheng, X. Self-peeling reversible dry adhesive system. *Chem. Mater.* **20,** 2866–2868 (2008).
51. Kim, S., Sitti, M., Xie, T. & Xiao, X. Reversible dry micro-fibrillar adhesives with thermally controllable adhesion. *Soft Matter* **5,** 3689 (2009).
52. Park, J., Youn, J. R. & Song, Y. S. Sustainable antireflection using recoverable nanopattern arrays. *J. Mater. Chem. C* (2017). doi:10.1039/C7TC02942J
53. Park, J., Youn, J. R. & Song, Y. S. Carbon Nanotube Embedded Nanostructure for Biometrics. *ACS Appl. Mater. Interfaces* **ASAP artic,** (2017).

54. Park, J. K. & Kim, S. Droplet manipulation on a structured shape memory polymer surface. *Lab Chip* **17,** 1793–1801 (2017).
55. Wang, S. *et al.* Controlling flow behavior of water in microfluidics with a chemically patterned anisotropic wetting surface. *Langmuir* **31,** 4032–4039 (2015).
56. Zhang, P. *et al.* Bioinspired Smart Peristome Surface for Temperature-Controlled Unidirectional Water Spreading. *ACS Appl. Mater. Interfaces* **9,** 5645–5652 (2017).
57. Chen, C. M. & Yang, S. Directed water shedding on high-aspect-ratio shape memory polymer micropillar arrays. *Adv. Mater.* **26,** 1283–1288 (2014).
58. Khanolkar, M. Constitutive modeling of glassy shape memory polymers. *Njit* 125 (2010).
59. Barot, G. & Rao, I. J. Constitutive modeling of the mechanics associated with crystallizable shape memory polymers. *Zeitschrift fur Angew. Math. und Phys.* **57,** 652–681 (2006).
60. Jeon, S. *et al.* Fullerene Embedded Shape Memory Nanolens Array. *Sci. Rep.* **3,** 3269 (2013).

Chapter V.

Particle focusing by normal stress components

5.1. Introduction

Particle handling based on the viscoelastic fluid is an emerging technique that has been developed over the past 10 years owing to its simplicity and high-quality focusing in a wide range of flow rates.[1–14] Since an early experimental work by Leshansky *et al.*[15] introduced the particle focusing in a slit channel that is due to an imbalance among the normal stresses imposed onto particles, the particle-focusing behavior in viscoelastic fluids has received substantial interest and widely been studied.[2, 3, 6–9, 11–13, 15–18] Later, Yang *et al.* demonstrated the particle focusing in viscoelastic fluids at the centerline of a square channel and four corners depending on the combination of the fluid elasticity and inertia.[13] The viscoelasticity-induced particle migration can be realized even when the Reynolds number (*Re*) approaches zero due to the presence of elastic stresses.

The viscoelasticity-induced particle-focusing technique is beneficial in a variety of analytical and processing applications such as sorting of particles,[6–8, 13, 14, 19–27] fluid transportation around particles,[28] measurement of the relaxation times of viscoelastic fluids,[29] and efficient trapping and stretching of particles at a stagnation point.[30, 31] In more detail, an enhanced flow-asymmetry fluid transport around particles was demonstrated using the Giesekus fluids.[28] A chip-based rheometry was also developed by harnessing the focusing behavior of particles to estimate the relaxation time of viscoelastic fluids.[29] This enabled the measurement of relaxation time at the millisecond level without requiring a calibration curve employed in conventional tests. In addition, cell stretching in the microfluidic device was analyzed with use of the viscoelasticity-induced cell focusing and trapping at the stagnation point of the cross-slot channel.[30, 31] In contrast to the inertial

particle-focusing method, the particle-focusing method using viscoelasticity can prevent a random lateral cell distribution and then guarantee rotation-free cell stretching along the channel centerline.

Ho and Leal[32] initiated a theoretical work to understand the lateral-migration mechanism of particles in viscoelastic fluids, in which the migration of particles in a second-order fluid was caused by the spatial gradient of the first normal-stress difference, defined as $N_1 = \tau_{xx} - \tau_{yy}$. Here, the τ_{xx} and the τ_{yy} are the normal-stress components in the flow- and velocity-gradient directions, respectively. The particle migration in the pressure-driven flow of viscoelastic fluids has been simulated considering a wide range of factors such as the effect of inertia and elasticity, the shear-thinning viscosity, the secondary flow, and the blockage ratio.[2, 28, 33] For most viscoelastic polymer solutions, the magnitude of the second normal-stress difference $N_2 = \tau_{yy} - \tau_{zz}$, which produces a secondary flow over the channel cross-section, is much smaller than that of N_1, where the τ_{zz} is the normal-stress component in the rotational direction.[33]

The viscoelasticity-induced focusing of particles in slit flow and square-channel flow were modeled by means of three-dimensional (3D) finite-element simulation.[32,34] The simulation results showed that the particles migrated toward the channel centerline or the closest corners depending on the initial particle positions. A single dimensionless number that can help explain the migration dynamics of a particle in viscoelastic fluids at the low Deborah number was proposed to offer a guideline for the particle focusing.[3, 5] In addition, a potential energy concept was recently introduced by considering the integration of a net-lift force composed of elastic and inertial forces acting on the particles.[35] Typically, it is assumed that τ_{xx} is much larger than τ_{yy} in most complex fluids, resulting in a positive N_1. Basically, movement of particles in a flow is determined by a hydrodynamic stress field imposed on the particle rather than the normal stress differences.

Interestingly, some complex fluids such as liquid-crystal polymer solutions[36] and nanotube suspensions[37] exhibit a negative N_1. When the N_1 becomes negative, an anomalous viscoelastic behavior can be caused by τ_{yy}. For example, carbon nanotube filled polymer shows unusual contraction properties after die extrusion due to the negative N_1.[40, 41] The networks of semiflexible biopolymer gels constituting the cytoskeleton of cells and the extracellular matrix also induce compression of filament in the orthogonal direction

to the shear direction.[40] Nonetheless, the effect of the negative N_1, *i.e.*, τ_{yy} has not been fully understood thus far.

This study aimed at the observation of the particle migration in viscoelastic fluids with the negative N_1. The effect of the normal stress components, τ_{xx} and τ_{yy}, on the lateral migration of particles in the viscoelastic fluid was analyzed. It was shown that the particles in the viscoelastic fluid with the negative N_1 migrated in the opposite direction to the case with the positive N_1. Furthermore, the particles flowing in the solution with the negative N_1 showed opposite focusing behavior compared with those in the solution with the positive N_1. The migration mechanism was investigated experimentally as well as numerically in order to explain the physics behind the movement of particles in a microfluidic channel.

5.2. Experimental

5.2.1. Design and fabrication of a microchannel

The microchannels employed in this study were replicated using a standard soft-lithography method. Straight microfluidic channels with a channel aspect ratio (*AR = W*:*H = 50:25*) of 2 were fabricated. A poly(dimethylsiloxane) (PDMS) was mixed with a curing agent and poured onto an SU-8 master mold. After the prepolymer was degassed in a vacuum chamber for 1 hr, it was cured at 70 °C for 4 hr. The PDMS channel was peeled off and punched with a 1.5-mm-diameter puncher (Harris Uni-Core, Sigma-Aldrich, U.S.A.), enabling the connection of the tubes to reservoirs. The channel was bonded onto a slide glass using a plasma-treatment device (BD-10A, Electro-Technic Products Inc., U.S.A.), and then heated at 120 °C for 1 hr to enhance the bonding strength as described in **Figure 1.1**.

5.2.2. Sample preparation

Two kinds of polymers were dissolved into 22 wt% aqueous glycerol solution to prepare dilute polymer solutions for experiments. Polyethylene oxide (PEO) solutions with the molecular weight of 2,000,000 and Hydroxypropyl cellulose (HPC) solution with the molecular weight of 1,000,000 were purchased from Sigma-Aldrich (U.S.A.), which have a positive N_1 and a negative N_1 distribution due to the unique liquid-crystal structures of HPC, respectively.[41–44] Molecular structure of PEO and HPC is schematically drawn in **Figure 5.1**. To investigate the lateral particle migration in the microchannel, both diluted PEO and HPC solutions were prepared with various polymer concentrations in the range of 100 to 4000 ppm. For HPC solutions, HPC powder was dissolved at 0 ~ 10 ℃ due to lower critical solution temperature (LCST) as shown in **Figure 5.2**. Polystyrene (PS) particles (Polysciences, U.S.A.) with diameters of 5, 10, and 15 μm and fluorescent PS particles (Polysciences, U.S.A.) with a 6.42-μm diameter were suspended in the viscoelastic mediums. A small amount of the surfactant, P1379-25ML TWEEN 20 (Sigma-Aldrich, U.S.A.), was used to prevent the particle aggregation. The diluted polymer

solutions were injected into the microchannel using a syringe pump (KDS 200, KD Scientific, U.S.A.) with flow rates ranging from 0.1 to 2.5 ml/h. An inverted optical microscope (IX 53, Olympus America Inc., U.S.A.) and a vision-hi charge-coupled device (CCD) camera (AcquCAM 23G, JNOpTIC Co. Ltd., South Korea) were used to observe the particle migration in the viscoelastic fluids. The particle-focusing behaviors were analyzed using the Image-Pro Plus (Media Cybernetics, Inc., U.S.A.) and ImageJ (National Institutes of Health, U.S.A.) image-processing software packages.

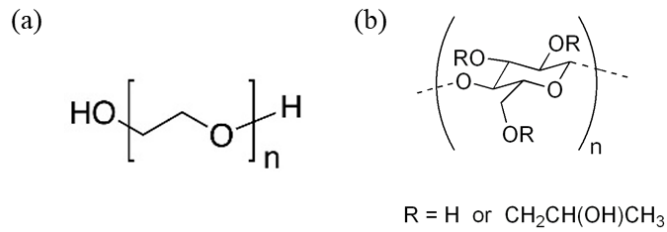

Figure 5.1. Molecular structure of (a) Polyethylene oxide (PEO) and (b) Hydroxypropyl cellulose (HPC).

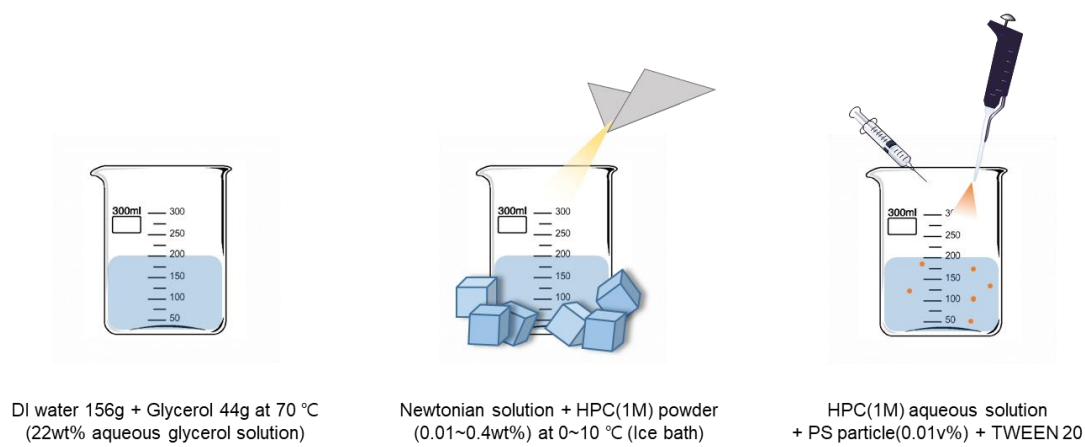

Figure 5.2. Preparation of HPC dilute solutions

5.2.3. Rheological properties of solutions

The rheological properties of the diluted PEO and HPC solutions were measured using a rotational standard rheometer (MCR 302, Anton Paar, Germany). The steady-shear viscosities were determined by using a double-gap geometry (**Figure 5.3**). The rheological characteristics of the diluted PEO and HPC solutions are different due to the different molecular structures and responses to the applied flow. In particular, the HPC molecules in the solution tend to align along the flow direction similar to liquid crystals.[44–47] As a result, the HPC molecules can generate a negative N_1. The origin of the negative N_1 is unclear, although it has been linked with a flow induced molecular orientation and a phase separation in the direction perpendicular to the flow.[39] The N_1 of the viscoelastic solution was generally measured using a cone and plate geometry with 50 mm diameter. In addition, the difference between the first and second normal stress differences was obtained by measuring the normal force with a parallel plate geometry. According to Zimm's theory for polymer solutions, the relaxation time of polymers is dependent on the structural characteristics. It is expressed as $\lambda_{zimm} \approx \frac{\mu_s R_g^3}{k_B T}$, where μ_s is the solution viscosity, k_B is the Boltzmann's constant, T is the absolute temperature, and R_g is the radius of the gyration of an entangled polymer chain. In this study, the R_g of HPC (Mw = 1,000,000) in the solution was approximately 124 ± 24 nm, which is much larger than that of the PEO (Mw = 2,000,000), *i.e.*, $R_g \sim 65$ nm.[14, 47, 53–56] Since the relaxation time of the diluted HPC solution is very small, it is difficult to measure it with a conventional capillary breakup extensional rheometer. Therefore, Zimm's theory for the estimation of the relaxation time was employed and the relaxation time was compared with that of the Carreau–Yasuda model (see **Table 5.1**). In the case of the diluted PEO solution, however, the relaxation time can be measured using a capillary breakup extensional rheometry. For the measurement, the HAKKE CaBER-1 device (Thermo Fisher Scientific Inc., U.S.A.) was used. The relaxation time of the diluted PEO solutions is listed in **Table 5.2**.[4] The relaxation time of both the diluted HPC and PEO solutions was used to calculate the elasticity number *El*. In viscoelastic fluids, the *El* is defined as *El = Wi / Re*, which is the ratio of the Weissenberg number ($Wi = N_1/\tau_{xy} = 2\mu\lambda\dot{\gamma}^2/\mu\dot{\gamma} = 2\lambda Q/HW^2$) to the Reynolds number ($Re = \rho U D_h/\mu$). Here, $D_h = 2WH/(W+H)$ is the hydraulic diameter

of the rectangular channel, μ is the solution viscosity, λ is the solution relaxation time, and Q is the flow rate.

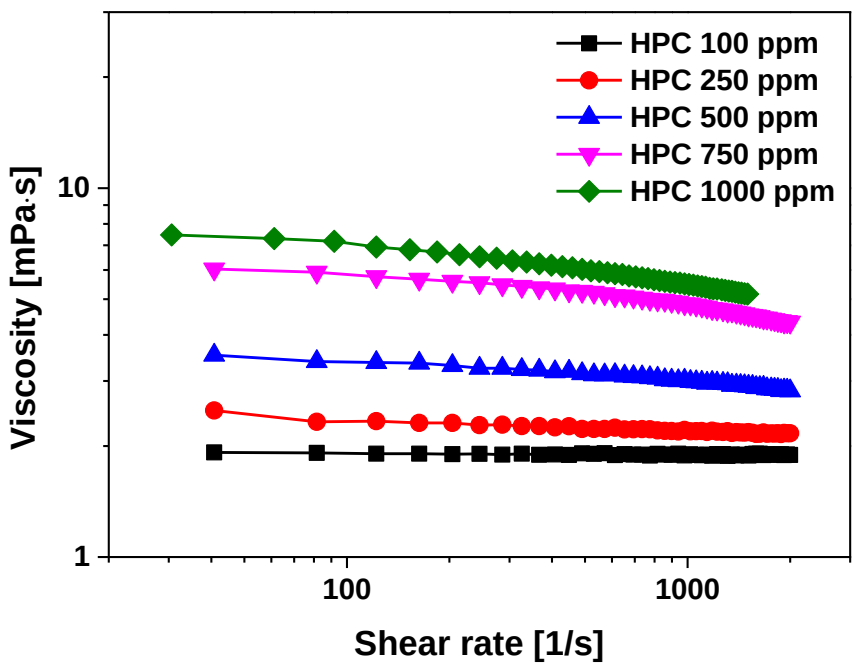

Figure 5.3. Viscosity of the HPC solutions according to the shear rates.

Table 5.1. Rheological properties of the HPC solutions fitted with the Carreau–Yasuda model and Zimm's theory.

Polymer Concentration [ppm]	Carreau-Yasuda Model		Zimm's Theory
	n	λ_{mean} [s]	λ_{mean} [s]
100	0.9864	0.00535	0.00879
250	0.9435	0.00857	0.01015
500	0.9232	0.00919	0.01386
750	0.9087	0.01218	0.02248
1000	0.8933	0.01754	0.02565

Table 5.2. Rheological properties of the PEO solutions fitted with the Carreau–Yasuda model and CaBER measurement.

Polymer Concentration [ppm]	Carreau-Yasuda model		CaBER
	n	λ_{mean} [s]	λ_{mean} [s]
500	0.9882	0.01404	0.015
1000	0.9556	0.01959	0.0184
1500	0.9302	0.01918	0.0198
2000	0.8921	0.02206	0.0217
2500	0.6841	0.02302	0.0232
3000	0.6113	0.02352	0.0243

5.3. Results and Discussion

5.3.1. Peculiar particle focusing in HPC solution

The particles in the viscoelastic fluid under the confined Poiseuille flow were placed at the center and the four corners of the cross-section of the microchannel as a result of the balance between the elastic and inertial forces. In many cases, diluted PEO and poly(vinyl-pyrrolidone) (PVP) solutions with the positive N_1 are used for viscoelasticity-induced particle focusing. The N_1 is considered as a main factor for the particle migration induced by the elastic force $F_E \sim a^3 \nabla N_1$. It is usually assumed that the N_1 is positive since τ_{xx} is much larger than τ_{yy} for common polymer solutions. Thus far, viscoelasticity induced particle focusing in a microfluidic device has been explained using the N_1, but the underlying physics has yet to be understood. For instance, while each normal stress component in the viscoelastic flow plays a key role in determining the particle movement in the channel, the effect of the normal stress component has not been addressed. In this sense, this study investigates how each normal stress component affects the particle focusing based on a force balance principle. It is surprising that polymer solutions with the negative N_1 show unexpected behaviors such as material contraction upon the confinement release.[38–40] The diluted HPC solutions with the negative N_1 were used to understand the influence of the normal-stress components, τ_{xx} and τ_{yy}, on the particle-focusing behaviors. Interestingly, unusual particle-focusing behaviors were observed in the diluted HPC solutions, as can be seen in **Figure 5.4**.

In the experiment, the particles suspended in the Newtonian fluid, the diluted PEO solution, and the diluted HPC solution were supplied randomly into the microfluidic inlet channel. Upon the occurrence of the flow with a large inertia (*Re* ~ 18.506), the particles in the Newtonian fluid were randomly distributed throughout the channel. The particles in the 2000 ppm PEO solution showed the center-line particle focusing in the channel, which has been reported in the literature.[2, 3, 11, 13, 33] For the 100 ppm HPC solution, the particles were focused at the double-equilibrium positions close to the channel walls. This is a very unexpected and unique phenomenon which is caused by viscoelasticity rather than channel geometry. The diluted HPC and PEO solutions with various concentrations were prepared,

and the N_1 and the first normal stress coefficient $\Psi_1 = (\tau_{xx} - \tau_{yy})/\dot{\gamma}^2$ were measured to explore the effect of the fluid elasticity on the particle-migration mechanism, as shown in **Figure 5.5 (a)** and **5.5 (b)**. The diluted PEO and HPC solutions showed the positive and negative Ψ_1, respectively. The magnitude of the negative N_1 value for the HPC solution was increased with increase in the polymer concentrations, which means that the τ_{yy} is larger than the τ_{xx} in all the cases. Indeed, this finding enabled us to look into the mechanism of particle migration from a different perspective.

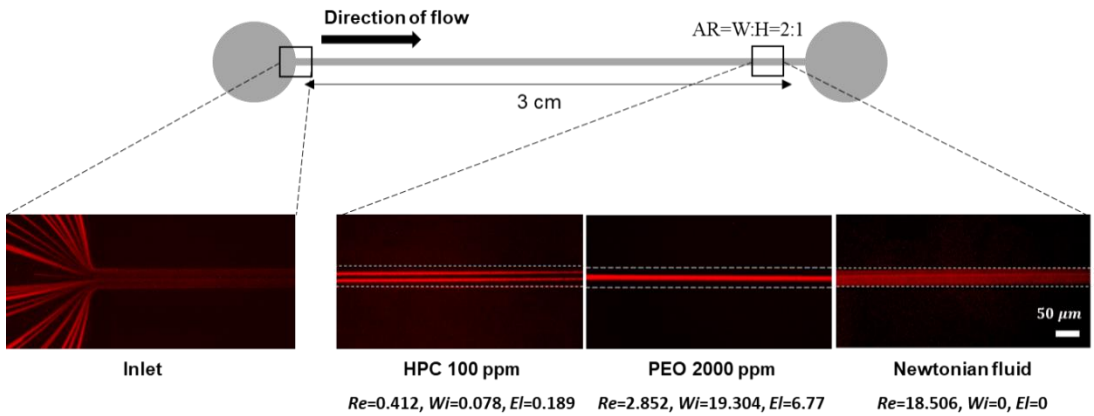

Figure 5.4. Particle focusing in viscoelastic solutions. Particle focusing behavior in the straight channel. The particles are double-line focused in the HPC solution with a negative N_1, whereas typical single-line focusing is observed in the PEO solution with a positive N_1. The particles in the Newtonian fluid are randomly distributed.

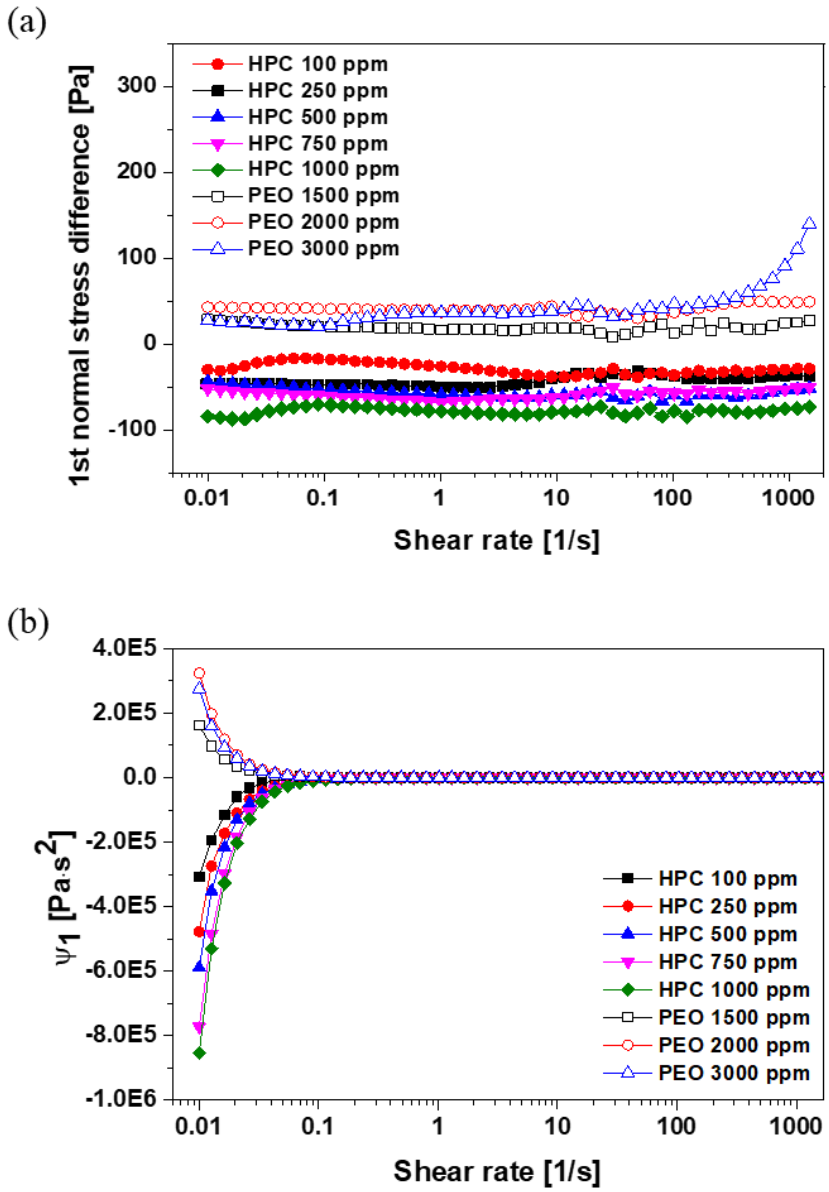

Figure 5.5. Rheological properties of viscoelastic solutions. (a) First normal stress difference as a function of the shear rate. The Measurement of N_1 is conducted changing the concentration of the HPC and PEO solutions. (b) First normal stress coefficient with respect to the shear rate.

5.3.2. Discussion for focusing mechanism

The difference of particle focusing in PEO and HPC solutions is categorized into two major behaviors. First, the double line particle focusing is observed in HPC solutions although the particle suspension flows in a straight microchannel.

In general, the suspended particles are aligned at the centerline of the straight rectangular microchannel along the flow direction as shown in case of PEO solution. Second, the focusing locations are not influenced by the flow rate increase in HPC solutions while the focusing position is varied when PEO solution is injected into a high aspect ratio (2:1) straight channel. As shown in **Figure 5.6 (a)**, the particles suspended in 100 ppm HPC solution are double aligned near the channel walls without the change of focusing locations according to the increase of the flow rate from 0.1 ml/h to 2.5 ml/h. However, the concentrated particles at the channel center are unstably separated into two different focusing lines when the flow rate increases to 0.5 ml/h from 0.1 ml/h in PEO solutions (**Figure 5.6 (b)**). We tried to explore the mechanism causing these two obvious differences of the focusing behavior.

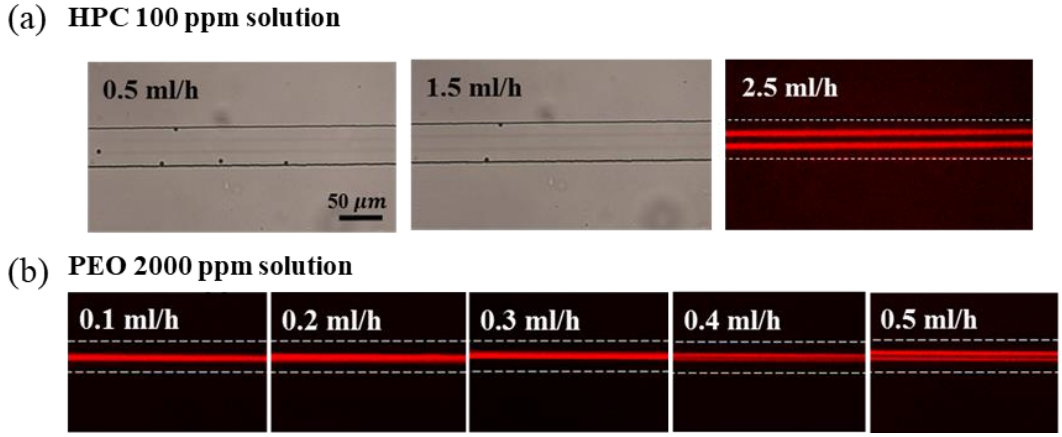

Figure 5.6. Flow rate effect for particle focusing location (a) in 100 ppm HPC solution, and (b) in 2000 ppm PEO solution.

5.3.2.1. Shear-thinning effect

Both the polyethylene oxide (PEO) solution and the hydroxypropyl cellulose (HPC) solution are viscoelastic solutions which show shear-thinning behavior. In the shear-thinning fluids, the particles migrate towards the off-centered region in a confinement due to the wall-attraction. As the shear rate increases, meaning the flow rate increases, the viscosity of the strong shear-thinning fluid gradually decreases, which follows that the inertial effect becomes effective to particle migration. For the comparison of the shear-thinning order of two solutions, viscosities of the solutions were curve-fitting with the relation of Carreau-Yasuda model ($\eta - \eta_\infty = \frac{\eta_0 - \eta_\infty}{(1+|\lambda\dot{\gamma}|^a)^{(1-n)/a}}$) as shown **Table 5.1** and **Table 5.2**, where η_∞ is infinite viscosity, η_0 is zero-shear viscosity and $\dot{\gamma}$ is the shear rate. Here, n indicates the power-law index. For the viscoelastic fluids, the power law index n is lower than 1 and the smaller the n, the greater the shear-thinning. 1000 ppm HPC solution and 2000 ppm PEO solution have similar value of the power-law index about 0.89 while the double line particle focusing is observed in 1000 ppm HPC solution and the particle migrate at the channel center as a single line in PEO solution. Therefore, the peculiar focusing behavior of HPC solutions is not about the shear-thinning effect.

5.3.2.2. Molecular structure effect

The two polymers (PEO and HPC) are semiflexible and water-soluble polymer which have been widely studied in polymer science. Also, HPC with low molecular weight has been reported the liquid-crystalline behavior when it flows in a confinement.[44–47] The rod-like structured molecules can be oriented along the flow direction in a high shear condition. Although we selected high molecular weight HPC powder to exclude the liquid-crystalline behavior, it was not easy to conclude that the molecular orientation is not occurred in the flow. In order to verify the semiflexible molecular movement in the microchannel flow, the heterogeneity of the solutions was confirmed by Cole-Cole plot (**Figure 5.7**). Cole-Cole plot is defined by a logarithmic plot of the storage modulus versus the loss modulus and a slope of 2 indicates the homogeneous solution without any physical structure. When the

slope is close to 0, it means that the solution is heterogeneous with rod-like molecules which can align to the flow direction. For the seamless experiment, PEO and HPC solutions with high polymer concentration from 4000 to 10000 ppm were prepared. As a result, two kinds of the solution have similar slope value which is close to 2, therefore, the liquid-crystalline molecular behavior in HPC solution is not considerable in this study.

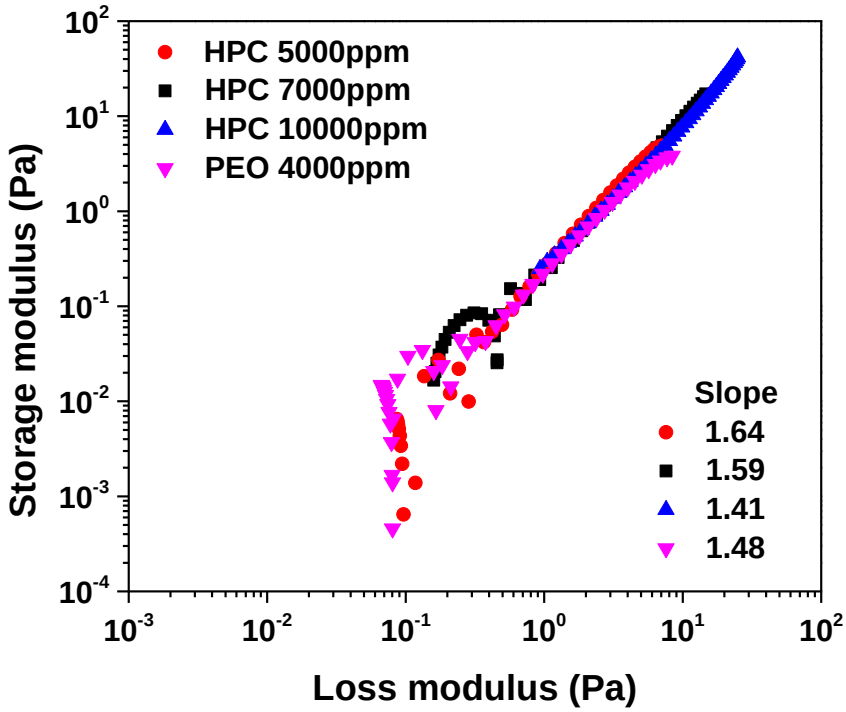

Figure 5.7. Cole-Cole plot for evaluation of solution homogeneity.

5.3.2.3. Normal stress component effect

Since the sign of the first normal stress difference (N_1) of two solutions is different, we thought that the magnitude of the normal stress component has the difference. By using a bulk rheometer, the N_1 and the difference between the first and second normal stress differences were obtained to experimentally calculate the normal stress component τ_{yy}. The cone and plate and parallel plates were selected for the experiments. First, N_1 was obtained from the cone and plate experiment.

The normal force F_N acting on the upper cone was measured as follows.

$$F_N = \frac{\pi R^2}{2}\left[\sigma_{xx} - \sigma_{yy}\right] = \frac{\pi R^2}{2} N_1 \tag{5-1}$$

In addition, the difference between the first and second normal stress differences was obtained by measuring the normal force with a parallel plate geometry (**Figure 5.8 (a)**).

$$\Delta N = N_1 - N_2 = \tau_{xx} - 2\tau_{yy} + \tau_{zz} = \frac{2F}{\pi R^2}\left[1 + \frac{d\ln F}{2d\ln\Omega}\right] \tag{5-2}$$

, where N_2 is the second normal-stress difference, *R* is the radius of the parallel plate, and Ω is the angular velocity,[50, 51] and τ_{yy} is the normal stress in the transverse direction to the shear-flow direction, i.e., the velocity-gradient direction.[52–54] The measurement of τ_{xx} is extremely difficult, whereas τ_{yy} can be evaluated by using the ΔN data as below. The total stress tensor of a fluid, σ_{ij}, is composed of the normal stress components σ_{ii} ($\mathrm{i} = 1, 2, 3$) and the shear stress components σ_{ij} ($\mathrm{i, j} = 1, 2, 3; \mathrm{i} \neq \mathrm{j}$). For an incompressible and linear viscoelastic fluid, the hydrostatic pressure p is defined as $p = (1/3)\left(\sigma_{xx} + \sigma_{yy} + \sigma_{zz}\right)$, and a deviatoric stress tensor τ_{ij} is defined as $\tau_{ij} = \sigma_{ij} - p\delta_{ij}$, where δ_{ij} is the Kronecker delta.[54] From these relations, the summation of the deviatoric normal stress components becomes

$$\tau_{xx} + \tau_{yy} + \tau_{zz} \approx 0. \tag{5-3}$$

By subtracting Equation (5-2) from Equation (5-3), the normal-stress component τ_{yy} is approximated by

$$\tau_{yy} \sim -\frac{N_1 - N_2}{3}. \quad (5\text{-}4)$$

In our microfluidic system, the velocity gradient direction was defined as the direction along the channel width. The deviatoric stresses, τ_{yy}'s of the diluted PEO and HPC solutions were obtained by using Equation (5-4) (**Figure 5.8(b)**). The incompressible nonlinear viscoelastic fluids are often explained by the Oldroyd-B model due to its simplicity. Equation (5-3) is true for incompressible Newtonian and linear viscoelastic fluids.[50–52] When the fluid becomes highly nonlinear, Equation (5-3) becomes invalid due to the anisotropic stress conditions. Here, we assume that the diluted HPC and PEO solutions are linear viscoelastic which allows one to use Equation (5-3), and can simplify $\tau_{yy} \sim (N_1 - N_2)/3$. Since measuring τ_{yy} is impossible, we measured N_1 and $(N_1 - N_2)$ of the diluted polymer solutions, and then extracted the τ_{yy} values of the diluted HPC and PEO solutions.

The τ_{yy} was increased with increase in the shear rate, and the HPC solutions showed higher τ_{yy} than the PEO solutions. As the solution concentrations were increased, the τ_{yy} for the HPC solutions was increased. This was an anomalous behavior considering typical polymer solutions including the PEO solution. From this finding, it was presumed that the particle-focusing behavior in the viscoelastic fluid is not determined by the normal stress differences but each normal stress itself. In other words, the double-line particle focusing can be explained by considering all the normal stresses such as τ_{xx} and τ_{yy} acting on the particle.

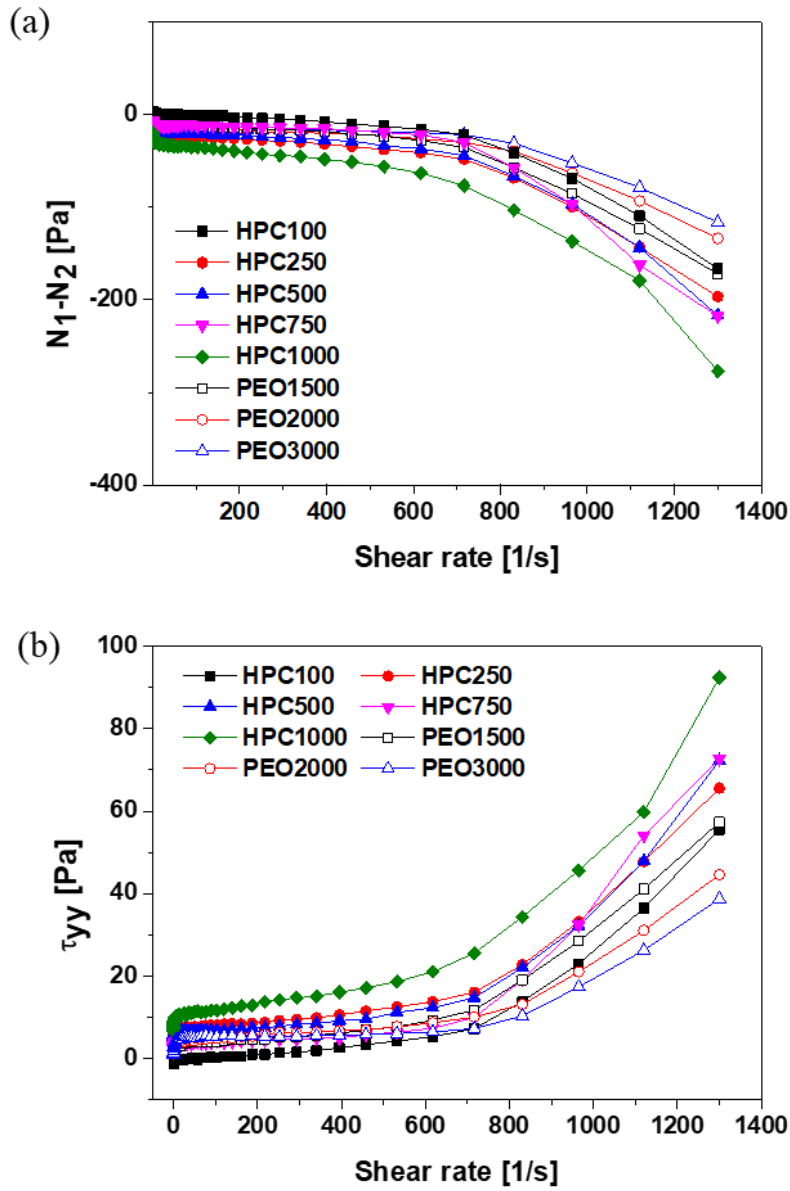

Figure 5.8. Rheological characteristics of the HPC and PEO solutions. (a) $N_1 - N_2$ as a function of the shear rate. The measurement is carried out changing the concentration of the solutions. (b) τ_{yy} as a function of the shear rate. The HPC solutions show much higher τ_{yy} than the PEO solutions.

5.3.3. Particle size and polymer concentration effect

The viscoelasticity-induced particle focusing was analyzed by using particles with different diameters of 5, 10, and 15 μm in the diluted HPC solutions (**Figure 5.9**). The channel-blockage ratio ($\beta = a/H$) is a critical factor for the particle-focusing behavior in viscoelastic fluids. The critical value of β was 0.2 according to the literature. The particles with $\beta \geq 0.2$ in the diluted PEO solutions were focused at the center, whereas the particles with $\beta < 0.2$ moved downstream randomly.[9] This technique was used to achieve size-selective particle separations.[9, 14, 22, 24] In the diluted HPC solutions, the particle motion was different from that in the diluted PEO solutions as shown in **Figure 5.9**. In the figure, one hundred images were superimposed for better observation of the lateral migration of the particles in the 100, 500, and 1000 ppm HPC solutions as shown in **Figure 5.9**. The 5, 10, and 15 μm particles in the diluted 100 ppm HPC solutions showed the double-line particle focusing even at low *El* values. It turned out that the double-line particle-focusing behavior in the HPC solutions strongly depended on the polymer concentration. When the concentration of the HPC solutions is 100 ppm, the double-line particle focusing is clearly detected for all the particles. For the 5 μm particles, the distance between the two focusing lines was relatively short, and the particles tended to move toward the channel center as the concentration of the HPC solution was increased from 100 to 1000 ppm (**Figure 5.10 (a)**). For the particles of 10 and 15 μm diameter, the double-line focusing was generated close to the side walls of the channel regardless of the HPC concentration. That is, the small particles were focused at the center, while the large particles were double-line focused close to the walls, which is completely different from other results reported in the literature. This is the first study which reports the double line particle focusing phenomenon solely induced by applying the force balance principle onto particles that are suspended in a viscoelastic fluid in the microfluidic channel.

To demonstrate the particle-sorting efficiency, the particle-separation resolution $R_{ij} = \Delta x_{ij}/(s_i + s_j)$ was calculated with respect to the particle size and the elasticity number, where Δx_{ij} is the distance between the *i*-th and *j*-th particles, and s_i is the standard deviation of the *i*-th particle's location.[14] The particle-separation resolution showed the highest values at the 1000 ppm HPC solution using the 5 and 10 μm particles

and at the 2000 ppm HPC solution using the 10 and 15 μm particles as displayed in **Figure 5.10 (b)**. These unusual particle-focusing behaviors can be used to develop an efficient particle sorter without employing any complex geometry.

From these experimental results, it was found that the large particles were more largely affected by τ_{yy} than the small particles, resulting in the close-wall double-line particle focusing. On the other hand, the small particles were focused at the center. The experimental observation can be explained with the help of the following assumption: the particle focusing is determined by the normal stress components themselves but not their differences. That is, when $N_1 < 0$ at high *El* values, the larger particles are focused along double lines close to the side wall than the smaller particles. For the viscoelastic fluids with $N_1 > 0$, all the particles, however, are focused at the center because $\tau_{xx} \gg \tau_{yy}$ (**Figure 5.11**).

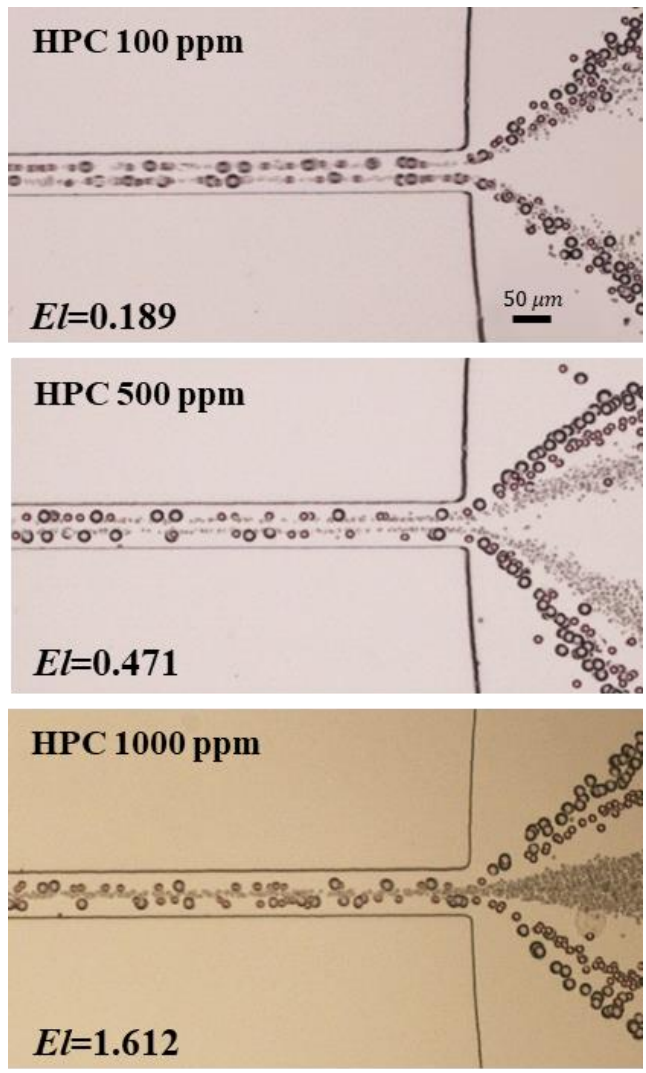

Figure 5.9. Particle focusing behavior in the HPC solutions with a negative N_1. Microscopic images of the particle focusing in the channel. The reverse particle focusing phenomenon is observed. At the relatively low polymer concentration, all the particles are double-line focused close to the channel walls. However, as the polymer concentration is increased, the large particles are double-line focused, but the small particles are focused at the center. Hundreds of images are superimposed for an enhanced observation of the particle migration.

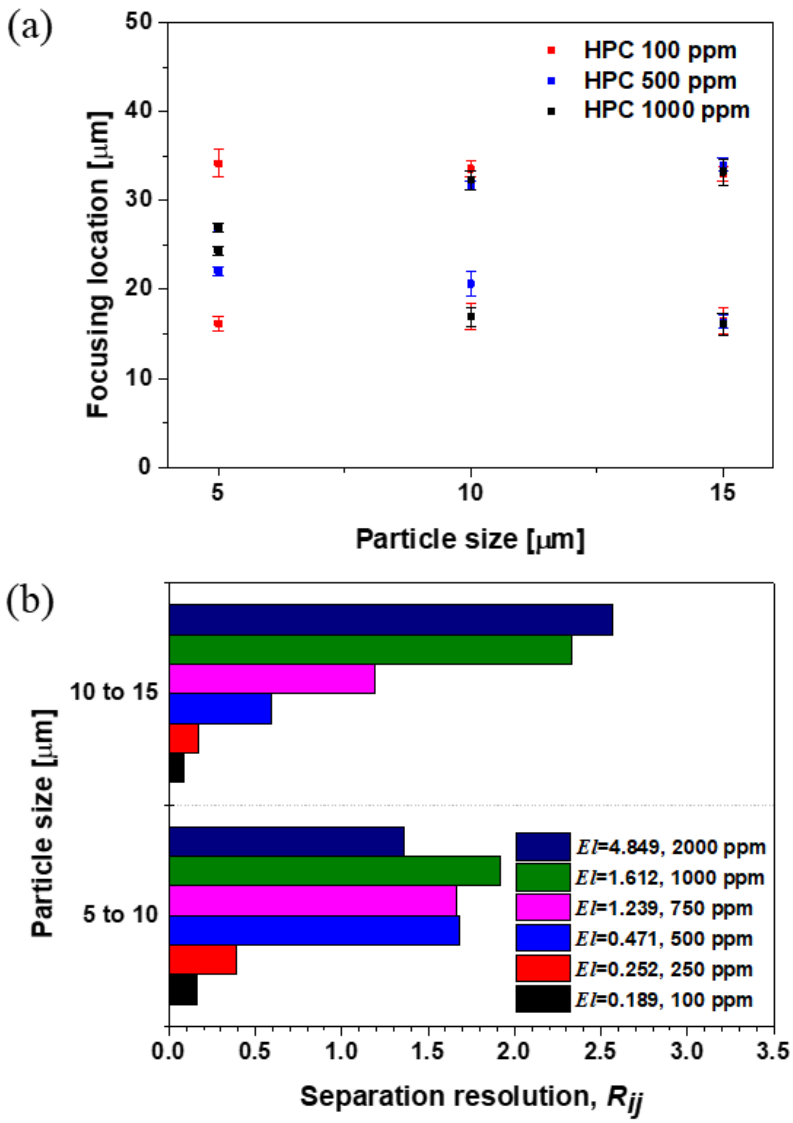

Figure 5.10. Particle focusing behavior in HPC solutions. (a) Particle focusing location according to the polymer concentration and the particle size and (b) Particle-separation resolutions (R_{ij}) with respect to various polymer concentrations. $R_{ij} = \Delta x_{ij}/(s_i + s_j)$, where Δx_{ij} is the distance between the i-th and j-th particles, and s_i is the standard deviation of the i-th particle's location.

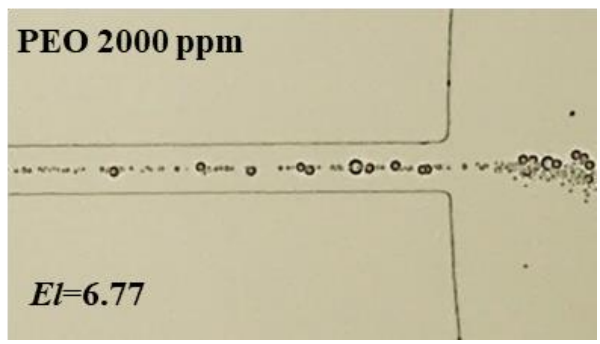

Figure 5.11. Typical particle focusing behavior in the PEO solution. All of the particles with 5, 10, and 15 μm diameters are focused at the center.

5.3.4. Mechanism & Dimensionless number based on the normal stress

Based on the experimental results, mechanisms of the particle focusing in viscoelastic fluids with the positive and negative N_1 were suggested in this study (**Figure 5.12**). The inertial forces including the shear-gradient lift force ($F_{L.S}$) and wall-repulsion force ($F_{L.W}$) and the elastic force (F_E) are developed in the microfluidic channel. In many cases, the inertial forces are negligible due to a low *Re*. In **Figure 5.12**, the elastic forces developed by τ_{xx} and τ_{yy} are expressed as $F_{E,\tau_{xx}}$ and $F_{E,\tau_{yy}}$, respectively. For typical viscoelastic fluids, the shear stress (τ_{xy}) and the normal stress (τ_{xx}), which are functions of the shear rate, become stronger at the channel walls than the channel center (**Figure 5.12**). The strong formation of the τ_{xx} and τ_{xy} at the channel walls causes the lateral particle migration towards the centerline. In many polymer solutions such as the diluted PEO solution, the τ_{yy} is relatively small (*i.e.*, negligible $F_{E,\tau_{yy}}$). Hence, the only driving force for the lateral particle migration is the τ_{xx} and τ_{xy}, which results in the particle focusing at the center (**Figure 5.12 (a)**). However, since the diluted HPC solution has a remarkably large $F_{E,\tau_{yy}}$, the particle movement is affected by not only the τ_{xx} and τ_{xy} but also the τ_{yy} (**Figure 5.12 (b)**). Consequently, the particles are double-line focused close to the channel walls when $F_{E,\tau_{yy}}$ is larger than $F_{E,\tau_{xx}} + F_v$. Here, F_v is the viscous drag force that resists the lateral migration of particles. For better understanding of the mechanism, a dimensionless parameter was defined and used, which can explain the ratio between the normal and the drag forces. The F_v leading to the particle for the lateral particle migration is a function of the particle diameter a, the fluid velocity U, the fluid density ρ, and the fluid viscosity μ.

As a result of the dimensional analysis based on Buckingham π-theorem, the dimensionless number $\frac{\rho a^2 \tau_{yy}}{\mu^2}$ was introduced, which represents the ratio of the elastic force to the F_v. In our study, it is intended to illustrate the hydrodynamic situations occurred on the particle (**Figure 5.12**) and to use τ_{yy} to obtain the scaling law that is derived by dimensional analysis. The normal stress gradient, $\nabla\tau_{yy}$, acting on the particle induced the lateral particle migration, however, τ_{yy} pushing the particle downward is assumed to be physically negligible due to its small value so that τ_{yy} is used to represent the

dimensionless number $\frac{\rho a^2 \tau_{yy}}{\mu^2}$ by balancing the elastic force and the viscous force. It was shown in **Figure 5.13 (a)** that the $\frac{\rho a^2 \tau_{yy}}{\mu^2}$ of the diluted HPC solutions decreased with increase in the polymer concentration and decreasing the particle size. However, it was found that the diluted PEO solution has a very low value of $\frac{\rho a^2 \tau_{yy}}{\mu^2}$ regardless of the polymer concentration and the particle size. These results implied that the suspended particles in the diluted HPC solution were subject to the larger normal force than the viscous drag force, thus resulting in the particle migration. On the other hand, the effect of the particle size on the normal force τ_{yy} for the lateral particle migration is not meaningful in the diluted PEO solutions, which leads to the center-focusing of particles rather than the off-center focusing. This coincides with the particle-focusing results of **Figure 5.13 (b)**.

The large particles in the HPC solution were double-line focused in all the cases, while the small particles were either focused at the center or off-center depending on the value of $\frac{\rho a^2 \tau_{yy}}{\mu^2}$. In general, the Weissenberg number, $Wi = \frac{N_1}{\tau_{xy}} = \frac{(\tau_{xx} - \tau_{yy})}{\mu\dot{\gamma}}$, is useful to explain the particle focusing in viscoelastic fluids. In the case where τ_{xx} is dominant, *e.g.*, the PEO solution with the positive N_1, the particles can be focused at the center. When the contribution of τ_{yy} becomes more significant for the particle migration than $\tau_{xx} - \tau_{yy}$, as in the case of the HPC solution, the particle-focusing regimes between the single-line and the double-line particle focusing could be distinguished by the ratio of τ_{yy} to $\tau_{xy}(= \mu\dot{\gamma})$ as demonstrated in **Figure 5.14**.

In the regime with a relatively low value of τ_{yy}/τ_{xy}, all of the 5, 10, and 15 μm particles in the PEO solution were focused at the center. The particles in the HPC solutions were double-line separated in the range of $10 < \tau_{yy}/\tau_{xy} < 20$, and become double-line focused when $\tau_{yy}/\tau_{xy} > 20$. These results indicate that the ratio τ_{yy}/τ_{xy} proposed in this study can serve as an effective indicator to understand the reversed particle-focusing phenomenon.

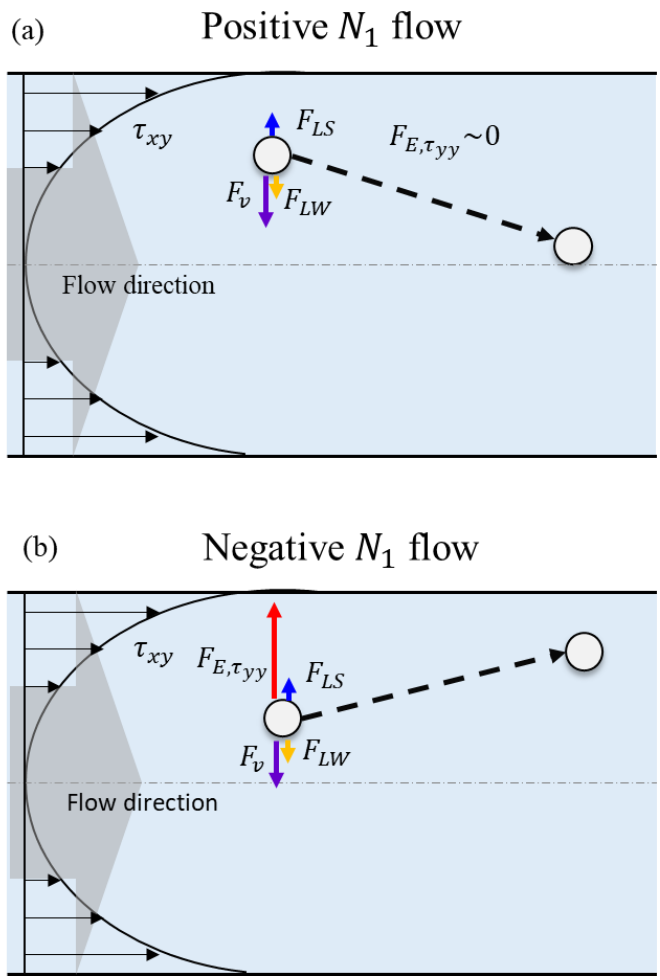

Figure 5.12. Schematic illustration of focusing mechanism of a particle in viscoelastic fluids. (a) Particle behavior in the positive N_1 flow. The particle is focused at the center when the τ_{yy} is negligible. (b) Particle behavior in the negative N_1 flow. The particle is double-line focused close to the wall when the $F_{E,\tau_{yy}}$ outweighs the $F_{\tau_{xy}}+F_{E,\tau_{xx}}$. Here $F_{E,\tau_{xx}}$ and $F_{E,\tau_{yy}}$ are the elastic forces from τ_{xx} and τ_{yy}, respectively, and F_v is viscous force from τ_{xy}.

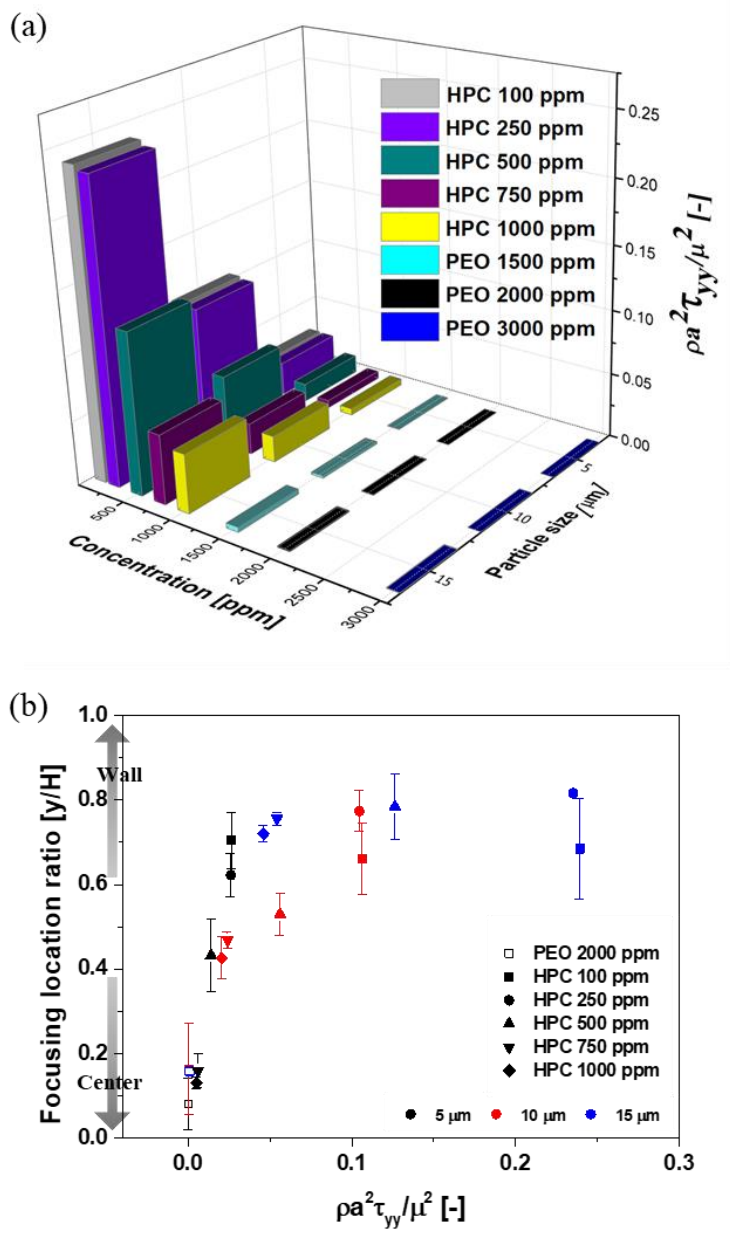

Figure 5.13. Focusing mechanism of particles induced by τ_{yy}. (a) Dimensionless number, $\rho a^2 \tau_{yy}/\mu^2$ as a function of the concentration and the particle size. The dimensionless number is defined to figure out the effect of the ratio of the viscous drag force to the normal force τ_{yy}, on the particle migration. (b) Focusing location ratio as a function of the number.

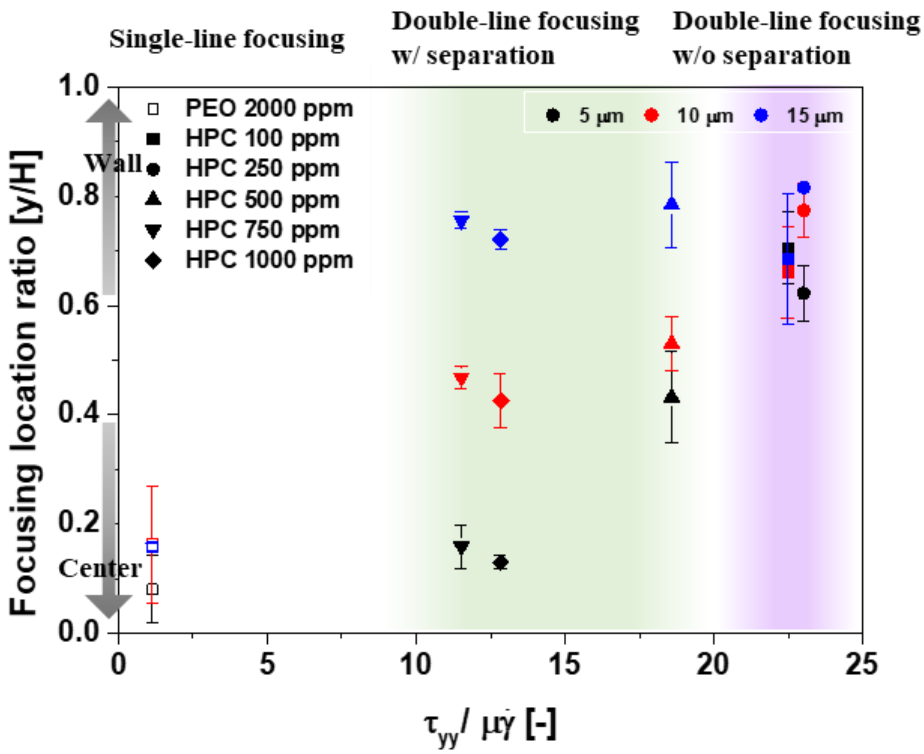

Figure 5.14. Single-line and double-line particle-focusing regimes classified according to the $\tau_{yy}/\mu\dot{\gamma}$.

5.4. Summary

In this study, we investigated the lateral particle migration in viscoelastic fluids with the positive or negative N_1. The corresponding particle focusing mechanism was analyzed changing the polymer concentration and the particle size. The findings showed that the migration of particles in the microfluidic channel could be explained by considering all the stress components separately (*i.e.*, τ_{xx}, τ_{yy} and τ_{xy} in the 2D case) rather than the only normal stress differences. The viscoelastic solution with the negative N_1 showed the reversed particle-focusing phenomenon compared with those with the positive N_1, which indicated that τ_{yy} plays a significant role in the particle migration. A dimensionless parameter defined with the ratio of the normal force to the viscous drag force was used to demonstrate the reversed particle focusing phenomenon. The ratio τ_{yy}/τ_{xy} was employed to divide the reversed particle-focusing regimes. Overall, it is anticipated that the reverse particle-focusing based on the negative normal stress difference could be applied to a new type of the flow cytometry which is able to separate and focus particles with different sizes in a viscoelastic fluid.

5.5. References

1. Howard, M. P., Panagiotopoulos, A. Z. & Nikoubashman, A. Inertial and viscoelastic forces on rigid colloids in microfluidic channels. *J. Chem. Phys.* **142,** (2015).
2. D'Avino, G. *et al.* Single line particle focusing induced by viscoelasticity of the suspending liquid: theory, experiments and simulations to design a micropipe flow-focuser. *Lab Chip* **12,** 1638 (2012).
3. Del Giudice, F. *et al.* Particle alignment in a viscoelastic liquid flowing in a square-shaped microchannel. *Lab Chip* **13,** 4263–71 (2013).
4. Yang, S. H., Lee, D. J., Youn, J. R. & Song, Y. S. Multiple-Line Particle Focusing under Viscoelastic Flow in a Microfluidic Device. *Anal. Chem.* **89,** 3639–3647 (2017).
5. Romeo, G., D'Avino, G., Greco, F., Netti, P. a & Maffettone, P. L. Viscoelastic flow-focusing in microchannels: scaling properties of the particle radial distributions. *Lab Chip* **13,** 2802 (2013).
6. Kim, B. & Kim, J. M. Elasto-inertial particle focusing under the viscoelastic flow of DNA solution in a square channel. *Biomicrofluidics* **10,** (2016).
7. Yuan, D. *et al.* Dean-flow-coupled elasto-inertial three-dimensional particle focusing under viscoelastic flow in a straight channel with asymmetrical expansion-contraction cavity arrays. *Biomicrofluidics* **9,** (2015).
8. Lee, D. J., Brenner, H., Youn, J. R. & Song, Y. S. Multiplex particle focusing via hydrodynamic force in viscoelastic fluids. *Sci. Rep.* **3,** 3258 (2013).
9. Lim, H., Nam, J. & Shin, S. Lateral migration of particles suspended in viscoelastic fluids in a microchannel flow. *Microfluid. Nanofluidics* **17,** 683–692 (2014).
10. Ahn, S. W., Lee, S. S., Lee, S. J. & Kim, J. M. Microfluidic particle separator utilizing sheathless elasto-inertial focusing. *Chem. Eng. Sci.* **126,** 237–243 (2015).
11. Del Giudice, F., D'Avino, G., Greco, F., Netti, P. a. & Maffettone, P. L. Effect of fluid rheology on particle migration in a square-shaped microchannel. *Microfluid. Nanofluidics* **19,** 95–104 (2015).
12. Lim, E. J. *et al.* Inertio-elastic focusing of bioparticles in microchannels at high

throughput. *Nat. Commun.* **5,** 4120 (2014).

13. Yang, S., Kim, J. Y., Lee, S. J., Lee, S. S. & Kim, J. M. Sheathless elasto-inertial particle focusing and continuous separation in a straight rectangular microchannel. *Lab Chip* **11,** 266–273 (2011).
14. Kang, K., Lee, S. S., Hyun, K., Lee, S. J. & Kim, J. M. DNA-based highly tunable particle focuser. *Nat. Commun.* **4,** 2567 (2013).
15. Leshansky, A. M., Bransky, A., Korin, N. & Dinnar, U. Tunable nonlinear viscoelastic 'focusing' in a microfluidic device. *Phys. Rev. Lett.* **98,** (2007).
16. HUANG, P. Y., FENG, J., HU, H. H. & JOSEPH, D. D. Direct simulation of the motion of solid particles in Couette and Poiseuille flows of viscoelastic fluids. *J. Fluid Mech.* **343,** S0022112097005764 (1997).
17. Kang, A. R. *et al.* Medium viscoelastic effect on particle segregation in concentrated suspensions under rectangular microchannel flows. *Korea Aust. Rheol. J.* **23,** 247–254 (2011).
18. Young Kim, J., Won Ahn, S., Sik Lee, S. & Min Kim, J. Lateral migration and focusing of colloidal particles and DNA molecules under viscoelastic flow. *Lab Chip* **12,** 2807 (2012).
19. Cartas-Ayala, M. A., Raafat, M. & Karnik, R. Self-sorting of deformable particles in an asynchronous logic microfluidic circuit. *Small* **9,** 375–381 (2013).
20. Guan, G. *et al.* Spiral microchannel with rectangular and trapezoidal cross-sections for size based particle separation. *Sci. Rep.* **3,** 1475 (2013).
21. Lu, X. & Xuan, X. Elasto-Inertial Pinched Flow Fractionation for Continuous Shape-Based Particle Separation. *Anal. Chem.* **87,** 11523–11530 (2015).
22. Li, D., Lu, X. & Xuan, X. Viscoelastic Separation of Particles by Size in Straight Rectangular Microchannels: A Parametric Study for a Refined Understanding. *Anal. Chem.* acs.analchem.6b03501 (2016). doi:10.1021/acs.analchem.6b03501
23. Liu, C., Xue, C. & Hu, G. Sheathless Separation of Particles and Cells by Viscoelastic Effects in Straight Rectangular Microchannels. *Procedia Eng.* **126,** 721–724 (2015).
24. Lu, X., Zhu, L., Hua, R. mao & Xuan, X. Continuous sheath-free separation of particles by shape in viscoelastic fluids. *Appl. Phys. Lett.* **107,** (2015).
25. Nam, J. *et al.* Hybrid capillary-inserted microfluidic device for sheathless particle

focusing and separation in viscoelastic flow. *Biomicrofluidics* **9,** 64117 (2015).

26. Yang, S. *et al.* Deformability-selective particle entrainment and separation in a rectangular microchannel using medium viscoelasticity. *Soft Matter* **8,** 5011 (2012).
27. H. Ranchon, R. Malbec, V. Picot, A. Boutonnet, P.Terrapanich, P. Joseph, T. Leïchlé, A. B. 2016 DNA separation and enrichment using electro-hydrodynamic bidirectional flows in viscoelastic liquids. *Lab Chip* 25 (2016). doi:10.1039/C5LC01465D
28. Li, G., McKinley, G. H. & Ardekani, A. M. Dynamics of particle migration in channel flow of viscoelastic fluids. *J. Fluid Mech.* **785,** 486–505 (2015).
29. Del Giudice, F. *et al.* Rheometry-on-a-chip: measuring the relaxation time of a viscoelastic liquid through particle migration in microchannel flows. *Lab Chip* **15,** 783–792 (2015).
30. Cha, S. *et al.* Cell stretching measurement utilizing viscoelastic particle focusing. *Anal. Chem.* **84,** 10471–10477 (2012).
31. Kim, J., Kim, J. Y., Kim, Y., Lee, S. J. & Kim, J. M. Shape Measurement of Ellipsoidal Particles in a Cross-Slot Microchannel Utilizing Viscoelastic Particle Focusing. *Anal. Chem.* **89,** 8662–8666 (2017).
32. Villone, M. M., D'Avino, G., Hulsen, M. A., Greco, F. & Maffettone, P. L. Particle motion in square channel flow of a viscoelastic liquid: Migration vs. secondary flows. *J. Nonnewton. Fluid Mech.* **195,** 1–8 (2013).
33. Barnes, H. A. An introduction to Rheology. *Elsevier* (1989).
34. Villone, M. M., D'Avino, G., Hulsen, M. A., Greco, F. & Maffettone, P. L. Simulations of viscoelasticity-induced focusing of particles in pressure-driven micro-slit flow. *J. Nonnewton. Fluid Mech.* **166,** 1396–1405 (2011).
35. Tian, F. *et al.* Microfluidic co-flow of Newtonian and viscoelastic fluids for high-resolution separation of microparticles. *Lab Chip* (2017). doi:10.1039/C7LC00671C
36. Kiss, G. & Porter, R. S. Rheology of concentrated solutions of helical polypeptides. *J. Polym. Sci. Polym. Phys. Ed.* **18,** 361–388 (1980).
37. Lin-Gibson, S., Pathak, J. A., Grulke, E. A., Wang, H. & Hobbie, E. K. Elastic Flow Instability in Nanotube Suspensions. *Phys. Rev. Lett.* **92,** 48302 (2004).
38. Kharchenko, S. B., Douglas, J. F., Obrzut, J., Grulke, E. A. & Migler, K. B. Flow-

induced properties of nanotube-filled polymer materials. *Nat. Mater.* **3,** 564–568 (2004).

39. Pasquali, M. Swell properties and swift processing. *Nat. Mater.* **3,** 509–510 (2004).
40. Janmey, P. A. *et al.* Negative normal stress in semiflexible biopolymer gels. *Nat. Mater.* **6,** 48–51 (2007).
41. Fried, F., Leal, C. R., Godinho, M. H. & Martins, A. F. The first normal stress difference and viscosity in shear of liquid crystalline solutions of hydroxypropylcellulose: new experimental data and theory. *Polym. Adv. Technol.* **5,** 596–599 (1994).
42. Hoekstra, H., Vermant, J., Mewis, J. & Narayanan, T. Rheology and structure of suspensions in liquid crystalline hydroxypropylcellulose solutions. *Langmuir* **18,** 5695–5703 (2002).
43. Martins, A. F., Leal, C. R., Godinho, M. H. & Fried, F. The influence of polymer molecular weight on the first normal-stress difference and shear-viscosity of LC solutions of hydroxypropylcellulose. *Mol. Cryst. Liq. Cryst.* **362,** 305–312 (2001).
44. Kulichikhin, V. G., Makarova, V. V, Tolstykh, M. Y., Picken, S. J. & Mendes, E. Structural evolution of liquid-crystalline solutions of hydroxypropyl cellulose and hydroxypropyl cellulose-based nanocomposites during flow. *Polym. Sci. Ser. A* **53,** 748–764 (2011).
45. Phillies, G. D. J., O'Connell, R., Whitford, P. & Streletzky, K. A. Mode structure of diffusive transport in hydroxypropylcellulose: Water. *J. Chem. Phys.* **119,** 9903–9913 (2003).
46. Hongladarom, K., Secakusuma, V. & Burghardt, W. R. Relation between molecular orientation and rheology in lyotropic hydroxypropylcellulose solutions. *J. Rheol. (N. Y. N. Y).* **38,** 1505–1523 (1994).
47. Magda, J. J. Hongladarom and. 772–784 (1993).
48. Acad, J. E. A. N. Y. Optical Properties of Hydroxypropycellulose. *Macromolecules* **17,** 1512–1520 (1984).
49. Eom, Y., Jung, D., Hwang, S. S. & Kim, B. Characteristic dynamic rheological responses of nematic poly(p-phenylene terephthalamide) and cholesteric hydroxypropyl cellulose phases. *Polym. J.* **48,** 869–874 (2016).
50. Korneeva, E. V *et al.* Conformational Properties of Hydroxypropylcellulose !.

Hydrodynamic Properties and Equilibrium Rigidity of its Macromolecules. *Eur. Polym. J.* **26,** 781–785 (1990).

51. Procedures, E. Conformational properties of hydroxypropylcellulose--ii. flow birefringence and optical anisotropy of hydroxypropylcellulose macromolecules. **26,** 787–790 (1990).
52. Morrison, F. a. Understanding Rheology. *Oxford Univ. Press* 387–394 (2001). doi:10.3933/ApplRheol-12-233
53. Shaw, M. T. & MacKnight, W. J. *Introduction to Polymer Viscoelasticity: Third Edition*. *Introduction to Polymer Viscoelasticity: Third Edition* (2005). doi:10.1002/0471741833
54. Miller, M. J. & Christiansen, E. B. The stress state of elastic fluids in viscometric flow. *AIChE J.* **18,** 600–608 (1972).

Chapter V.

Concluding Remarks

The present work was aimed to explore a new particle focusing mechanism and develop a novel analytical platform integrating binary logic operations. Based on force balance of inertial forces and elastic force under viscoelastic fluid flow, multiple particle focusing locations were observed and controlled. Furthermore, a particle logic device was introduced by using multiple-line particle focusing phenomenon. These accomplishments were experimentally demonstrated with microparticles in a microfluidic channel, proving by theoretical analyses from several perspectives such as flow, structural analysis and heat transfer.

The multiple-line particle focusing was observed in two kinds of viscoelastic fluids having the opposite sign of the first normal stress difference (N_1) under shear flow. For the particle focusing in a microchannel, the positive first normal stress difference fluids (*e.g.,* polyethylene oxide (PEO), polyvinyl pyrrolidone (PVP) solutions) have been used and it has been reported that the particles migrate towards the channel center which is the stable region by the force balance of inertial force and elastic force. The elastic force is proportional to the gradient of the N_1 and the channel center has the minimum values of the N_1. Contrary to the focusing behavior in the positive N_1 fluids, the particles are double aligned in the negative N_1 fluid, hydroxypropyl cellulose (HPC) solutions. As the particle size increases, the particles are focused near the channel walls and the distance between the focusing lines increases, while all sizes of the particles are aligned at the channel center as a single line in the positive N_1 solutions. We analyzed the focusing mechanism in terms of the N_1 and the normal stress component effect acting on a particle. The finding showed that the migration of particles in the microfluidic channel could be explained by considering the normal stress components separately rather than the only N_1. For the simple analysis of the normal stress component effect, the solutions were assumed as a linear viscoelastic fluid and the normal stress τ_{yy} which plays a significant role in the particle migration was finally calculated by experimental measurements. In order to

effectively describe the τ_{yy} effect on a particle, a new dimensionless parameter, the ratio of the normal force to the viscous drag force, was defined and schematic illustrations of the focusing mechanism by the normal force from τ_{yy} were suggested for the two different kinds of flow. Additionally, the ratio τ_{yy}/τ_{xy} was employed to divide the reversed particle focusing working regimes. The multiple-line particle focusing was also realized by developing the general viscoelastic focusing mechanism in the positive N_1 fluid. According to the viscoelastic particle focusing, the particles are typically focused at the channel center and four corners of a rectangular channel by the force balance. The relative magnitude of the elastic force and inertial forces can be altered by the channel cross-sectional aspect ratio and the channel inlet geometry. The higher cross-sectional aspect ratio channel has the wider stable region for the particles and the shear-gradient lift force at the center becomes high when the flows from the two inlet meet. The aspect ratio effect and the lift force were theoretically calculated by adopting Oldroyd-B model which is one of the representative model for viscoelastic fluids. Consequently, the particles are double or triple aligned by the effect of the shear gradient lift force and wall-repulsion force at the entrance and the bigger particles are aligned closer to the channel walls. The transition of the focusing locations from the double-line to single-line were demonstrated by increasing the fluid elasticity and the working space for the multiple-line focusing was introduced by using Reynolds number (*Re*) and Weissenberg number (*Wi*). It is anticipated that this fundamental studies will help design microfluidic devices for the enrichment and effective separation of the micro- and nano-particles developing a new concept of flow cytometry.

Integration of microfluidics with electronics makes it possible to develop a new platform with functions of logic operation, fluidic transistors/diodes, circuit, and memory devices. As applications of the multiple-line particle focusing, we suggested two novel microfluidic logic devices based on the viscoelastic particle focusing. First, element particle logic operations in a microchannel were demonstrated and a binary number “0” or “1” was assigned at the input/output channels depending on the existence of particles. By designing a microfluidic channel with 3 inlets, 1 expansion chamber and 4 outlets, 5 element logic operations including two-input logics and one-input logics were simultaneously realized. For two-input logics, 2 inlets were respectively assigned as input A and input B and another inlet was assigned as a supporting input where the particles are always injected in the channel. The conditions of the inputs were sequentially given as

AB[00], AB[10], AB[01] and AB[11]. By the injection of the particles according to the input conditions, the forms of the particle focusing were varied from single-line to triple-line. Finally, the particle logic operations which are XOR, OR and AND gate were evaluated at the outlets. In order to get the one-input logics such as NOT and Buffer gate, input B was altered as another supporting input. The particle streamlines from each inlet were numerically calculated by using Oldroyd-B model. Second, we developed smart particle valve system by alternating the microchannel material to shape memory polymer (SMP). In case of a polydimethylsiloxane (PDMS) microchannel, the valve system to control the flow and the particles has been operated by adopting the complex layered structures or connecting the external devices. If the recoverable functions of SMPs are integrated into a microfluidic system, the flow in the channel can be controlled in a programmed manner. This can bring about a great impact on microfluidic fields. In this study, a unique microfluidic valve was proposed for switchable particle control by employing the SMP and simple control of the particle path was introduced. The local deformation of the SMP microchannel changed pressure distribution in the microfluidic device, and thus leading to altering the particle streamlines. The microchannel has 2 inlets and 2 outlets, and one branch of the outlets were deformed by Joule-heating. When one outlet channel was deformed, the particles in the channel traveled through the other outlet. The particle path differed by the channel deformation could represent a logic circuit (*i.e.*, $A + S \cdot B$) depending on the presence and absence of particles in the channel. The pressure and velocity fields of the viscoelastic fluids were calculated numerically and structural analysis and heat transfer by Joule-heating were also predicted theoretically. It is expected that this programmable microfluidic system can offer a promising possibility for the development of microfluidic based logic devices.

Despite the negligible interaction between the rigid particles, the control of the focusing position and the traveling path of the particles were demonstrated. This new particle focusing mechanism and particle logic devices based on the microfluidic platform introduced in this work can guide a simple manipulation and analysis of the cell and the flow for the applications in biomedical and pharmaceutical fields.

Korean Abstract

초 록

본 연구에서는 기존에 보고되었던 점탄성 유동에서의 관성력과 탄성력의 균형을 이용한 단일 입자 집중현상을 기반으로 직선 채널에서의 다중 입자 집중 현상을 구현하고자 하였다. 다중 입자 집중 현상을 구현하기 위해 두 가지의 전략을 선택하여 입자 거동을 관찰하고 분석하였다. 먼저, 기존 연구들과 같이 양수의 제 1차 수직응력차를 가지는 세미-플렉서블 고분자 용액을 이용하여 다중 집중 현상을 유도하였다. 채널의 구조에 변화를 주어 입자에 작용하는 관성력과 탄성력의 영향을 제어하였고, 다중 입자 집중을 위한 새로운 메커니즘을 제시하였다. 두번째로, 음수의 제 1차 수직응력차를 가지는 액정 고분자 용액 내에서의 입자 거동을 관찰하였다. 기존 이론으로는 설명이 불가함을 증명하고 흐름 내 생성되는 수직 응력 성분이 입자가 정렬하는 데에 직접적인 영향을 미칠 가능성에 대한 또다른 입자 집중 메커니즘을 제시하였다. 본 연구에서 새롭게 소개한 다중 입자 집중 현상의 응용으로 미세 유체 논리 장치와 입자 밸브 시스템을 개발하였고, 그에 따른 미세 유체 논리 동작을 증명하였다.

제 2 장에서는 미세 유체 장치에서 단일 입자 집중과 다중 입자 집중의 전이를 다루었다. 양수의 제 1차 수직응력차 용액인 폴리에틸렌옥사이드 (PEO) 용액을 사용하여 기존 점탄성 유동 하에서의 입자 집중 메커니즘을 기반으로 유체의 유량과 농도를 조절하여 입자가 받는 관성력과 탄성력을 제어하였다. 본 연구를 통해 채널의 입구 개수와 종횡비와 같은 구조적 영향이 미세 유체 채널에서의 다중 입자 집중 현상을 가능하게 하고, 그 이유는 구조적인 특징에 의해 발생하는 추가적인 관성력 때문임을 확인하였다. 높은 종횡비를 가지는 미세유체 채널은 채널 단면으로 형성되는 제 1차 수직응력차 최소값의 분포가 넓게 형성됨을 수치해석을 통해 확인할 수 있었다. 그러므로 입자가 안정적으로 존재할 수 있는 영역이 증가하여 입자

집중보다는 다중 입자 집중이나 넓게 집중되는 입자 집중 밴드를 형성하게 된다. 여러 개의 채널 입구와 높은 종횡비로 인해 관성력과 탄성력이 비슷한 크기로 입자에 작용하게 되고, 그 결과 입자들은 채널의 가운데 부분이 아닌 채널의 벽 쪽으로 이동하여 정렬하게 된다.

제 3 장에서는 2장에서 소개한 다중 입자 집중 현상을 이용해 점탄성 유동을 기반으로 한 미세 유체 논리 장치를 개발하였다. 전자공학에서 사용하는 이진수를 입자의 존재 유무로 정의하였고, 채널의 입구와 출구 수와 같은 구조를 제어하여 전자공학에서 정의되는 기본 논리 게이트인 XOR, OR, AND, Buffer, NOT 게이트를 고정된 유량, 입자 크기, 유동 조건 ($El \sim 1.483$)에 대해 구현하였다. 또한, 점탄성 유동의 기본적인 물리학을 이해하기 위하여 수치해석을 수행하였고, 입자가 주입되는 경로에 따른 유선 및 점탄성 유동에 의해 생성되는 제 1차 수직응력차의 분포를 예측하였다. 6.19 정도로 높은 분리 효율을 가지는 선명한 다중 입자 집중 선이 관찰되었고, 입자가 출구로 추출되는 것은 이미지 프로세싱을 통해 분석하였다.

제 4 장에서는 소프트 리소그래피를 이용해 미세유체채널을 제작할 때 사용되는 재료인 폴리다이메틸실록산 (PDMS)을 투명한 형상기억 고분자 (SMP)로 대체하여 스마트한 입자 제어를 위한 독특한 입자 밸브 시스템을 개발하였다. 채널의 모양을 프로그램 할 수 있는 기능을 사용하기 위하여 체온 근처에서 형상 변형 및 회복 성능을 보이는 아크릴계 형상기억고분자를 미세 채널로 디자인하였다. 형상기억고분자 미세 채널 내 수력 저항의 크기는 채널의 변형과 회복을 통해 선택적으로 조절할 수 있다. 두 개의 출구에 따라 형성되는 압력장의 변화를 유도해 점탄성 유동 하에 정렬되어 흐르는 입자의 경로를 제어하였다. 형상기억고분자 채널의 변형과 회복을 채널 단면 모양에 대해 구조해석으로 예측하였고, 변형에 의한 압력장 변화를 이론적으로 계산하였다. 이러한 입자 밸브 시스템은 입자의 유무 (A와 B)와 채널의 변형 유무 (S)를 기준으로 논리 회로인 A+S·B로 표현될 수 있다.

제 5 장에서는 음수의 제 1차 수직응력차를 가지는 하이드록시프로필 셀룰로오스 (HPC) 용액을 이용하여 입자 집중현상을 관찰 및 분석하였다.

기존에 보고된 양수의 제 1차 수직응력차 용액 유동에서 관찰할 수 있는 한 줄 정렬 현상과 달리 같은 구조의 채널에서 입자가 두 줄로 정렬되는 현상을 관찰하였다. 이러한 독특한 입자 집중 현상은 입자 크기가 커짐에 따라 확연한 차이를 보였고, 입자 크기 별 입자 집중 위치 간의 거리 차이가 발생해 일자 채널에서도 높은 분리 효율을 보였다. 채널 너비 방향으로 작용하는 수직 응력 성분 τ_{yy} 를 실험적으로 계산하고, 새로운 무차원수 도입을 통해 τ_{yy}가 점탄성 유동 내 입자 집중에 미치는 영향을 분석하였다.

주요어 : 다중 입자 집중, 미세 유체 논리 장치, 점탄성 유동, 형상 기억 고분자, 제 1차 수직응력차 (N_1), 수직 응력 성분, 입자 분리, 유동 해석, 구조 해석, 열 전달

학번 : 2013-23041